NOVEL STUDIES ON THE FORMATION AND CHEMICAL REACTIVITY OF COMPOUND CLUSTERS AND THEIR PRECURSORS IN THE GAS AND LIQUID PHASE

A Dissertation
Presented to
The Academic Faculty

by

James Adam Ferguson Bradshaw

In Partial Fulfillment
of the Requirements for the Degree
Doctor of Philosophy of Chemistry

Georgia Institute of Technology

December 2008

NOVEL STUDIES ON THE FORMATION AND CHEMICAL REACTIVITY OF CLUSTERS AND THEIR PRECURSORS IN THE GAS AND LIQUID PHASE

Approved by:

Dr. Robert L. Whetten, Advisor
School of Chemistry and Biochemistry
Georgia Institute of Technology

Dr. Thomas Orlando, Chair
School of Chemistry and Biochemistry
Georgia Institute of Technology

Dr. Mostafa El-Sayed
School of Chemistry and Biochemistry
Georgia Institute of Technology

Dr. Walter de-Heer
School of Physics
Georgia Institute of Technology

Dr. Facundo Fernandez
School of Chemistry and Biochemistry
Georgia Institute of Technology

Dr. Lawrence Bottomley
School of Chemistry and Biochemistry
Georgia Institute of Technology

Dr. Sidney L. Gordon
School of Chemistry and Biochemistry
Georgia Institute of Technology

Dr. Andrew Leavitt
Department of Chemistry
University of West Georgia

Date Approved: August 6th, 2008

Dedicated to my Grandfather, James Harvey Ferguson,
from whom I learned a little bit about science and a lot about life.

ACKNOWLEDGEMENTS

First and foremost, I am indebted to my family for their love and support over the many years of my education. To my mother and father, brother and sister, grandmother, aunts and uncles, cousins, thank you. To the countless other people, to my friends and surrogate families, I am who I am and have accomplished what I've accomplished because of you.

Undoubtedly omitting many people very deserving here, with my sincere apologies, I would like to extend my gratitude to the following people for their interminable assistance, guidance, and friendship over the years in no particular order: Kindra Freiherr, Anthony Godwin, Prof. Robert Whetten, Prof. Larry Bottomley, Prof. Facundo Fernandez, Prof. Tom Orlando, Prof. Mostafa El-Sayed, Dr. Gary Dobbs, Dr. Federico Polo, Prof. Andrew Leavitt, Prof. Sidney Gordon, Prof. Farooq Khan, Dr. Melissa Arredondo, Dr. Ryan Price, Dr. Richard Wyrwas, Kane Barker, Karen and James Goeders, Josh Bietz, Angello Bello, Karl Xjimenez, Tal Berkowitz, Arianna Biesso, John Bowlan, Jef Bredemeir, Angie Brogden, Colton Brown, Dr. Marcelle Buford, Sarah Call, Sarah Cater, Sam Mize, Scott Centers, Craig Clark, Jay Clark, Brent Crenshaw, Greg Dunn, Mike Escoe, Karine Etienne, Elizabeth Farris, Prof. Jean-Francois Masson, Will Frasier, James Glasscock, Dr. Greg Grieves, Christina Hampton, Dr. Chris Hughes, Hanif Hunter, Ian Jones, Joel Rausch, Thaddeus Keefe, Gary Kusic, Chris Zetena, Brett Mauro, Reagan McRae, Amanda Minino, Kelley Mitchell, Kevin Price, Sharon Mize, Heidi Parker, Chris Montgomery, Dr. Devang Naik, Brian Rickert, James Sullivan, Danny White, Prof. Louis Brus, Prof. Paul Wine, Prof. Boris Mizaikoff, Dr. Leigh Bottomley,

Dr. Bill Baron, Dr. Mary Peek, Dr. Robert Braga, Dr. Christine Kranz, Prof. Michael Chapman, Prof. Edward Conrad, Prof. Dragomir Davidovic, Prof. David Finkelstein, Prof. Phillip First, Prof. Eugene Patronis, Prof. Michael Shatz, Prof. Turgay Uzer, Prof. Andrew Zangwill, Dr. Cameron Tyson, Karen and David Jones, Ryan English, Joelle Hall, Heather Luttrell, Scott Mullin….

TABLE OF CONTENTS

LIST OF TABLES

LIST OF FIGURES

LIST OF SYMBOLS AND ABBREVIATIONS

6061 T-6	Aircraft grade aluminum
AC	Alternating current
Alumina	Al_2O_3 (not single crystal)
BBO	BaB_2O_4
CF	ConFlat vacuum gasket
Chevron	Image aligned microchannel plate configuration
DC	Direct current
d_d	Drift Region Length
DFT	Density Functional Theory
d_v	Gas Valve Orifice Diameter
E_0	First Stage Electric Field
E_1	Second Stage Electric Field
ESI	Electrospray ionization
FTIR	Fourier-transform infrared
GPIB	General purpose interface bus (IEEE 488)
GS/s	Giga-samples per second
HV	High voltage
ID	Inside diameter
KDP	KH_2PO_4
LDI	Laser desorption ionization
MALDI	Matrix assisted laser desorption ionization
MCP	Microchannel plate
MESH	Number of wires per linear inch

MP2	Møller-Plesset perturbation theory
MS	Mass spectrometry
Nanoscience	Nonsense
Nd:YAG	Neodymium-doped yttrium aluminum garnet ($Nd:Y_3Al_5O_{12}$)
NIR	Near infrared electromagnetic spectrum
OD	Outside diameter
OFHC	Oxygen-free high-conductivity
P_C	Carrier Gas Pressure
P_R	Reactor Pressure
R2PI	Resonant two-photon ionization
RF	Radio frequency
RPM	Revolutions per minute
RS-232	Recommended standard 232
S_0	First Stage Spacing
S_1	Second Stage Spacing
SAM	Surface Assembled Monolayer
T-304	Graded stainless tool steel
T-316	Graded stainless tool steel
t_g	Gas Valve Pulsewidth
TIG	Tungsten inert gas
TOF	Time-of-flight
TPI	Threads per inch
TTL	Transistor-transistor logic
UHV	Ultra-high vacuum
USB	Universal serial bus

UV	Ultra-violet electromagnetic spectrum
v	Carrier Gas Sonic Speed
Variac	Variable alternating current power supply
V_{gas}	Volume of Gas Released from Gas Valve
VIS	Visible electromagnetic spectrum
V_R	Reactor Volume

LIST OF EQUATIONS

SUMMARY

Presented are four separate and unique studies on molecular and nanoscale systems: Atmospheric hydration and aggregation of NaCl clusters, highly water-soluble aurous-thiolate oligomers, water-soluble gold clusters from aurous-thiolate oligomer precursors, and gold iodide clusters.

Adsorption of water on cationic and anionic sodium chloride clusters is investigated to elucidate active sites of molecular interaction as well as primary aggregate formation kinetics. Considered an exceptionally abundant atmospheric species, experiments are conducted to further quantify gas phase chemistry and hydration/solvation of alkali halides.

Currently the most soluble of all known gold-thiolates, para-mercaptobenzoic acid-based (pMBA) aurous-thiolate oligomers are investigated and physical and chemical properties quantified. Solubility, structural conformation, and poly-dispersity of higher homologs are observed with the goal of further applications in clusters research, medical and biomedical, and industry.

Gold thiolate clusters, synthesized using pMBA-based oligomers, are investigated through reductive formation in solution. UV-VIS and UV-VIS-NIR spectroscopy is undertaken to assign structures based on predictions of the HOMO-LUMO gap and other electronic transitions.

Gold iodide is investigated in relation to the common thiolate-halide analogy. Synthesis and characterization of a solid precursor as well as anion and cation cluster formation is presented as part of an ongoing collaboration.

CHAPTER 1

INTRODUCTION

In nanoscience, chemical species of specific interest are typically defined as objects that are quantifiable on the scale of a nanometer. Entities with properties inherent to their scale more-often-than-not fall in the sub-50nm regime. They are often further classified according to configuration where intrinsic properties emerge from dimensional restrictions, often allowing them to act as one, two, or three-dimensional objects. More significantly, the nanoscale cluster and molecular genus may exhibit intensive discrete properties that differ significantly from those observed in their larger breathren or their bulk conformation.

Although the public eye and popular media considers nanoscience, often erroneously referred to as nanotechnology, paradigmatic of modern 20th century science, its actual heritage is much more extensive. The English chemist Michael Faraday is credited with the first scientific chronicle of nanometer-scale materials. In 1857 he provided the first objective description of nanoscale species, emphasizing the significant optical characteristics of nanoscale gold and other metals.[1] Prior to Faraday, nanoparticles, unbeknownst to the artists, were used in 9th century Mesopotamia[2] for various aesthetic inclusions to pottery. Gold nanoparticles were also common, though not fully understood, in providing the traditional deep-red tint associated with stained glass windows found the world over.

Nanoscience has and will continue to be an area of intense interest. A prodigious variety of potential applications exist in materials science, biomedical and medical

engineering, electronics, etc. Within the realm of pure chemical science, nanoscience endeavors to uncover and quantify the phenomenon involved in fundamental chemical reactions, perhaps someday consistently one molecule at a time. This fundamental viewpoint provides an encompassing description of all chemistry that occurs in the laboratory and by correlation to that of nature.

Nanoscience provides an effective bridge between bulk materials and their atomic or molecular structures. Generally bulk materials display constant physical properties regardless of their size, given certain environmental conditions such as pressure and temperature. Nanoscale species defy these generalities, exhibiting size-dependent properties such as superparamagnetism,[3] quantum confinement,[4] and surface plasmon[5] resonances. In the recent literature, single layer graphite, known as graphene, may lead to the next generation of micro and nanoelectronics.[6,7] Graphene has the ability to act as a conductor or semiconductor depending on its' effective width as a wire. This feature, specific to the nanoscale, could allow for a single material to be used throughout simple and complex electronic circuits.

Tending towards the nanoscale, the dominant laws dictating behavior and characteristics transition from classical ensemble-based theory to that of quantum mechanics. A common effect in all species, as their size shifts to the nanoscale, is the drastic increase in the percentage of atoms at the surface relative to the core. For bulk materials larger than a few hundred nanometers, the percentage of surface atoms is effectively negligible relative to the total number of atoms in the core. Due to the obvious geometrical relationships of a sphere, as the size decreases, $r \rightarrow 0$, the relationship of area to volume is obvious:

$$\frac{Area}{Volume} = \frac{3}{r} \qquad \textbf{(1.1)}$$

In the lower physical limit, it becomes clear that the surface area becomes dominant over volume. This geometrical trend, commanding the region of small scale, causes many materials to exhibit a number of special properties, relative to the bulk, without being so small as to be solely defined by quantum mechanics. The bending of bulk copper, for example, has been shown to occur with the movement and transition of inclusive copper clusters of ~50 nm.[8] Smaller copper particles, incapable of this deformation process, have been shown to be exceptionally rigid, known as super-hard, materials.

Tending further downward in size, towards that of single molecular species, brings about the complete overruling of most classical descriptions, relying almost entirely on the laws of quantum mechanics. In this region, where the very structure of clusters and other species may rely on size, number, and type of available atoms, an enormous amount of variability in chemical and physical properties exists. Discussed in Chapter 3, the addition of one or two atoms to a small NaCl cluster can induce a drastic change in structure, transforming overall chemical reactivity, charge density, and dipole moment. Lesser environmental perturbations, such as the presence of an externally applied field in the form of a weak ionic interaction, are also observed to induce structural deformations. These small and large changes in structure can cause a previously reactive cluster to become effectively inert.

Typical to the discussion of nanoscience, the common descriptive bearing is to start at the bulk and move downwards in scale. A very active region of investigation that is responsible for much of the developments made in recent years focuses on transitioning in scale from the other direction; starting small and working up in size. Many clusters below the 50nm scale are synthesized from atomic or molecular precursors much smaller, often even sub-nanometric. Gold particles, for example, are routinely produced from smaller molecular constituents containing single gold atoms, and chemically or thermally induced to coalesce into larger, nanoscale species. These nanometer species can also, by chemical or thermal means, be induced to coalesce further and further until the bulk material is realized. Unfortunately, the precursors and products involved in this constructive synthesis are often incompatible with chemicals and environments of reasonable analogy to the intended applications. Biological applications, for example, necessitate species that are stable in aqueous environments inside a relatively narrow pH range. In Chapter 4, we present data and analysis on a molecular precursor to gold nanoparticles, in the form of a narrowly poly-disperse oligomeric chain, that lends itself especially well to synthesis, analysis, and application in any number of different fields. Its' observed higher solubility under neutral pH conditions provides a rare ease of integration previously unavailable for gold species.

CHAPTER 2

CUSTOM CRYOGENIC TOF-MS DEVELOPMENT

2.1 Introduction

Fundamental to the further understanding of physical and chemical processes is the necessary analysis of the aforementioned transition region from the atomic to the bulk: territory of nanoscience. Study of this significant size domain offers insight into nearly all palpable and theoretical systems. It has become, more often in recent years, a primary source for the advancement and correction of existing fundamental orthodox theories. In the laboratory, chemical systems are now capable of emulating the theoretical properties of cosmological events,[9] effectively changing their chemical identity on the periodic table[10] (albeit without alchemy), and most importantly, lending insight into the causality and consequence of much that occurs in the physical world.

An unfortunate intractability common to the study of these nano and/or molecular species is often the lack of an exacting analytical characterization. Despite the developmental leaps and bounds of fields such as microscopy, be it imaging or scanning, is the associated difficulty in analysis of the recurrently poly-disperse collection of species, each having unique and novel properties. Elucidating quantitative information can, and has to a large extent, be done with mass spectrometry. This type of characterization allows for an exact mass assignment that, along with tandem analytical techniques such as spectroscopy, can be used to determine primary structures. Mass spectrometry is also of particular interest in studying species that cannot be synthesized

in a wet lab and/or are only known to be stable in minimally interacting environments such as high vacuum.

2.2 Motivation

For gas-phase species, such as those found in the stratosphere and troposphere driving much of atmospheric chemistry, one finds laser-desorption ionization (LDI) as one of the more useful techniques. Although other ionization techniques and sampling systems have certain advantages, LDI allows for almost perfectly analogous atmospheric conditions to be recreated in the laboratory. Equivalent temperatures, pressures, and the high ultra-violet (UV) radiation fluence found at higher terrestrial elevations are readily accessible. Ablation of a sample using various wavelength pulsed nanosecond laser sources and a quenching or thermalizing carrier gas allows for bulk reactant samples to be used to produce kindred molecular species, often having exceptional properties not shared by the bulk.

Time-of-flight mass spectrometry (TOF-MS) has been determined as the most appropriate detection system due to both its' exceptionally high sensitivity (gain values > $1.4 \text{ X } 10^6$) as well as its pulsed operation to maximize duty cycle when coupled to a pulsed ion source. Every experiment carried out by the mass spectrometer is described here chronologically from the creation of molecular species, to various probing and tandem techniques, and then to mass analysis.

2.3 Source

To accomplish the assorted goals and results presented throughout this work, a pulsed LDI flow reactor was judged the most appropriate source for cluster creation,

formation, coalescence, and analysis. The following reactor design was, in large part, adopted from a highly successful molecular beam system designed and employed by Prof. Walter de Heer; here implemented with assorted variations.

2.3.1 Flow Reactor

High-speed gas valves are readily commercially available but with few suppliers and variations on available design. Much of the instrumentation development pursued here revolves around available componentry. Additionally, one of the more expensive considerations in mass spectrometry is available evacuation pumping, necessary to maintain a high enough level of vacuum for effective operation. It follows that, within the useful detectability limit, as small a source and required pumping load as possible is preferred to keep required mechanical rotary-vane and turbo-molecular pumping to a minimum.

General Valve Company Inc. ultra-fast valves, Series #9, were employed. With a minimum useful pulse-length of 200μs and a maximum operating pressure of 34bar, the internal volume of the reactor had to be designed so as to allow for as broad a range of conditions as possible. A major consideration was that the atmospherically analogous region, 0.1 – 1atm, was of primary interest and had to be readily accessible without extremes in operating parameters.

2.3.2 Reactor Volume

Using a typical pulse length of 300μs and a He carrier gas pressure of 7bar, an ideal internal reactor volume (for ~0.5bar) was determined simplistically, and relatively

accurately, assuming a linear release of gas from the pulsed valve at the sonic barrier into vacuum:

$$V_{gas} = t_g \pi (\frac{d_v}{2})^2 \nu \qquad \textbf{(2.1)}$$

Here V_{gas} is the total volume of gas released into the reactor chamber at the carrier gas backing pressure P_c, d_v is the diameter of the output orifice of the ultra-fast valve, v is the supersonic expansion velocity of the carrier gas, and t_g is the pulse length of the ultra-fast valve. Assuming an ideal gas it follows that:

$$P_c V_{gas} = P_R V_R \qquad \textbf{(2.2)}$$

Where P_R is the reactor pressure and V_R is the reactor volume. With a desired operating pressure of $P_R = 0.5$bar:

$$V_R^{0.5bar} = 2(P_C) t \pi \left(\frac{d_v}{2} \right)^2 \nu \qquad \textbf{(2.3)}$$

With $P_C = 7$bar, t = 300μs, d = 0.075cm, and v = 130,000 cm/s

$$V_R^{0.5bar} = 2(7)(300\mu s)\pi \left(\frac{0.075}{2} \right)^2 (130{,}000) \cong 2.4 cm^3 \qquad \textbf{(2.4)}$$

As has been found in this group's previous work using flow reactors, a variability of output nozzle lengths, diameters, and orifice sizes, was known to be necessary. As such, the internal volume of the reactor, excluding the reactor nozzle, was made to be ~2 cm^3 allowing for a large margin of freedom in variability.

2.3.3 Construction and Assembly

The Main reactor was constructed from 99.99% purity oxygen-free high-conductivity (OFHC) copper:

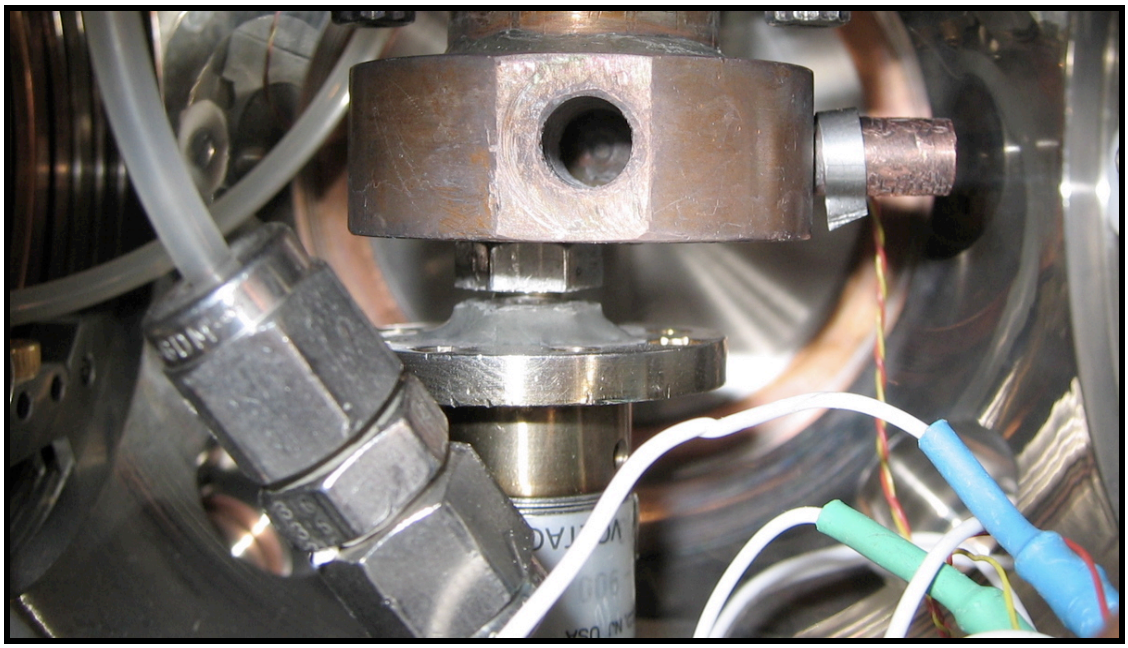

Figure 2.1. Reactor Assembly.

Copper was chosen for its low thermal expansion coefficient, here necessary for an operation range > Δ400K. Also beneficial was copper's high thermal conductivity and relative ease of fabrication. The reactor was fabricated from stock billet, acquired from

McMaster-Carr Supply Company, by lathe, alternating and direct current tungsten inert gas (AC/DC-TIG) welding, end-mill machining, and silver-solder brazing. The main reactor and assorted nozzles were machined and match tap-died with a ¼"-28 threading to allow for simple and quick changing of various output nozzles. Different nozzle parameters, along with pressure and timing adjustments, allowed for control of resident time of clusters inside the reactor, lending to a reasonable control on cluster size as well as reaction times with other mixed reactants. An additional benefit of a modular reaction nozzle not undertaken here is the potential of using catalytically active materials, thus making an enormous variety of experiments available to the user.

2.3.4 Reactor Nozzle

By trial and error, various reactor nozzles were designed, fabricated and tested to maximize cluster size dispersion as well as cluster yield. For most studies conducted, the reactor nozzle shown to the right in Figure 2.1 was used. With an inside diameter of 0.5cm, an internal length of 2cm, and an output orifice of 0.8mm, this nozzle endows the reactor source with a total internal volume of ~2.4cm^3 – consistent with the basic calculations from Section 2.3.2. As demanded by a pulsed source for directional flow, the reactor nozzle orifice had an effective length of zero with a tapering angle of 120^0, coming from the standard drill-bit cutting face angle.

2.3.5 Alignment

To ensure a high degree of adjustability, a 0.25" tongue and groove rotational/horizontal positioning stage was machined out of OFHC copper and placed immediately above the heater:

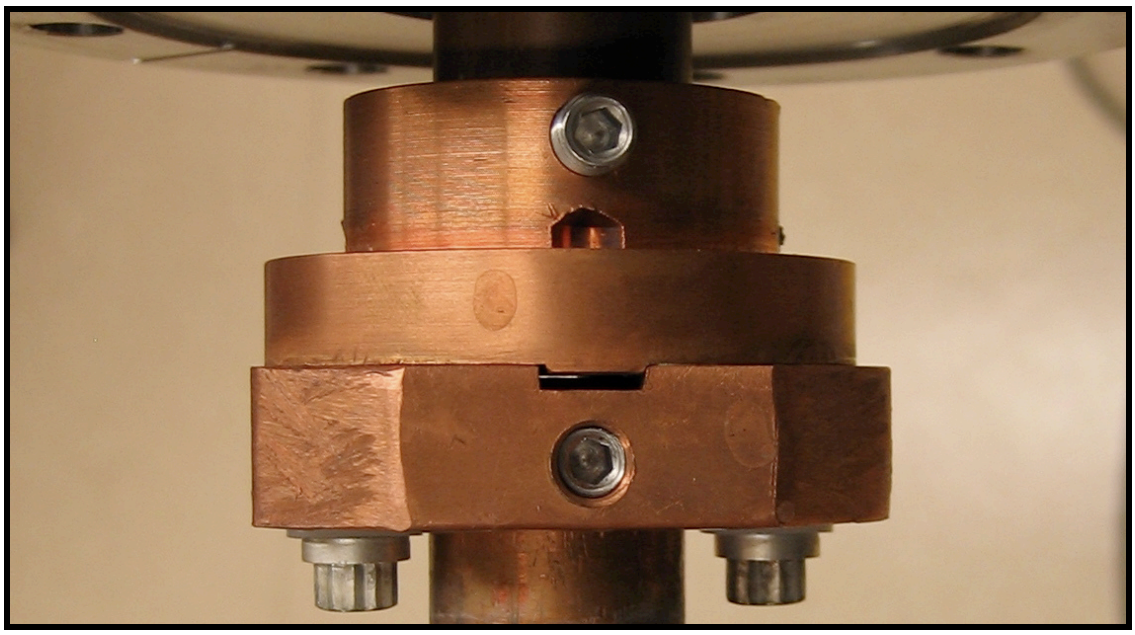

Figure 2.2. Rotational and Horizontal Alignment Stage.

This established proper alignment of the reactor output nozzle with the conical skimmer discussed in Section 2.6. Delrin® (DuPont) gaskets and silver-coated stainless steel setscrews were used to secure positioning.

2.3.6 Thermal Control

The existing system[11] that motivated this undertaking utilized a two-valve system. Below 50K an intermediate storage reservoir was found to be necessary to thermalize the helium carrier gas prior to introduction into the reactor. A standard ultra-fast valve assembly would feed this reservoir.

Because the solenoid assembly of the ultra-fast valve does not operate effectively below 50K and it was appropriate to implement a second valve, remotely mounted, that allowed only the gasket-poppet system to be exposed to the cryogenically cooled reactor. For the research undertaken here, the remote reservoir and remotely operated solenoid assembly were bypassed and a single valve was found sufficient.

Above 50K no thermal isolation was deemed essential. The main reactor housing was coupled to a vertically suspended closed-cycle He cryogenic cooling assembly (APD model DE-204) via a 7/8" diameter 4" long solid cylindrical piece of OFHC copper with connections made using DC TIG welding as well as silver solder brazing. For stable thermal control, a pipe heater (Omega Inc. #MBH-1210150B/120) was installed along the 4" copper coupling-rod. Any variation in temperature was made by output to the heater, keeping the cold finger operating at maximum capacity.

Temperature was monitored and controlled by an Omega Inc. feedback loop sensor (model CNiTH-i16D33-2). Thermal output of the heater was regulated by two type K thermocouples. One thermocouple was placed at the coupling rod/reactor interface and the other at the output reactor nozzle. These two temperatures were averaged and assigned as the cluster thermal bath temperature. Above 350K the cold finger assembly must be shut off but can be exposed to temperatures as high as 450K without damage. Higher temperatures, not undertaken here, would require thermal de-coupling to the cryogenic system or an inline insulation stage such as alumina (Al_2O_3).

2.3.7 Enclosure and Ablation Source

The frequency tripled output (355nm) of a Continuum Inc. model 660B-10 Nd:YAG laser was utilized for ablation. A 1mm diameter 1.5cm long hole was drilled

into the back of the reactor, aligned with the output orifice of the reactor nozzle, for introduction of ablative light. A 50cm focal length 25mm diameter quartz doubly-convex lens was mounted along an adjustable optics guide for alignment and focusing into the reactor through a quartz view-port fitted 2 ¾" conflat (CF) plate. An adjustable diameter iris was placed in between the ablation laser and focusing optics to control fluence.

The entire source assembly was installed inside a Kimball Physics Inc. 4.5" CF "Spherical Cube" chamber (MCF450-SC60008):

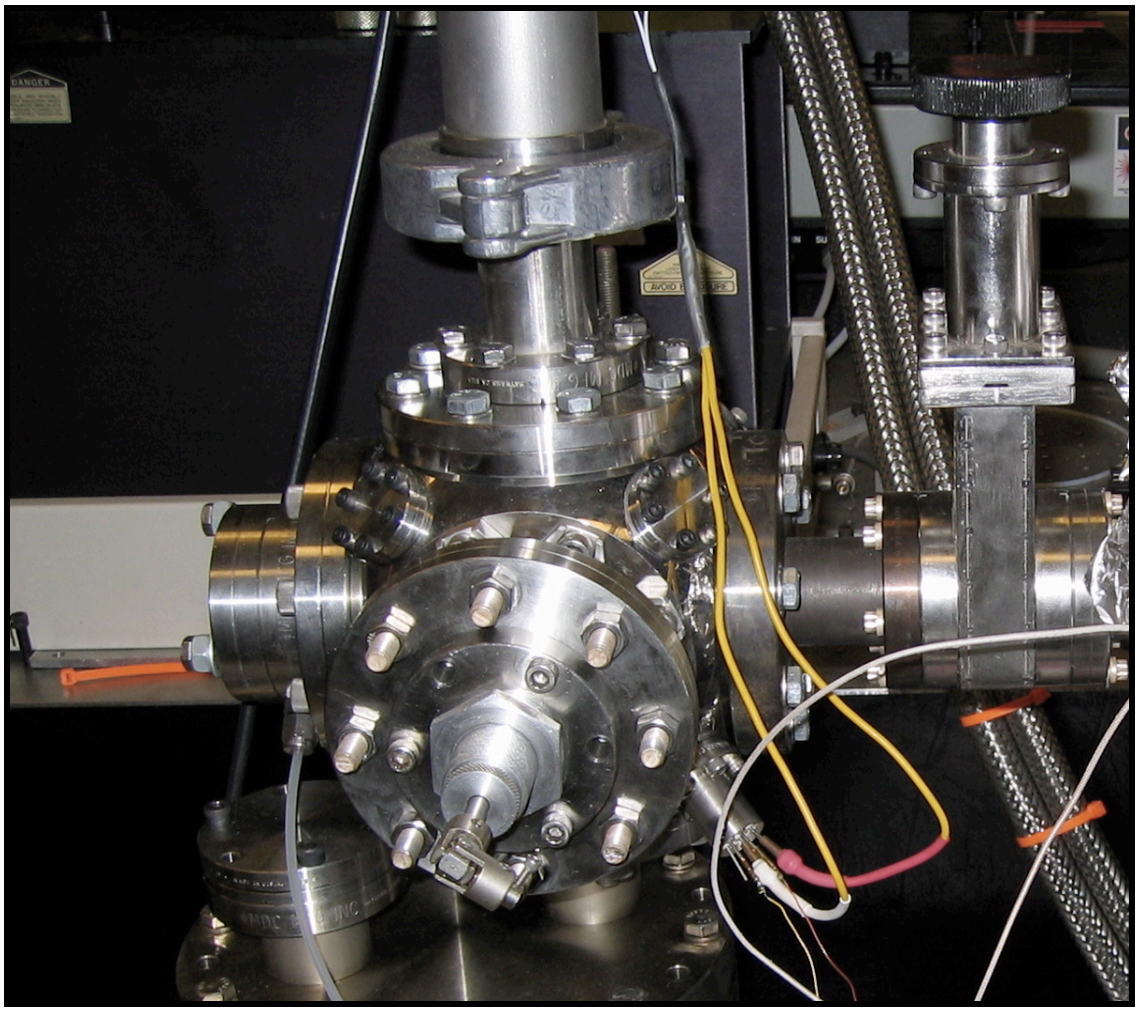

Figure 2.3. Source Chamber.

CF electrical feed-throughs (micro CF-1.33”) were used for electrical connections with the pulsed valve, thermocouples, heating assembly, etc. A Leybold-Heraeus Turbotronik 360 turbo-molecular pump, backed by a Leybold-Heraeus Trivac D8A rotary vane pump, was used for vacuum. The resulting assembly was attached to the remaining instrument, discussed in following sections, by a MDC Inc. GV-1000 gate valve. All CF vacuum hardware was used with OFHC copper or Viton® (DuPont) gaskets.

2.4 Target Rod Fabrication and Carrier

For sample preparation, 1/8” cylindrical target rods were prepared in a custom hydraulic die using high purity granular or crystalline starting reagent. 1.5-2 grams of material was placed inside a hardened high carbon-steel die and pressed, typically with a tungsten or tool-grade steel rod, at approximately 7500bar:

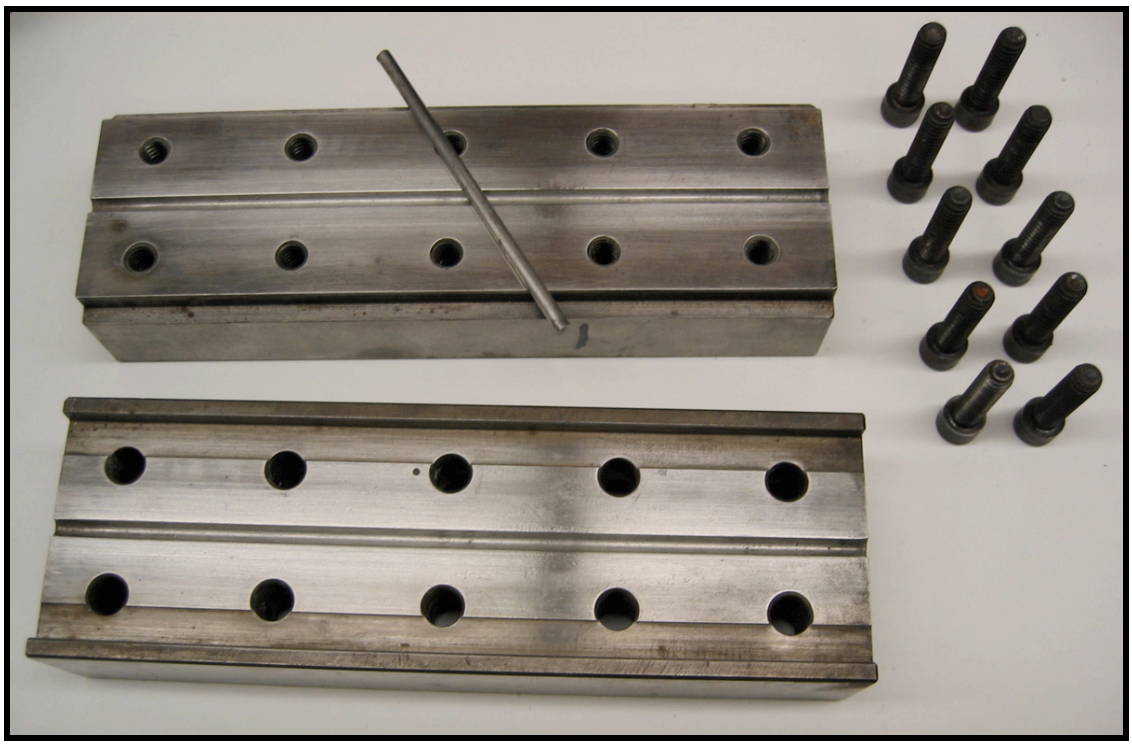

Figure 2.4. Target Rod Die.

It was discovered that the presence of a small quantity of liquid, matched so as not to dissolve the starting material or induce a reaction, considerably improved the quality and robustness of the target rod by reducing stiction between the target material and die and more evenly distributing pressure throughout the sample

Previous experience with small 1/8” diameter target rods warranted the development of a carrier sleeve for the target material (seen to right in Figure 2.5):

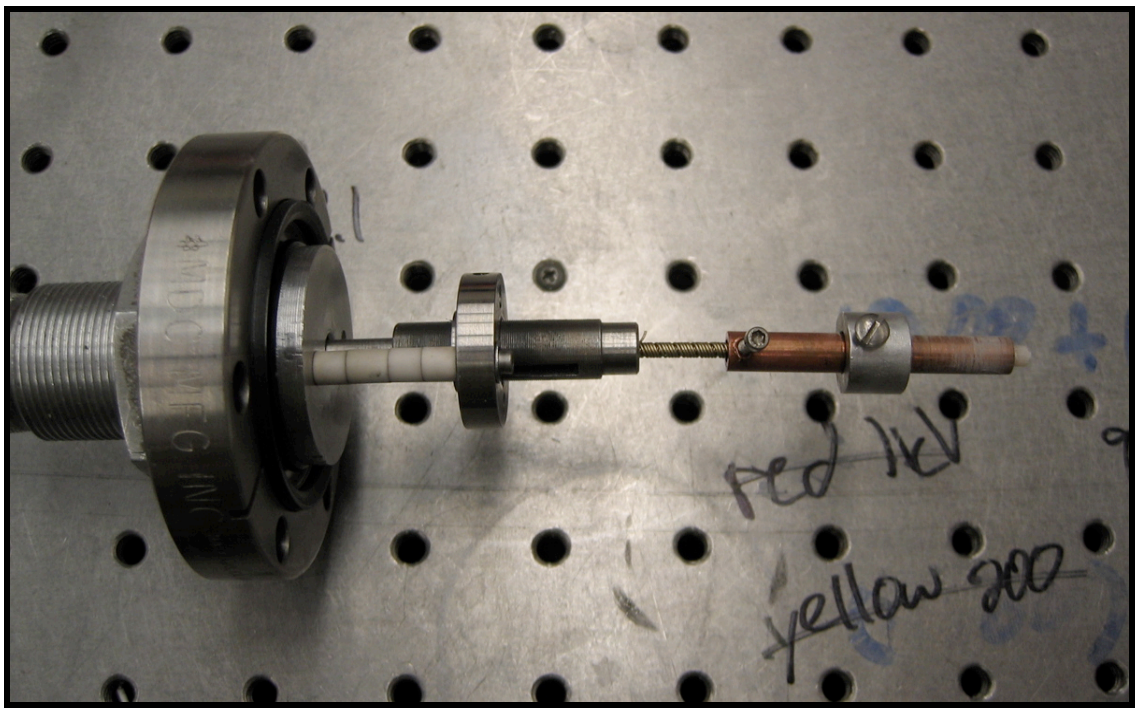

Figure 2.5. Target Carrier Sleeve.

Two major issues with previous target rod handling were the often large variation in diameters, introducing a possible major leak into the source reactor, as well as the common breaking or cracking of the target rod due to small applied torques and the inherent fragility of the starting material. A ¼" OFHC copper sleeve, fitted with high tolerance (<150μm gap) to the sample input on the reactor, was lathe-turned from stock ½" billet rod and coupled to a 100 thread-per-inch (TPI) feed screw. As seen in Figure 2.5, a stop collar was also installed to ensure that the target rod would not get damaged form over extension. Additionally, since the typically feed distance was typically equal to or less than 2mm, the total internal volume of the reactor never varied by more than 2.5%. The target position and feed rate were controlled by an externally mounted one-

rotation per minute (rpm) AC motor via an ultra-high vacuum (UHV) compliant rotary motion feed-through.

2.5 Reactant mixing

Introduction of various reactants from high vapour pressure liquids was accomplished using an inline gas-liquid bubbler:

Figure 2.6. Carrier Gas Bubbler.

Carrier gas, typically helium, was introduced into the bubbler and forced to pass through the reactant liquid before making its' way to the pulsed valve for introduction into the

source reactor assembly. Viton gasketted ¼" Swagelock Inc. compression fittings allowed for rapid exchange of different reactant liquids as well as operating pressures in excess of 10bar. The entire assembly could also be heated using a variable voltage (variac) controlled inductive heating tape to assist in providing a reactant saturated carrier gas. Temperatures were limited to 473K due to the Viton gaskets.

2.6 Skimming and Pressure Differential region

Typical to any TOF-MS system, the drift region that allows separation of differing mass species by velocity distribution requires an operating pressure at or below 10^{-6}torr. Pressures above this threshold tend to blur mass resolution.[12] More fiscally significant is the increased likelihood of damaging the microchannal plate (MCP) detector assembly that has operating voltages as high as 5kV and internal electric fields as high as 30kV/cm. High pressures within the detection system run a significant risk of arcing, causing irreversible damage to both the detector assembly as a whole as well as any sensitive electronics thereof coupled such as pre-amplifiers, rapid data acquisition oscilloscopes, etc.

Due to the excessive pumping available to the source region, it was found unnecessary for additional inline pressure differentials. The pulsed molecular beam produced by the source is allowed 2cm before encountering a 1.2mm conical skimmer assembly:

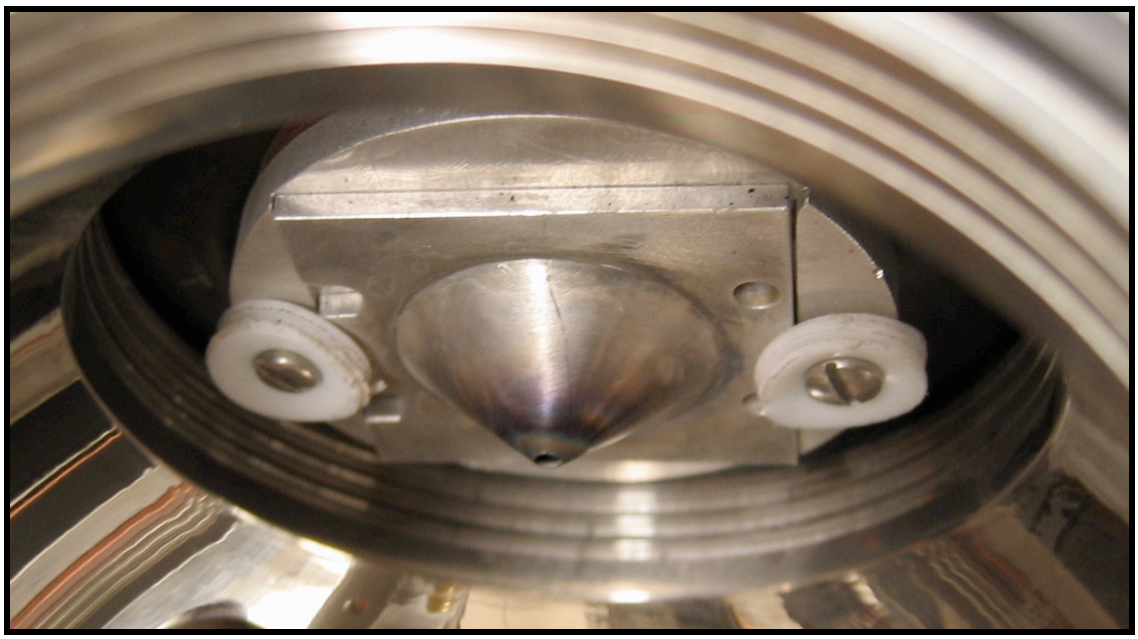

Figure 2.7. Primary Skimmer**.**

The skimmer is made of 6061 T-6 aluminum, permitting easy maintenance and cleaning and is typically grounded to the rest of the instrument. It is mounted to a custom-machined grooved base plate allowing for fine-tuning of vertical position relative to the reactor nozzle output. Using a custom Delrin® shim and electrical feed a floating voltage can be applied for experiments deeming something as such necessary. A relatively well-defined cylindrical molecular beam, culminated by both the reactor nozzle and conical skimmer, enters the high-voltage (HV) extraction region, which is also home to the detection system. A horizontal-slit skimmer in front of the HV extraction region further reduces the pulsed molecular beam down to 150μm in height using two standard straightedge razor blades mounted onto a custom adjustable T-304 stainless steel base. The base was made in part, using high-resolution computer numerically controlled (CNC) machining equipment care of Ian Jones at Jones & Company Inc. Atlanta, GA.

2.7 Ionization Region

2.7.1 Design and Construction

Once the molecular beam has passed through the horizontal skimmer, it is immediately below the pusher plate of a two-stage acceleration region. The region consists of three plates including a pusher plate, an intermediate plate, and a final grounding plate. Spacing for the extraction region is kept compact to maximize the length of the following drift region prior to detection:

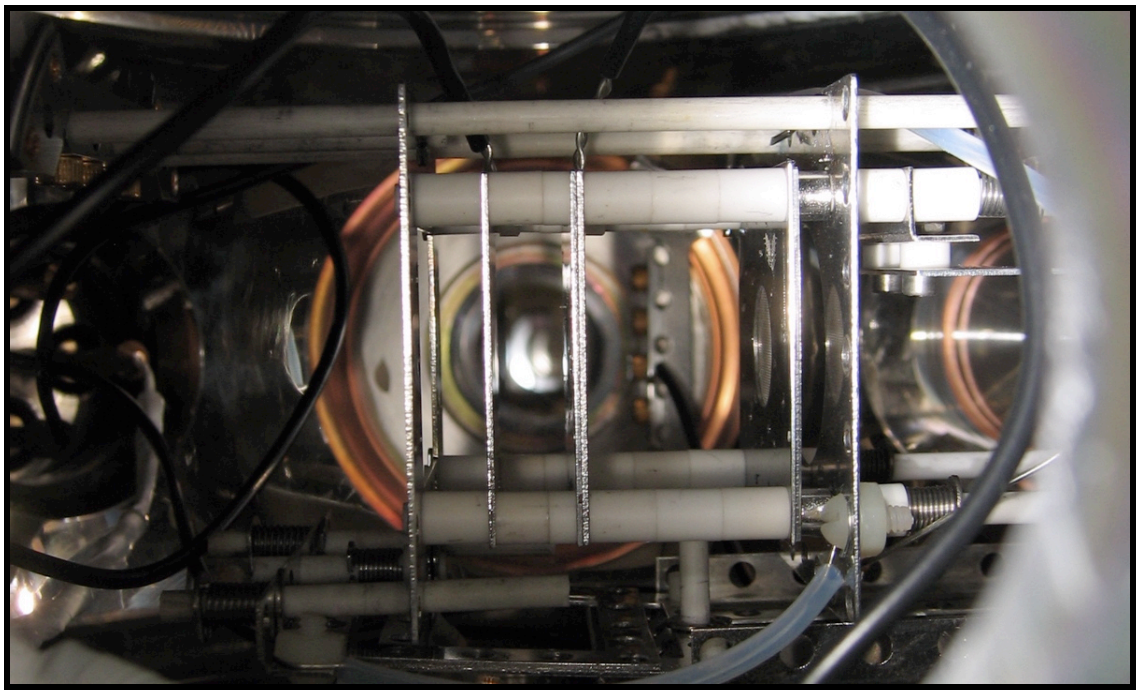

Figure 2.8. HV Extraction Region.

Kimball Physics Inc. components are utilized here due to their ease of configuration and high tolerances. Acceleration plates, 3.5cm squares, are installed along four 1/8” outside diameter (OD) alumina guide rails. Use of ceramic guide rails allows

independent voltages to be applied to each plate and minimizes stray fields encountered by ions being accelerated. The first plate (pusher) is solid T-304 stainless steel while the second and grounding plate have a 2cm and 1cm hole center-cut into them. Both the grounding and middle plate have T-316 500 mesh stainless-steel screens to maximize electric field uniformity in the region. Each screen is expected to reduce signal by 10%, here a 20% total loss,[12] which was experimentally determined to be insignificant. The three acceleration plates are spaced using 1/8" inside diameter (ID) alumina cylinders. The total spacing between the first and second plate is 7.71mm and spacing between the second and third plate is 20.36mm.

Directly below the grounding plate is an additional plate, orthogonal to the accelerating electric field, which allows for a deflection voltage to be applied. The deflection voltage, typically 0-120V, enables the user to select a mass range to be directed towards the detector. Because incoming species are moving at a high rate of speed prior to extraction, this voltage compensates for this initial velocity orthogonal to the acceleration field.

The entire acceleration assembly, horizontal skimmer included, is mounted on a vertical positioning stage, machined from billet 6061-T6 aluminum to compensate for changes in the molecular beam position induced by expansion and contraction of the copper coupling rod in the source region at different temperatures. The remaining molecular beam not extracted for detection is diverted directly into a Varian Inc. TV-551 8" CF turbo-molecular pump roughed by a Varian Inc. DS-302 rotary vane pump.

2.7.2 Theoretical Optimization

The applied voltage to the middle plate is adjusted and optimized for maximum resolution relative to the total applied voltage. Taking into account a drift length d_d, pusher plate middle plate spacing of s_0, and middle plate grounding plate spacing of s_1:

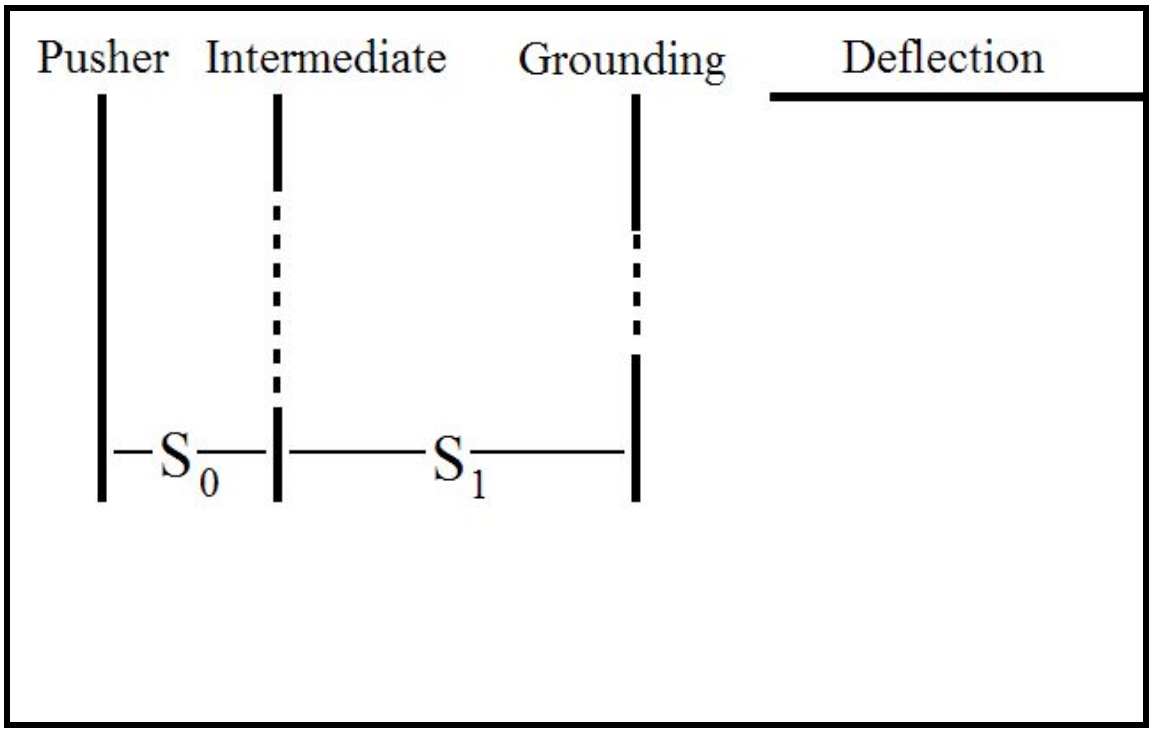

Figure 2.9. Extraction Region Schematic.

One can determine the theoretically optimized[12] values of internal electric fields of E_0 and E_1 and adjust in the input voltages appropriately for maximum resolution by way of time-lag focusing. Assuming that:

$$\sigma = s_0 + \frac{E_1}{E_0} s_1 \qquad \textbf{(2.5)}$$

and that the time-of-arrival to detector difference for ions at s_0 and $s_0 + \Delta s_o$ is:

$$\Delta t = \left(\frac{m}{2eE_0}\right)^{\frac{1}{2}}\left[\frac{1}{\sqrt{s_0}} - \frac{s_1}{\sqrt{s_0}}\left(\sqrt{\sigma} + \sqrt{s_0}\right)^{-2} - \frac{d_d}{2\sqrt[3]{\sigma}}\right]\Delta s_0 \qquad \textbf{(2.6)}$$

we let $\Delta t/\Delta s_0 = 0$, insuring all mass identical species have the same time of flight. If follows that:

$$d_d = 2\sigma^{\frac{3}{2}}\left[\frac{1}{\sqrt{s_0}} - \frac{s_1}{\sqrt{s_0}}\left(\sqrt{\sigma} + \sqrt{s_0}\right)^{-2}\right] \qquad \textbf{(2.7)}$$

Solving either numerical or graphically provides a helpful starting input voltage range. Because of the rapid rise-fall times of the high voltage pulser the values determined from Eq. 2.7 were not the exact operating value used in the laboratory. This variation is attributed to the inductive and radio frequency (RF) contributions of the system experienced during rapid application of high voltages.[13] Experimentally the applied voltages were optimized at 3000V for the pusher plate, 2872.8V at the middle plate; the bottom plate being grounded to the chamber. The adjustable potentiometers between the first and second plates and second and third plates were set at 370.7Ω and 8.37kΩ respectively:

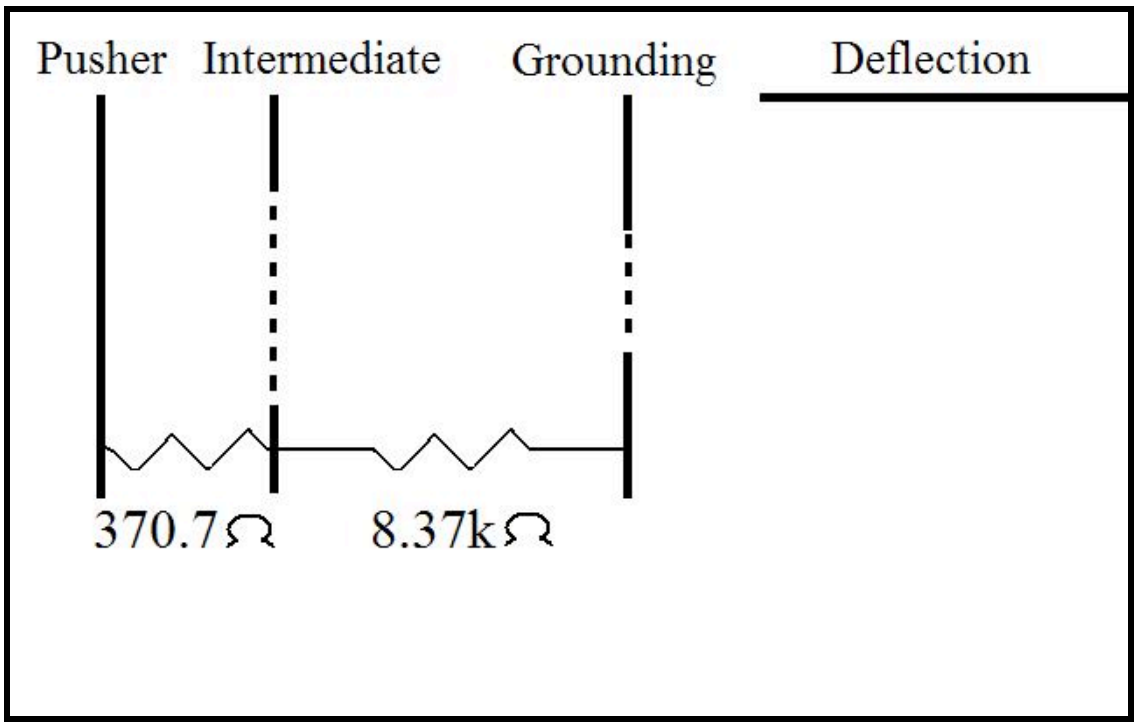

Figure 2.10. Extraction Region Resistive Distribution.

Thin-carbon resistive-film potentiometers were used to minimize inductive loads that could adversely affect the rapid voltage transmission. All HV internal wiring connections were made with tin-coated OFHC copper insulated with UHV-compatible non-inductive Voltrex tubing from SPC Technology Inc.

2.8 Tunable Laser System and Ionization Sources

Prior to application of a high voltage (HV) for extraction, it is possible to pump-probe molecular species by way of a number of available radiation sources. Both single and two-photon spectroscopy can be done; resonant two-photon spectroscopy (R2PI) most commonly of interest.

Laser sources have access to the HV extraction region via input and output 2" sapphire windows. Sapphire is the preferred material here as it is effectively optically

transparent for radiation between 200nm and 4000nm. UV quartz has also been used for select frequencies due to its lower cost.

2.8.1 Dye Laser System

The preferred tunable radiation source is a Continuum ND6000 dye laser. This system operates with a useful resolution/line-width of $< 0.05 cm^{-1}$. Pumped by a pulsed Continuum Surelite-I Nd-YAG at either 355nm or 532nm, the dye laser output is sent through a Spectra Physics WEX-1 package where output frequency doubling as well as sum-frequency and difference-frequency generation can be carried out, giving the total system an overall range of 250nm – 800nm. Different angle cut KH_2PO_4 (KDP) crystals are used for different frequencies of incident radiation. A mechanically coupled compensator crystal insures output light does not wander in target position. The near-infrared (NIR) region, 800nm - ~4000nm, is accessible with additional non-linear optics as well as utilization of the fundamental (1064nm) output of the pump Nd:YAG laser.

2.8.1 Optical Parametric Oscillator System

The second tunable laser system, a Continuum Surelite optical parametric oscillator (OPO) was also available. This system utilized a pump laser (Continuum Surelite-I Nd-YAG) to produce a tunable light output by way of the non-linear optical properties of a BaB2O4 (BBO) crystal. Incident 355nm light is converted to a selected output frequency and then angle compensated, through a second tuning crystal, to insure beam directionality. Although the BBO offers conversion efficiencies as high as 30%, the output line-width is of insufficient resolution for many gas phase spectroscopic techniques:

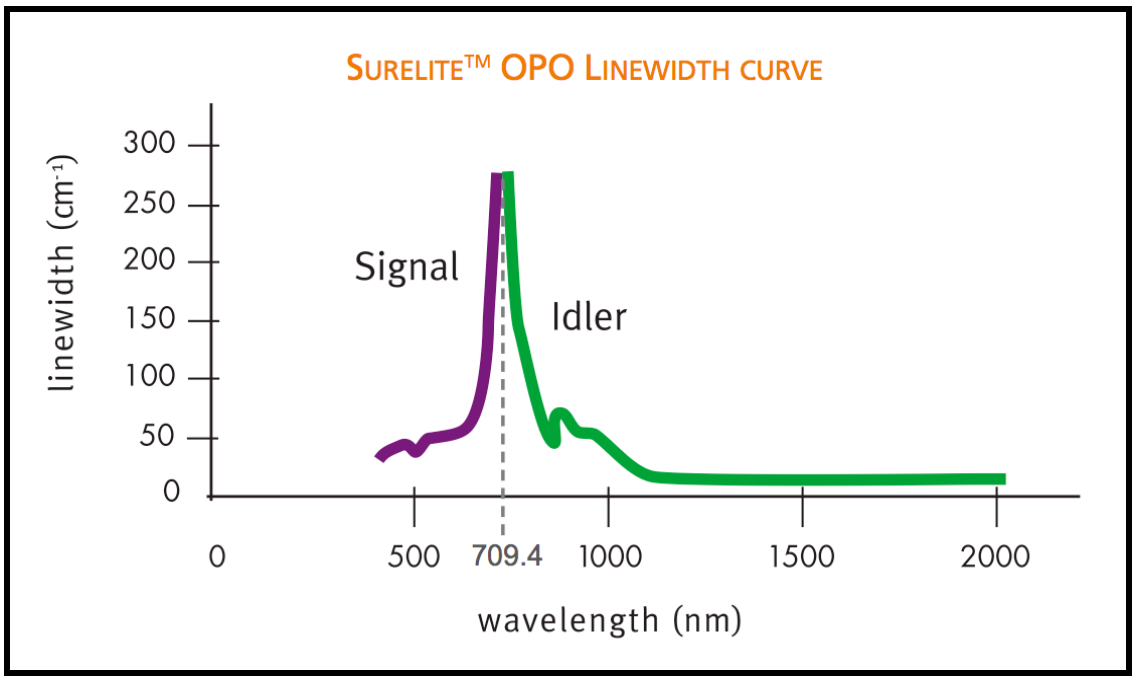

Figure 2.11. OPO Linewidth.[14]

It is, however, very well suited for rapid tuning for spectral-feature identification. Thereafter the higher resolution dye laser may then be used for high-resolution data acquisition.

2.8.2 Excimer Laser

In addition to the two available tunable laser systems, an ArF equipped Lambda-Physik Optex excimer laser was also available for ionization. This system, having an output of 193nm or 6.4eV, was the preferred laser to first-step identification of gas-phase species prior to spectroscopic probing. This system is especially useful for a number of various species because of its high ionization energy.

2.9 High Voltage Pulser and Tunable Extraction Region

The HV pulsar was designed and constructed around the HV transistor available from Behlke Power Electronics GmbH, model HTS-81. Capable of voltages as high as 8kV and rise times under 10ns, this HV switch is ideal for TOF applications. Construction was consistent with the manufacturers specifications:[15]

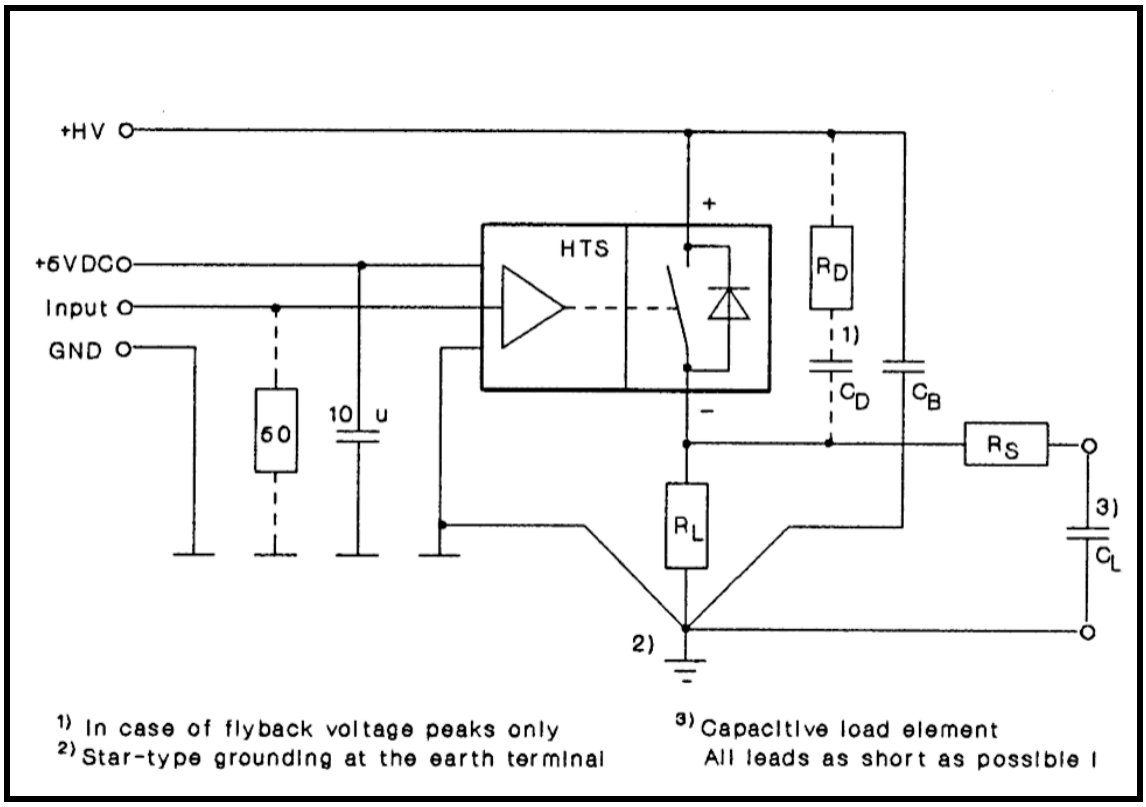

Figure. 2.12. HV Pulser Wiring Diagram.[15]

As shown in Figure 2.12, ±HV was supplied via a Bertan Associates 205A-05R HV power supply. An inline 0.5μF 8000V electrolytic capacitor, shown here as C_B, ensured a consistent and stable voltage during operation. The Behlke GmbH model HTS-81 HV switch was powered using a Digikey Inc. model 271-1100-ND 5Vdc 1.4Amp power supply. The switch power supply was stabilized with a 10μF capacitor to ground. The resistive load, R_L, is here the total resistance of the extraction region from Section 2.7.2, 8740.7Ω. R_D, C_D, R_S, and C_L, were installed with the manufacturer's recommended values.[15] The TTL trigger input was grounded with a 50Ω resistor to impedance match the BNC signal cable from the delay generator.

Since both positive and negatively charged ions were studied, a set of heavily insulated and isolated input-outputs posts were fabricated from polycarbonate plastic:

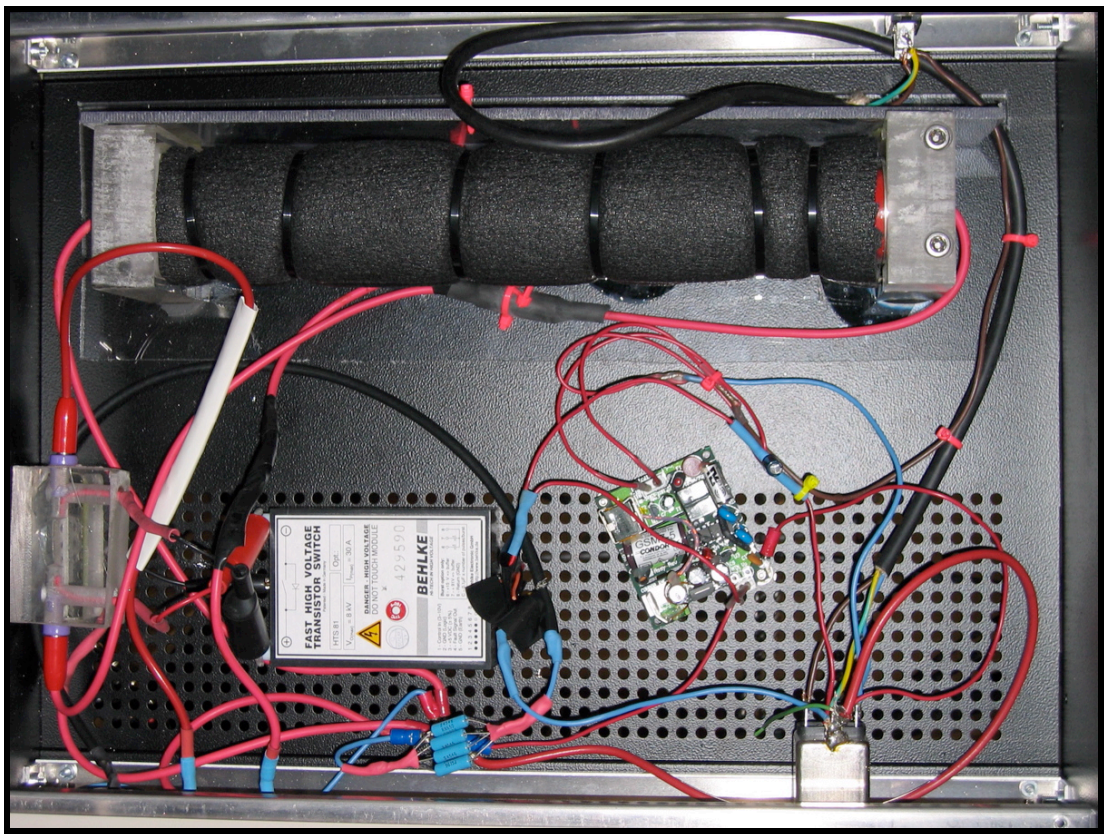

Figure 2.13. HV Pulser Enclosure.

Alligator clips as well as a banana plug binding post allowed the for a quick (and safe) reversal of the input voltage from the HV power supply, to the voltage regulating capacitor, and finally into the Behlke HTS-81 switch. Failure to reverse the input potential when changing from anion to cation mode sampling would result in catastrophic failure of the switch.

2.10 Drift region

The drift region consisted of a vertically oriented 50cm unobstructed length for ion separation to occur. The entire region was held at ground, with multiple redundant connections made, and had an ion pressure gauge offset on an inline t-junction to monitor

detector pressure exposure. A T-316 500 mesh stainless-steel screen provided screening from any stray electric fields that the ion gauge might produce. 2 ¾" conflat hardware and coupling nipples were used throughout.

2.11 Microchannel Plate Detector

2.11.1 Design

The microchannel plate (MCP) detector employed was of the typical chevron configuration, having two parallel MCP's spaced 150μm shown here:

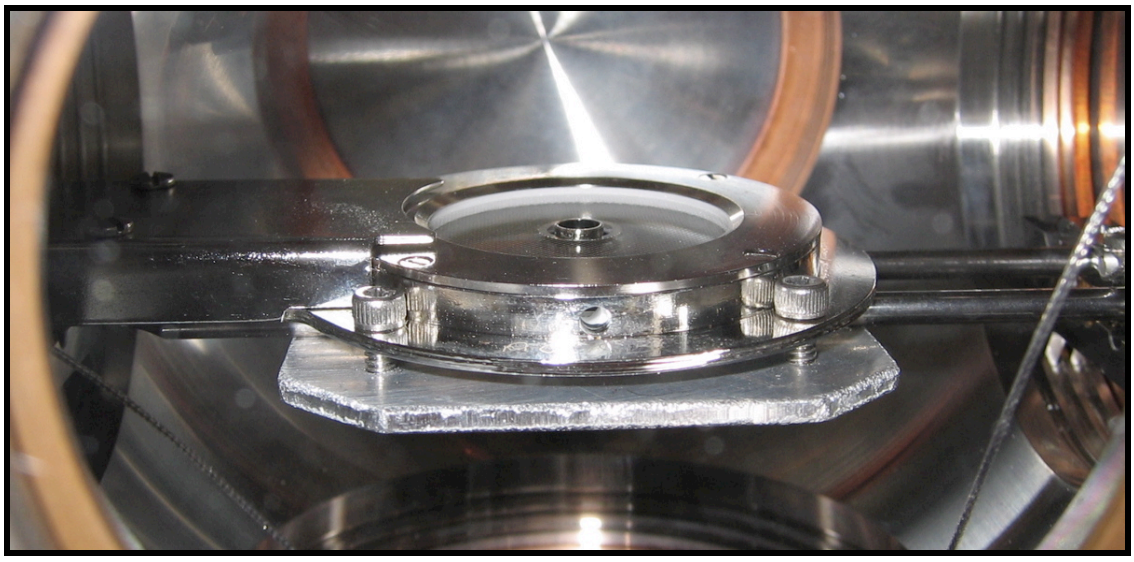

Figure 2.14. MCP Detector Installation.

Special center-hollowed MCPs are used here, having the ability to be utilized in a coaxial-reflectron configuration not yet realized. The individual MCP plates are nominally 32.66mm in diameter, having an active diameter of 25.4mm minus the 8mm center hole (456.4mm^3 active area). Microchannels are 10μm in diameter and are at the

standard offset angle of 12°. A Nickel 500 mesh screen sits 250μm above the first MCP so as to ensure incoming ions experience a zero electric field in the drift region. Below the second MCP is conical T-304 stainless-steel anode which is coupled through a UHV electrical feed-through for signal acquisition. In cation-mode the output signal is immediately grounded by way of a 50Ω resistor for impedance matching with the following data acquisition electronics. During anion operation, when the MCP detector anode is floated at high voltages, a 120pF capacitor couples the output signal also having a 50Ω grounding resistor immediately thereafter for impedance matching.

Residual gas in the drift region and species introduced by the HV extraction region are pumped by an 8" CF Pfeiffer-Balzers TCP 380 turbo-molecular pump directly behind the MCP detector assembly. The turbo is roughed by a Pfeiffer-Balzers DUO 016B rotary vane pump.

2.11.2 Voltage Distribution

An external Bertan Associates 205A-05R HV power supply is used to distribute appropriate voltages across the MCP assembly for cation and anion operation:

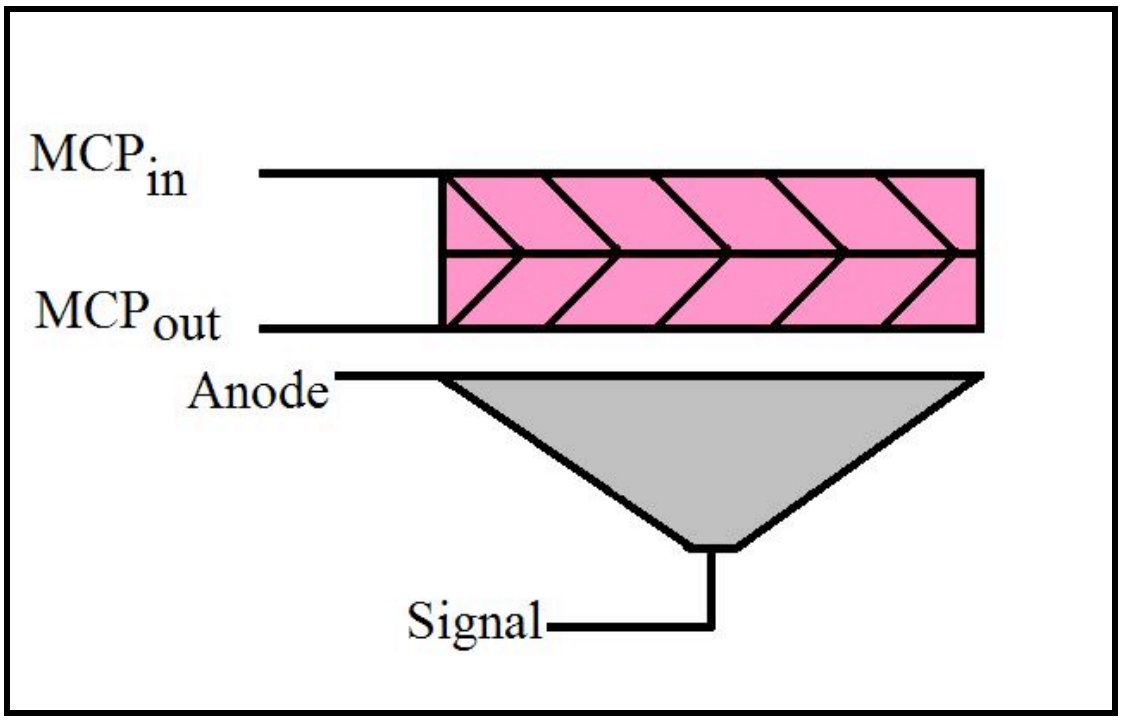

Figure 2.15. MCP Detector Schematic.

With an HV divider providing the appropriate voltages by way of resistive voltage distribution:

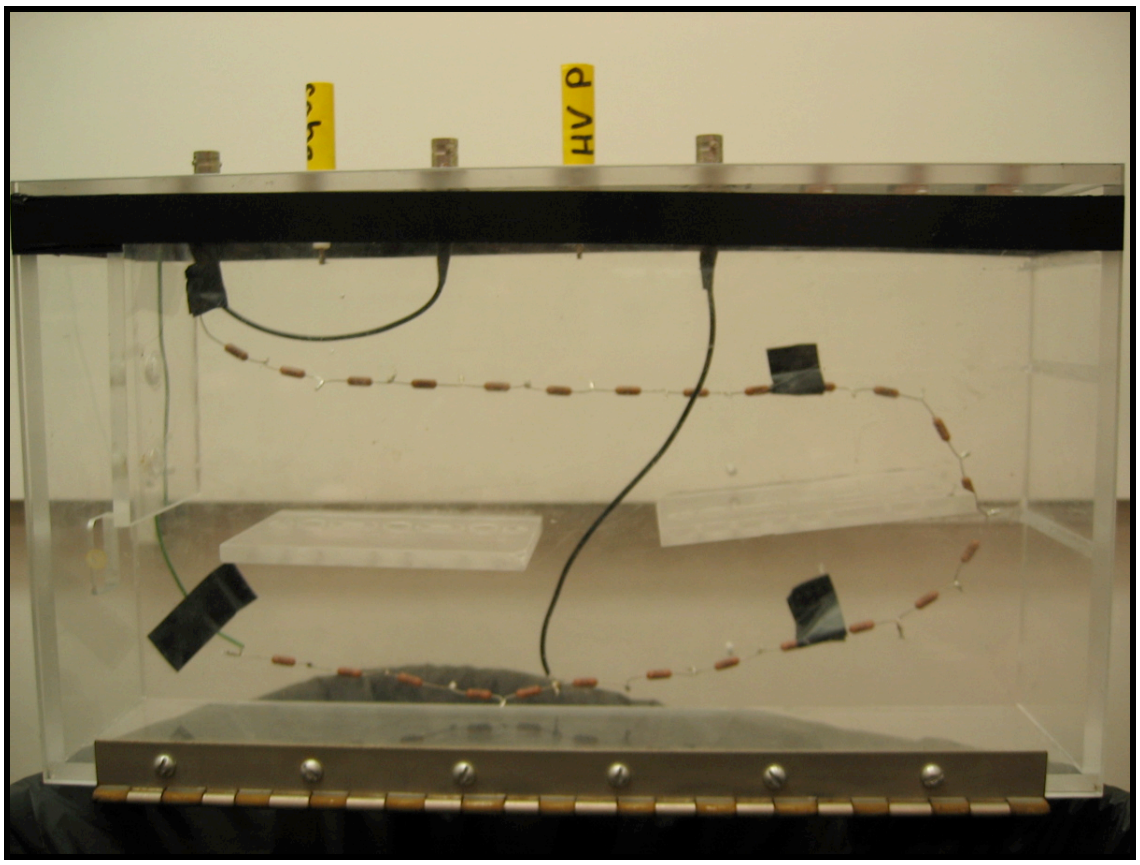

Figure 2.16. MCP HV Divider.

2.12 Signal Acquisition

The impedance-matched output from anode of the MCP detector was immediately sent to a custom 150MHz preamplifier. The preamplifier utilized a Comlinear Corporation CLC501-AJP-MI military-spec fast video amplifier. Having a slew-rate of ~1200V/μs and a usable operating speed of 120MHz, this pre-amplifier configuration provided more than enough time resolution[13] for the intended applications of the custom TOF mass spectrometer.

Signal from the pre-amplifier was split and simultaneously sent to a Tektronix TDS-220 100MHz - 1GS/s scope for real-time monitoring as well as to a Lecroy 9370 1GHz - 1GS/s scope for data acquisition.

2.13 Timing and System Control

Timing control was provided by the use of two Stanford Research Systems Inc. delay generators, Model DG 535. Specific control of all involved electronics, laser systems, etc. utilized control commands carried through USB, RS232, and GPIB connections. Custom visual basic-based software, developed by Dr. Gregory Grieves, was modified and readily implemented.

A typical timing scheme requires taking into account the associated delays with various components. Whereas the excimer laser has a delay in the low nanoseconds, the Nd:YAG requires a charge signal ~186μs prior to sending a trigger signal. The gas valve, being mechanical and thereby inherently slow to respond, can require hundreds of microseconds between sending a trigger signal and the poppet actually opening. The standard beginning sequence follows:

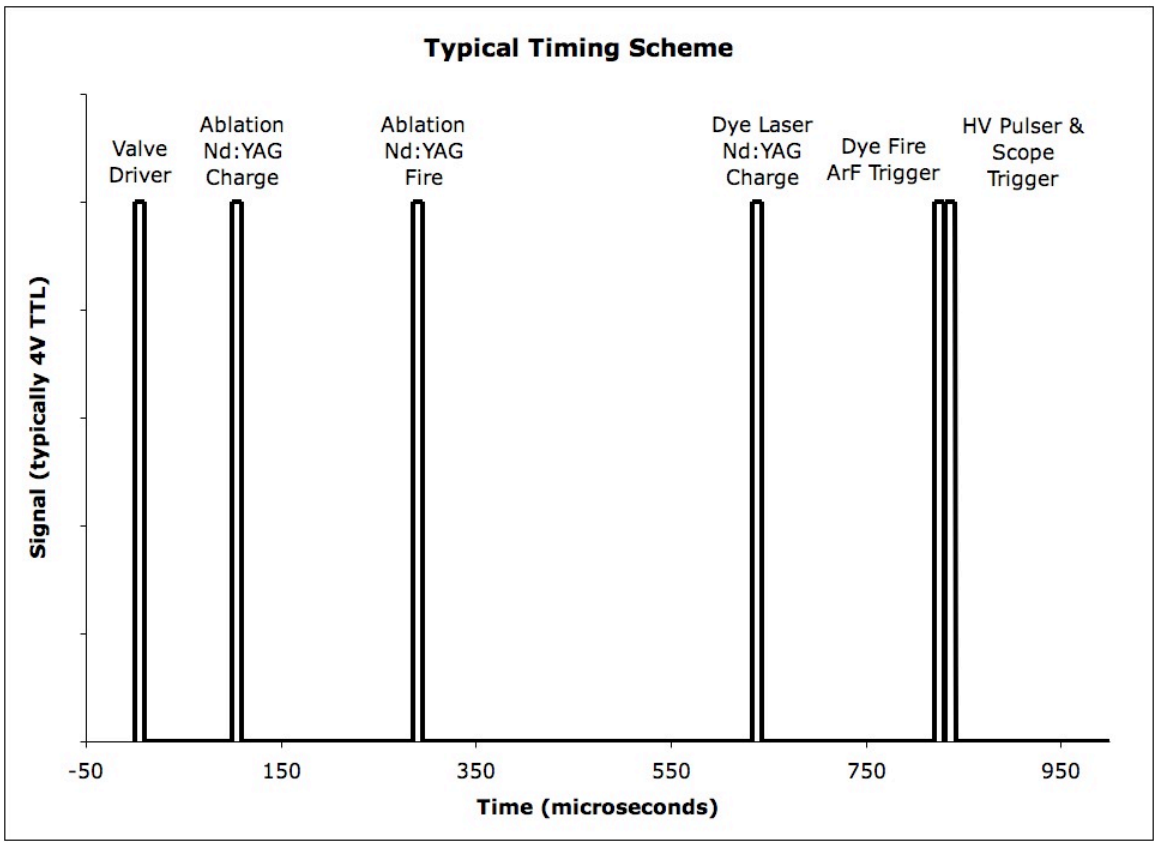

Figure 2.17. Typical Timing Scheme.

Here the valve driver output, using its' internal clock, represents T=0. At 100µs a TTL signal is sent to the ablation Nd:YAG to charge followed by another signal, 186µs later telling it to fire. After 348µs, a charging signal is sent to the dye pump-laser, with a fire signal the same 186µs. The Dye fire signal is split and also sent to the excimer trigger input. At ~832µs a signal is sent to trigger both the data acquisition scope as well as the HV pulser. This signal is 5µs in length so as to limit damage to the HV MOSFET from prolonged power output.

CHAPTER 3

NACL CLUSTERS AND ATMOSPHERIC WATER ADSORPTION

3.1 Introduction and Background

Oceanic sea-salt is one of the most abundant cluster species in the atmosphere.[16] Worldwide seawater has an average NaCl concentration of ~0.6M,[17] enabling lunar and storm driven tide wave-action to provide a constant and significant supply of aerosolized salt species to the atmosphere.[16] The role of gas phase NaCl species is suspected in many atmospheric chemical reactions though many, if not most, of the specific physical contributions remain unknown.

For its significant role in the development of humanity, the specific chemistry of NaCl remains somewhat elusive. Historically, salt has played an extraordinary role in human civilization. Aside from being a biological necessity, accounts[18] of the harvesting or mining of salt date back as far as 6000B.C. to central-east China (Shanxi region). Salt addition has long allowed for the preservation of foods, most notably meats during early civilization's travels to survey and inhabit the planet; a practice still used today. For modern industry salt is a common and necessary component in a vast number of chemical processes. Notable is salt's role in the manufacturing[19] of everyday consumables such as paper, textiles and fabrics, soaps and detergents, and any number of other products too voluminous to mention here.

In the realm of fundamental science, the hydration and dissolution of NaCl clusters is of significant interest both in their role in atmospheric processes as well as offering insight into the dissolution kinetics of alkali-halide salts. The full understanding

of their chemical activity, such as possible catalytic sites for the destruction of tropospheric ozone or as deliquescent agents, remains deficient.

The rudimentary understanding of the solvation of salts, with varying size and defect density, played a crucial motivation for further investigation. Indication of their presence in interstellar dust grains[20] also demands a complete understanding of all possible chemical processes. An exceptional collection of literature on dry NaCl clusters exists, both experimental[21,22,23] and theoretical,[24,25,26] describing predicted and confirmed[27] structures. Investigations of water on bulk salt surfaces[28,29] have also existed for some time and are relatively numerous. A small collection of studies[30,31] exists for the hydration of smaller (Na_nCl_n: $n \leq 6$) clusters species but are, at best, only tangentially related to the atmospheric analogue. More common in the literature are studies on NaCl parallels, such as NaI[30] and other alkali-halide species. Prior to this investigation, adsorption on NaCl clusters was only vaguely understood and specific to very small unique and large bulk species. The size-scale transition region, presumed to offer the most insight as to the driving kinetics that lead to aggregation in the atmosphere, was studied in detail for a select group of exclusive species under atmospherically relevant conditions.

Previous studies undertaken by this group[32,33] have provided a considerable amount of insight into the topic. A sizable knowledgebase made this undertaking particularly attractive. Through serendipity, what was originally thought to be an erroneous data set led to the more complete and descriptive understanding of the atmospheric salt hydration system.

3.2 Sample Preparation

For experimental preparation, a 1/8” cylindrical LDI target rod was prepared in a custom hydraulic die (Section 2.4) using 99.999% (by %weight metal impurity) granular sodium chloride (Alfa Aeser #10862). Approximately 2 grams of salt were placed inside the hardened high-carbon steel die and pressed, with a tungsten rod, at approximately 7500bar. The resulting salt sample was attached with cyano-acrylate glue to a ¼” carrier sleeve (Section 2.4) and placed in the reactor assembly:

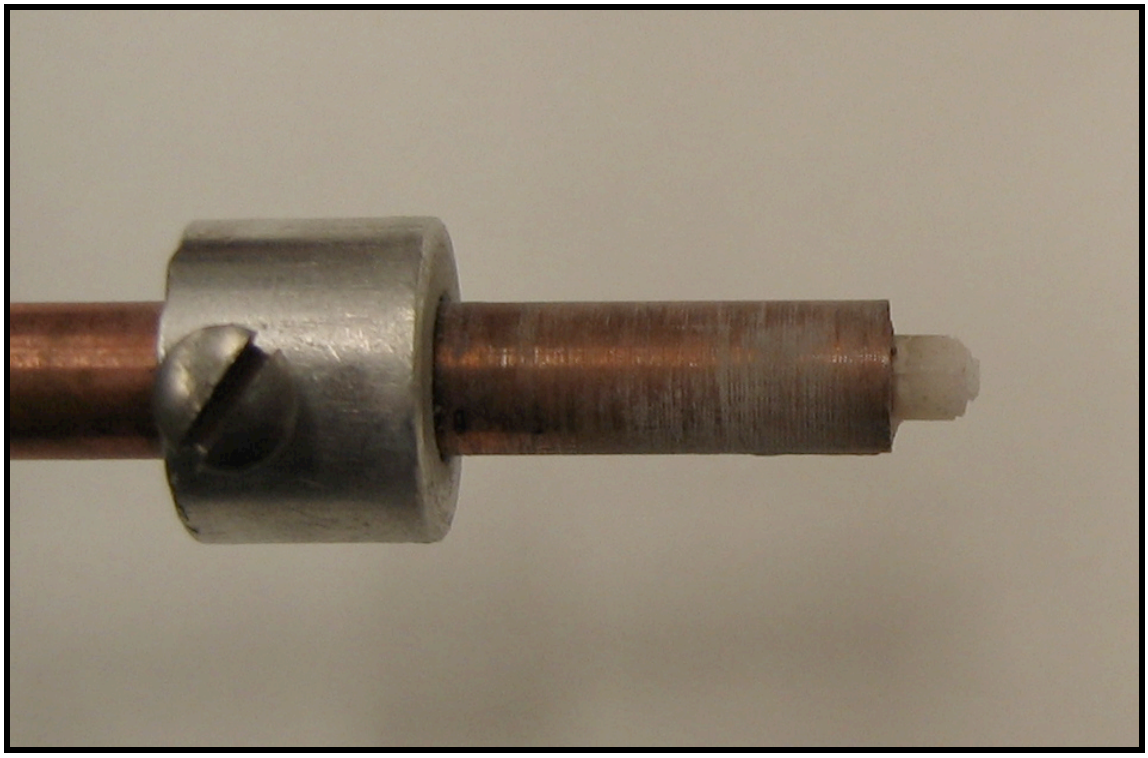

Figure 3.1. NaCl Target Rod.

A great deal of trial and error transpired in attempts to prepare the salt target. Previous work with salts and assorted varieties of organic components, such as para-amino benzoic acid (PABA), showed that small additions of a select liquid maximized the yield and quality of the target. After exhausting numerous readily available additive liquids, it was determined that the presence of a small quantity (< 200μL) of cyclohexane provided the highest quality salt sample. Discussed in Section 3.53, only a trace amount of the cyclohexane remained and had a negligible effect on the specific chemistry investigated.

3.3 Experimental Method and Parameters

Salt clusters were produced by the LDI cluster source described in Section 2.3. The frequency-tripled output of a Nd:YAG laser (355nm) was determined the most effective ablation source as compared to the frequency doubled (532nm) and fundamental (1064nm). High purity helium carrier gas, seeded with water vapour via an inline bubbler (Section 2.5), was introduced into the reactor at a total pressure of ~0.5bar. For collection of dry NaCl cluster mass spectra, all carrier gas plumbing, starting at the He gas storage cylinder, was evacuated using a Edwards Inc. Stage-2 (#5) rotary vane pump and left overnight. An inline helium purification filter, UOP Inc. model P-1002, was placed at the output of the helium gas regulator. Regular maintenance and cleaning of this inline filter ensured that no unknown gas phase reactants entered the reactor assembly.

The ablation laser was set for a charge-trigger time of 186μs. The inline iris was adjusted to provide approximately 10-15mJ of energy per pulse. Optimized delay times between the firing of the Nd:YAG and the opening of the ultra-fast valve, having a pulse-width of ~300μs with a backing pressure of approximately 7bar, was found to be ~210μs. The delay time between the ultra-fast valve and HV pulser was set at ~350μs. Assuming

a molecular beam speed of ~130,000cm/s and a distance between the reactor and HV extraction region of 28.5cm, the cluster aggregation and resident-thermalization time was approximated at ~120μs. This time scale insured that any significantly high-energy metastable species would not survive long enough to escape the reactor assembly in the molecular beam. The applied deflection voltage was varied from 0V to 120V to ensure efficient collection of the entire mass range of species formed in the reactor assembly. Subsequent mass plots were normalized and combined to display this complete hybrid spectrum. Experiments were carried out at 298.15K ± 3K offering an environment slightly less conducive to aggregation than that of higher elevation atmospheric events. Atmospheric events typically occur at temperatures ranging from 243K – 283K, being a function of their altitude.

3.4 Computational Method and Parameters

In addition to experimental data and analysis, it was deemed absolutely necessary to execute a theoretical and computational study of any unique or subsequently odd acting species. Because of the variety[34,35] of structural predictions available for alkali-halide clusters, relative energies were needed for comparison. Additionally, because of the presence of water during ablation and coalescence, alternative structural predictions were essential so as to investigate thermodynamically favorable structures integrating the water into the energetic considerations.

All calculations were performed with the Spartan ’04, version 1.0.3 package, using an Apple Dual G5 desktop configured with 4GB of RAM. The optimized ground state structures were obtained using DFT calculations with the B3LYP hybrid density functional model and a 6-31G* basis set. All of the structures obtained represent local

minima, i.e., all of their vibrational frequencies were real. The ground state structures obtained for the non-hydrated NaCl clusters agreed with those given in the various sources of literature[1]. The hydration bond energy ΔE_e was computed as the difference between the electronic energies of the hydrated cluster and the non-hydrated cluster. The vibrational, rotational, and translational contributions to the thermodynamic quantities H, S, and G were calculated by Spartan for an ideal gas at 298 K and 1bar. ΔH, ΔS, and ΔG for the hydration of a cluster were calculated by combining these results with ΔE_e. The value of ΔE_e for the $Na_{14}Cl_{13}$ and $Na_{13}Cl_{14}$ clusters could only be estimated due to computer limitations. An approximate structure of the bare cluster was obtained by using the Spartan MMFF molecular mechanics model. Although these select clusters were far too large for energy optimization, the single point DFT energy could be calculated for $Na_{14}Cl_{13}$. With H_2O added, all of the Na and Cl atoms in the cluster were spatially frozen, and an energy-optimized structure could be obtained. A single point DFT energy could not be calculated for the $Na_{13}Cl_{14}$ cluster.

3.5 Experimental Results

3.5.1 Dry NaCl Cation Mass Spectrum

The dry cation mass spectrum clearly demonstrates what is effectively common[21,22,23] in mass spectrometry of alkali halides. Due to the Cl^{35}:Cl^{37} distribution of ~3:1, exacting identification can be made by mass assignment and relative isotopic abundance. Species in the lower (<m/z 600) region vary moderately in relative population. The most abundant species here, Na_7Cl_6, is only ~3 times more abundant than the scarcest Na_3Cl_2 and Na_4Cl_3:

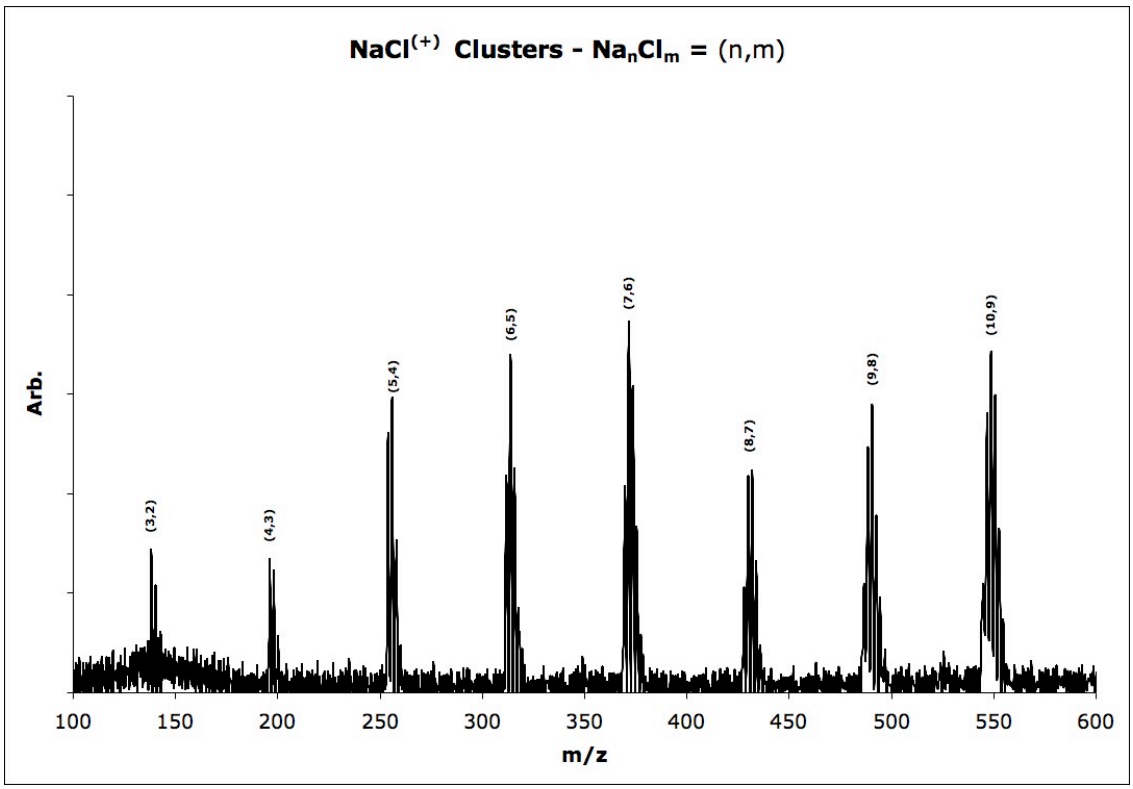

Figure 3.2. Dry NaCl Cation Mass Spectrum m/z 100-600.

In this lower mass region the most diverse variety of structures exist. Discussed in detail in Section 3.6, these structural configurations contribute significantly to their overall interaction with water molecules.

In the higher mass region (m/z 600-1200), the most favored cluster is the $Na_{14}Cl_{13}$, being a highly stable 3X3X3 cube. Relative abundances vary considerably more here than is seen in the lower mass range. The majority of these species, discussed in detail in Section 3.6, adopt the bulk structure, having one or more structural defect inclusions owing to the missing chlorine ion. The presence of the (14,12) species (singly charged) is attributed to the F-centre, or colour-centre, configuration with a free electron taking the place of a chlorine ion:[35]

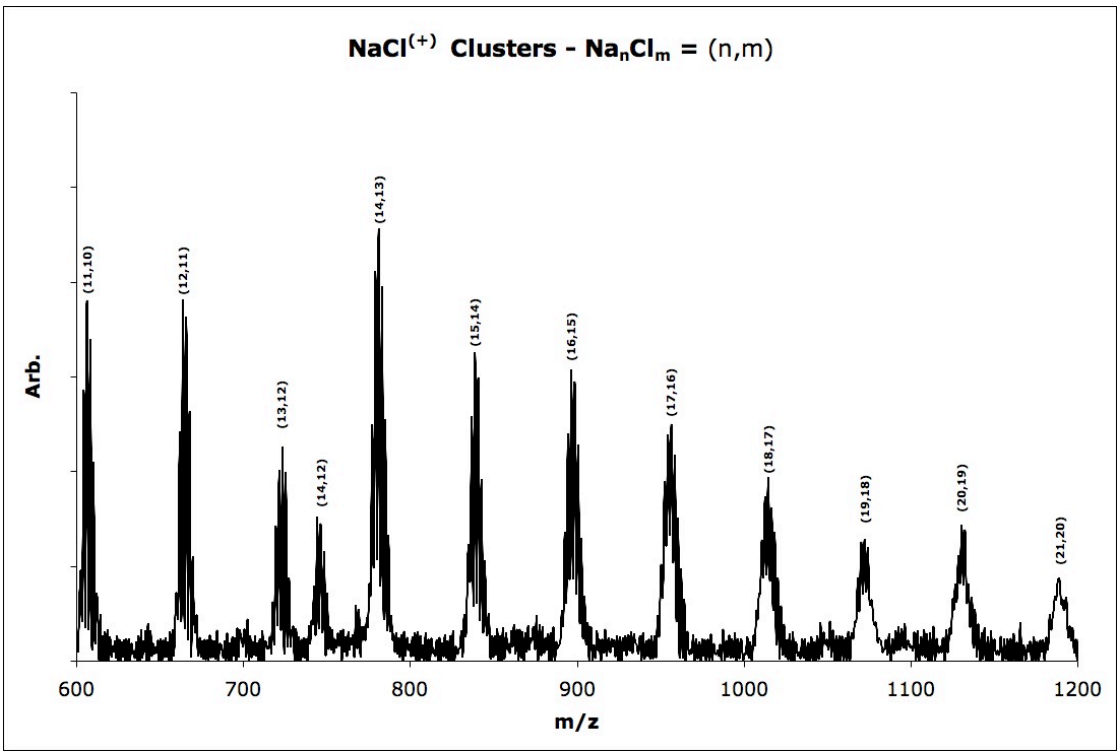

Figure 3.3. Dry NaCl Cation Mass Spectrum m/z 600-1200.

3.5.2 Hydrated NaCl Cation Mass Spectrum

In the presence of water, the relative population of the smaller various dry clusters changes little as a function of cluster type (including hydrated species); testament to the salt clusters' preferential formation without internal defects:

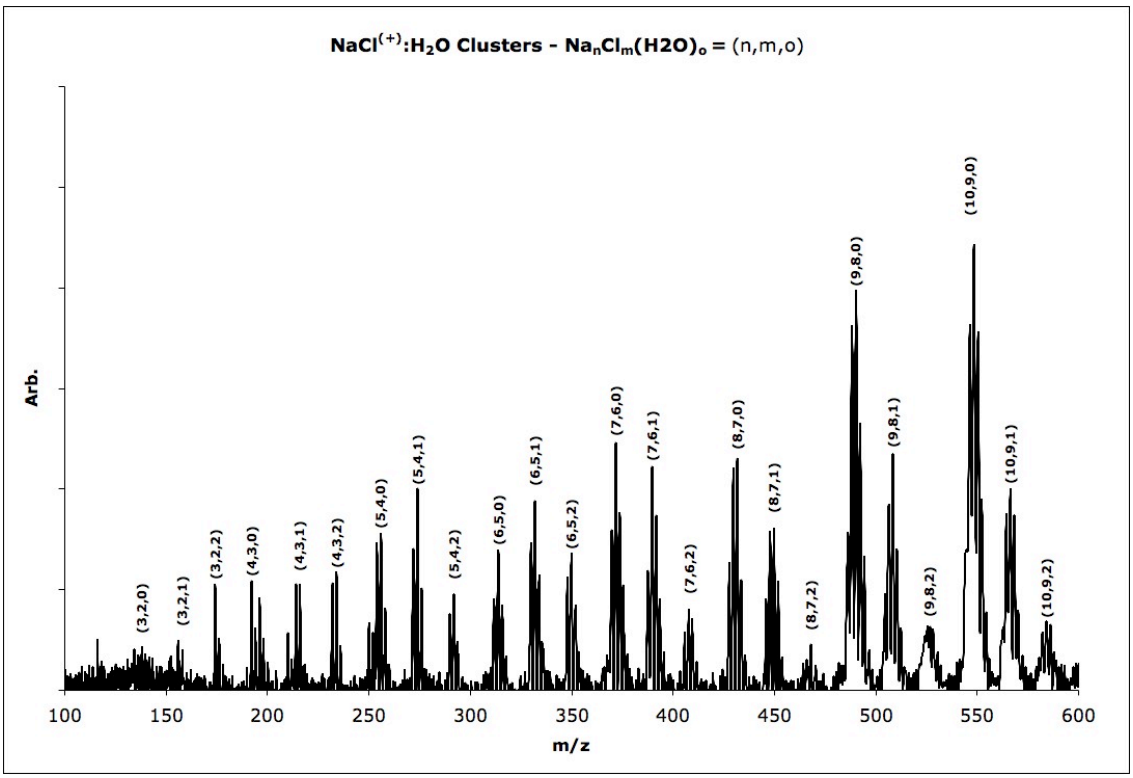

Figure 3.4. Hydrated NaCl Cation Mass Spectrum m/z 100-600.

There is however, an enormous reduction in dry clusters, relative to those hydrated, in the sub-500 m/z region. This region shows multiple adsorption of water molecules for every cluster. Detailed investigation of the mass spectra shows, resolved by isotopic splitting, that some species, including the Na_4Cl_3 and Na_3Cl_2, readily coordinate with three water molecules.

For the > m/z 600 mass region, relative populations of the larger various dry clusters changes little, similar to their smaller brethren. The quantity of hydrated species is however in stark contrast:

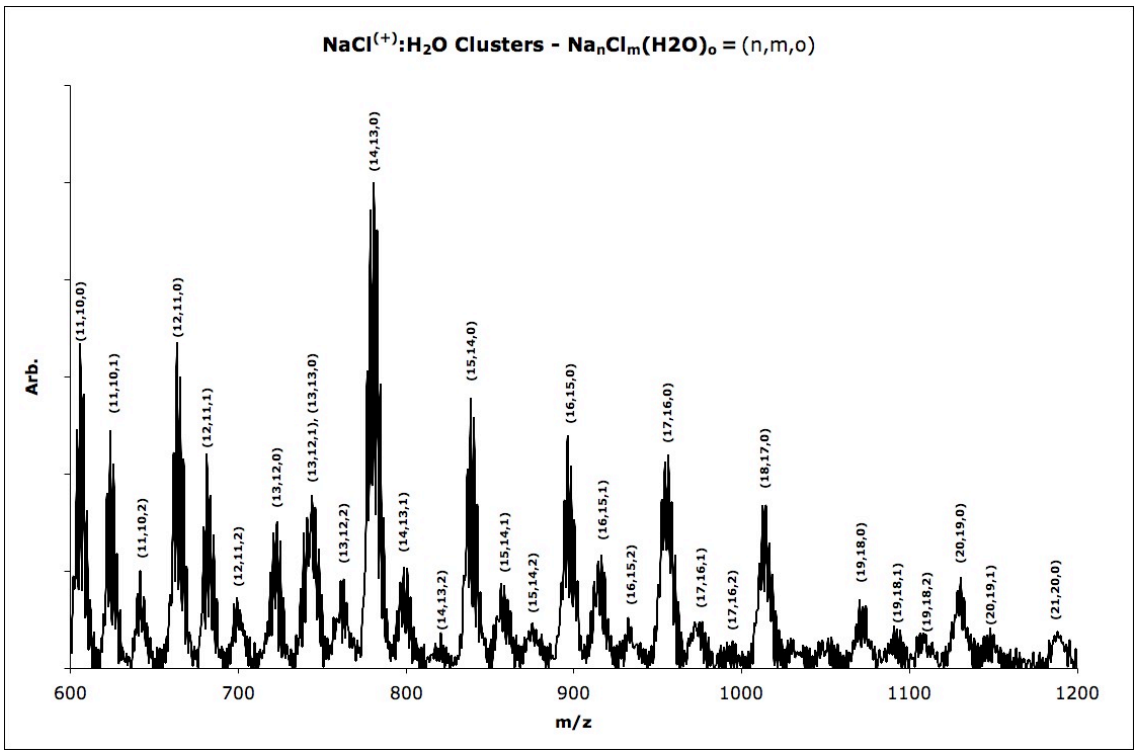

Figure 3.5. Hydrated NaCl Cation Mass Spectrum m/z 600-1200.

The dry $Na_{14}Cl_{13}$ still dominates the landscape with an effectively identical distribution of other dry species. Albeit small, a trend follows in linear fashion displaying a reduction in adsorption as a function of size.

When these adsorption trends are compared to the relative yields seen in the smaller mass region, a considerable variation is readily apparent. Figure 3.6 shows the overall reaction yield for zero, one, and two water adsorptions as a function of the number of sodium ions present for the cationic clusters:

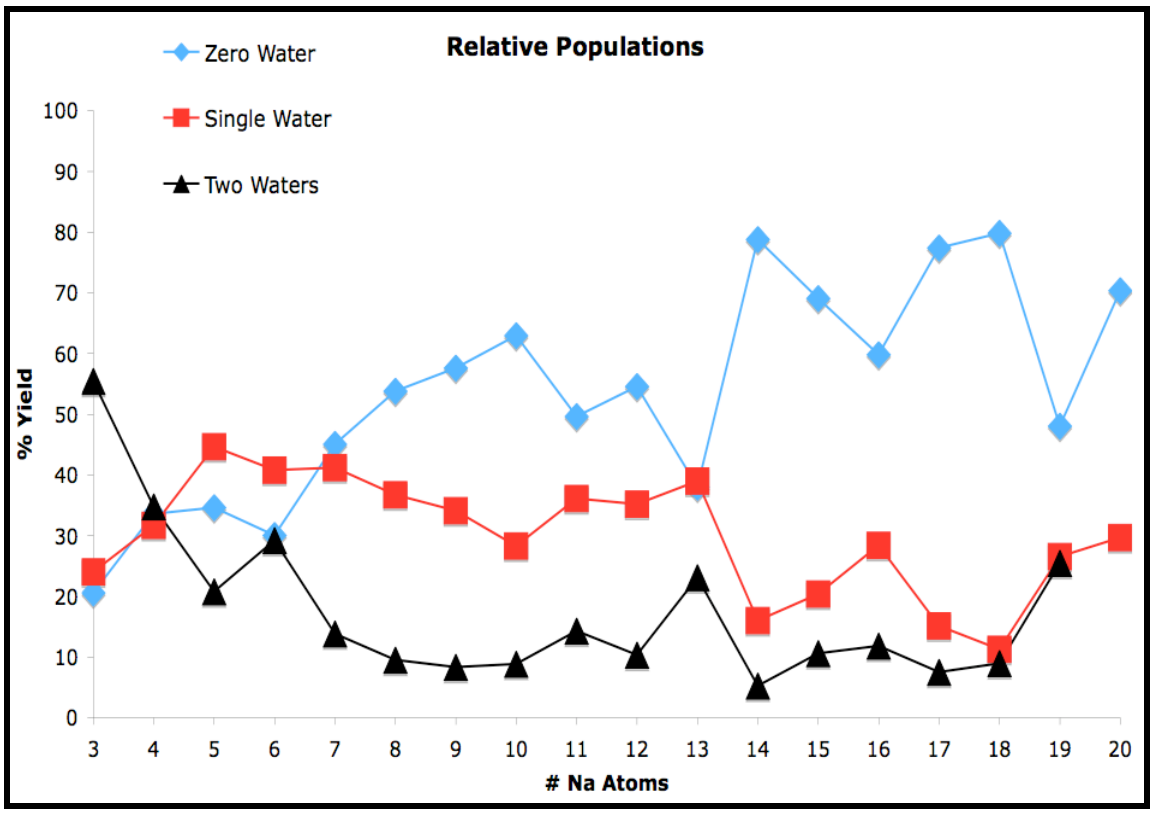

Figure 3.6. NaCl Cation Absorbance Yield.

With the exception of the $Na_{16}Cl_{15}$ and $Na_{19}Cl_{18}$ species, both having highly exposed defects, the larger mass region presents an enormously smaller adsorption yield when compared to the smaller species. Above m/z 600, more than 70% of the total cluster population succeeds in remaining dry. In the lower mass region, polar opposite to the heavier clusters, more than half the species in the < 600 m/z region are found hydrated in aggregates containing one or two waters.

3.5.3 Dry NaCl Anion Mass Spectrum

The anion mass spectrum, which shares superficially identical structural ionic bond networks albeit with chlorine and sodium exchanged for almost all clusters, shows a very linear overall distribution of species in the lower mass region:

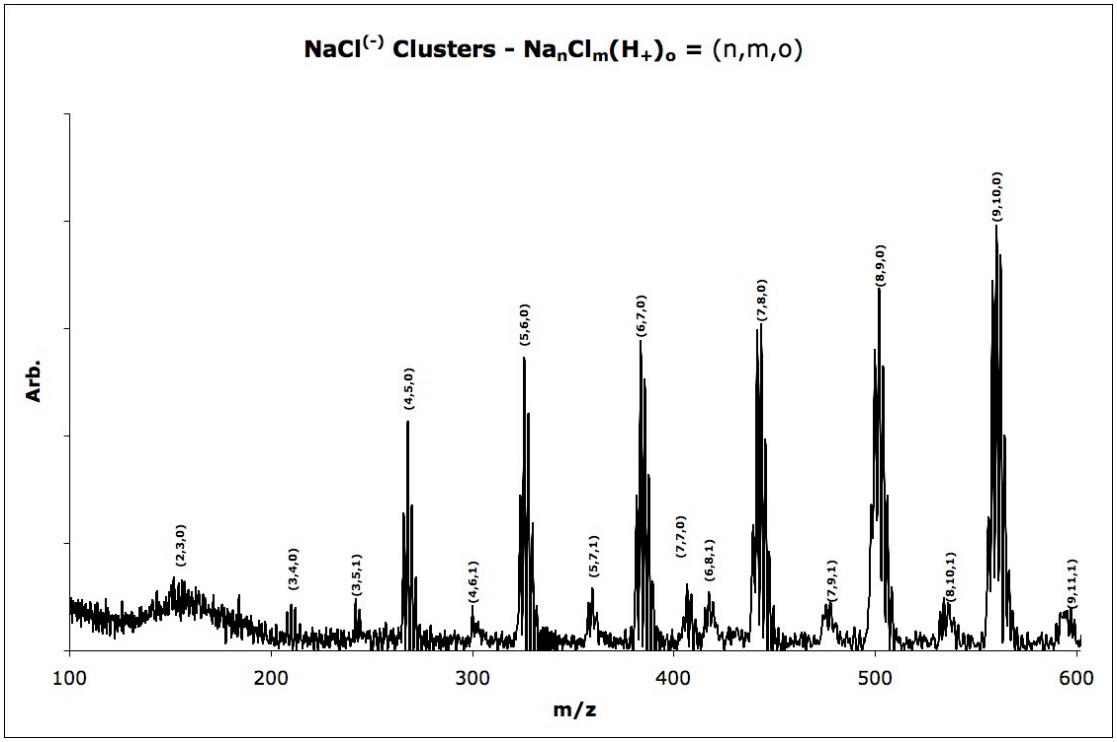

Figure 3.7. Dry NaCl Anion Mass Spectrum m/z 100-600.

Most apparently different relative to the cation spectrum are the Na_2Cl_3 and Na_3Cl_4 abundances, being considerably lower relative to the positively charged Na_3Cl_2 and Na_4Cl_3. This difference is likely due to the larger size of the chlorine atom, making small, less stabilized clusters less energetically favorable. This is also the likely explanation for the well-nigh equivalent population of the larger species in the low mass region.

In the higher mass region, a marked difference in overall relative populations is observed. The prominently expected $Na_{13}Cl_{14}$ instead follows in an overall linear trend of abundance as a function of size. This observed equivalence or linearity is attributed to the relaxation of the chloride tending outwards from the cluster surface,[36] as seen in bulk salt surfaces, lending to a higher self-stabilization capacity:

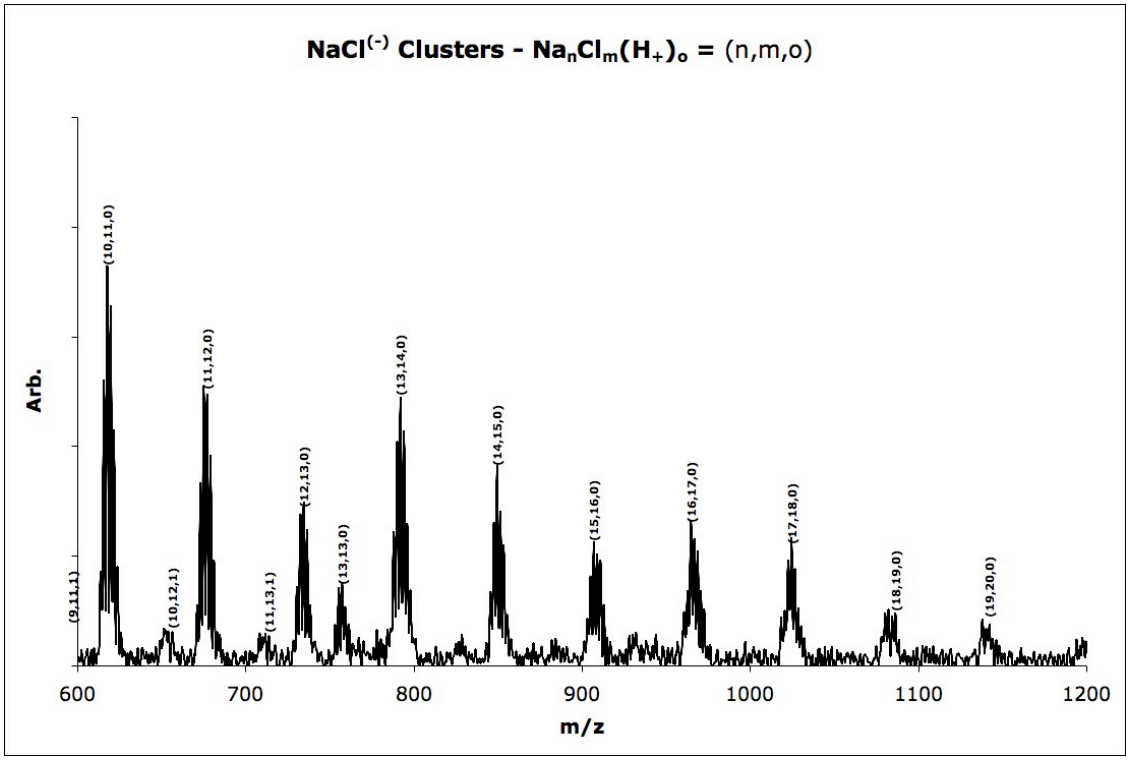

Figure 3.8. Dry NaCl Anion Mass Spectrum m/z 600-1200.

One peculiarity present in the anionic spectrum is the series of species with the addition of a hydrogen chloride unit. These doubly halogen-excessive clusters are likely of considerable interest but are not pursued here. Their presence is attributed to trace

amounts of residual cyclohexane included in the target rod from the hydraulic fabrication process.

3.5.4 Hydrated NaCl Anion Mass Spectrum

In sharp contrast to the highly efficient aggregation of water and NaCl seen with cationic species, the anionic salt clusters are, relatively speaking, almost effectively inert. No adsorption is observed prior to the Na_6Cl_7 cluster, having a yield much lower than that measured for the cations:

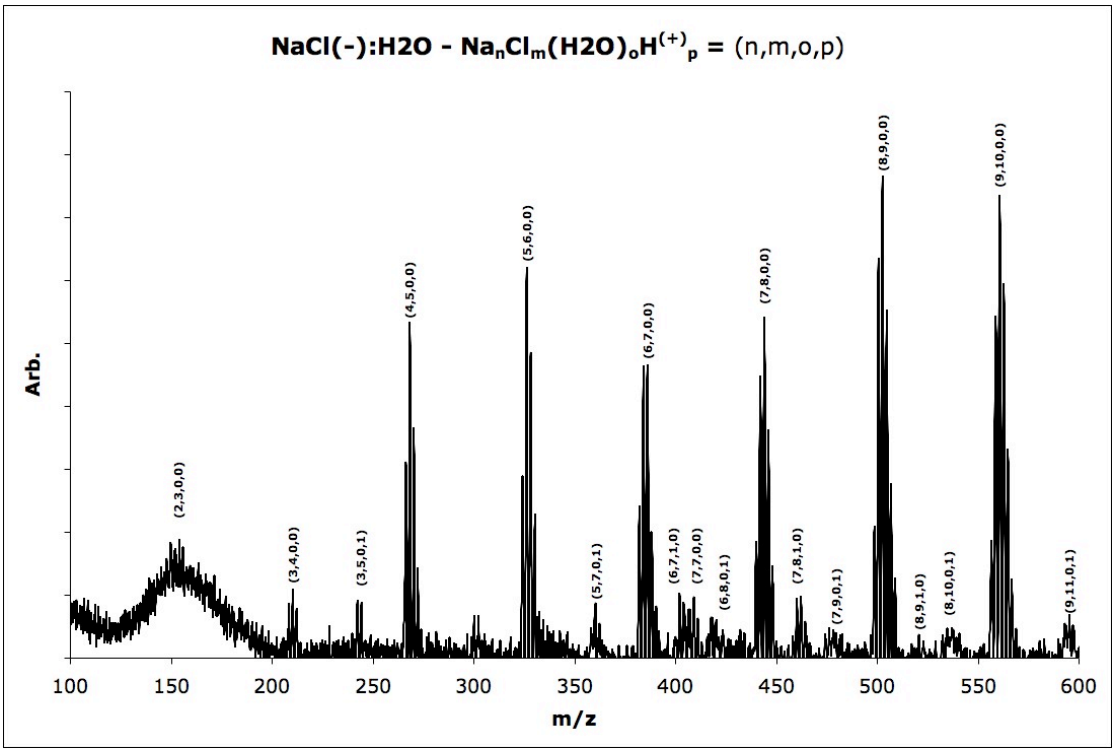

Figure 3.9. Hydrated NaCl Anion Mass Spectrum m/z 100-600

In the lower mass region the Na_7Cl_8 and Na_8Cl_9 species are also seen to adsorb water but to an even lesser extent. In the higher mass region there is little change in trend. Only the $Na_{14}Cl_{15}$ cluster is observed to adsorb water:

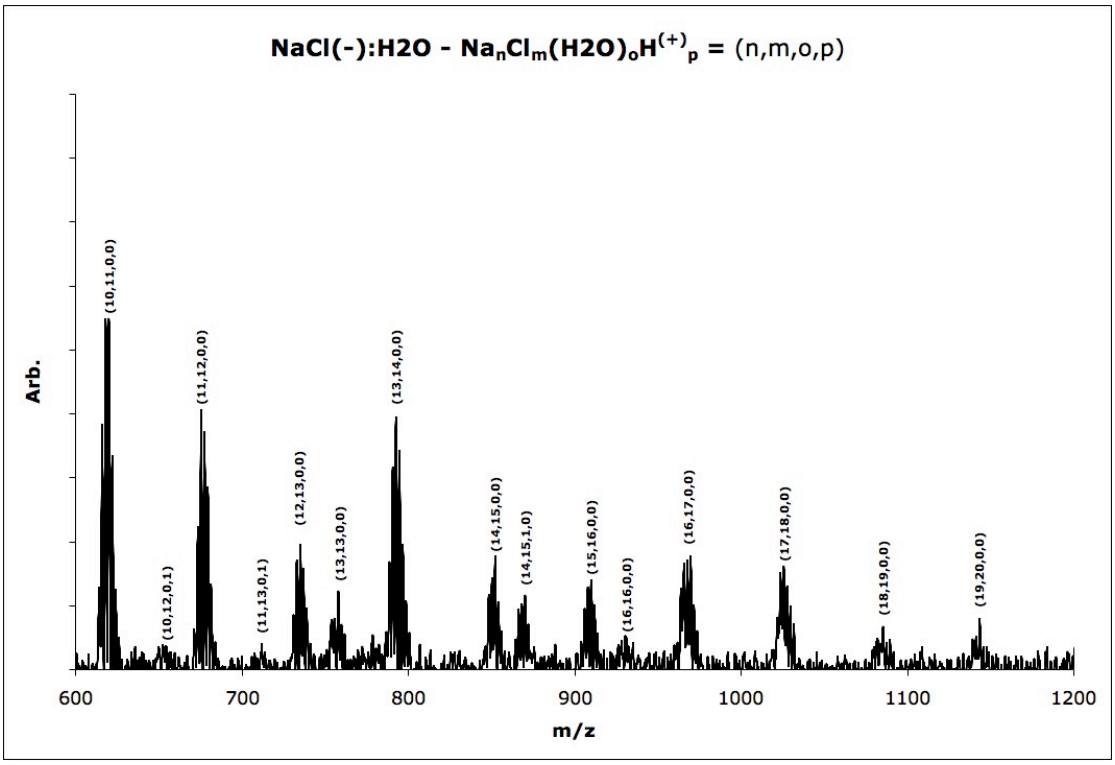

Figure 3.10. Hydrated NaCl Anion Mass Spectrum m/z 600-1200.

The relative yield of this adsorption is anomalously high but is unfortunately beyond the available computational ability. The previously predicted structure[32] of $Na_{14}Cl_{15}$, by way of the classical Born-Mayer potential, has an exceptionally high defect density across one of its' leading edges, likely here providing a spatially attractive match for adsorption. In general the overall reactivity of the anionic salt clusters with water is substantially less than that of the cations.

3.6 Cation Computational Results

Computational analysis was undertaken for select species, structurally having a marked variation from the bulk structure. Within the limits of the computational hardware available, these results all represent converged real-solution structures. Structures are in good agreement with previous studies[34] using lower level calculations. Bond lengths, on the order of 2.2-2.3Å, are considered realistic and well within the expected range. For the cationic clusters, nearly all considered species showed strong reaction exothermicity:

Table 3.1. Cation Computational Reaction Values.

Cations					
$Na_nCl_m^{(+1)}$ (n,m)	ΔE (kcal/mol)	ΔH (kcal/mol)	ΔS cal/mol·K	ΔG kcal/mol	BL (angstroms)
(4,3) corner	-22.8	-21.2	-22.4	-14.5	2.23
(4,3) face	-21.1	-19.6	-21.4	-13.2	2.24
(5,4) corner	-21.9	-20.4	-20	-14.4	2.24
(5,4) face	-18.2	-16.7	-27.1	-8.6	2.24
(7,6) top	-22.6	-21	-24.5	-13.7	2.23
(7,6) bottom	-21.9	-20.3	-23.9	-13.2	2.24
(7,6) middle	-21.1	-19.5	-25.3	-12	2.23
(14,13) corner	-17.2	N/A	N/A	N/A	2.23

Most calculated values for ΔE, ΔH, ΔS, ΔG are nearly identical. Most obviously diverging from the general trend is the large ΔS and accompanying lower ΔG of adsorption to water for the Na_5Cl_4 face discussed in detail in Section 3.6.2.

3.6.1 $Na_4Cl_3^{(+1)}$ Cluster

The Na_4Cl_3 cluster is the smallest cluster to adopt the common cubic structure of the bulk. Deficient a chlorine ion at a corner, the cluster "blooms" outward from the electrostatic repulsion of the three equivalent sodium ions:

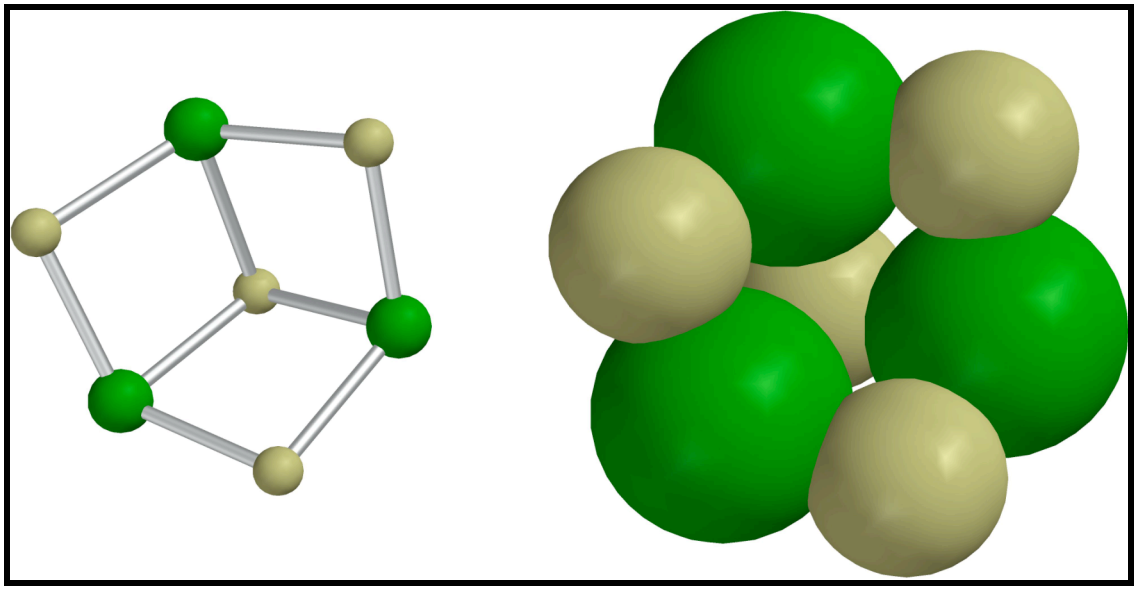

Figure 3.11. Dry Na_4Cl_3 Cation Structure.

The three outward equivalent sodium ions have little steric hindrance and, as seen in Table 3.1, are highly favorable sites for adsorption of water. Experimental data, shown in Figure 3.12, shows multiple water adsorption with computational analysis showing little deformation in structure:

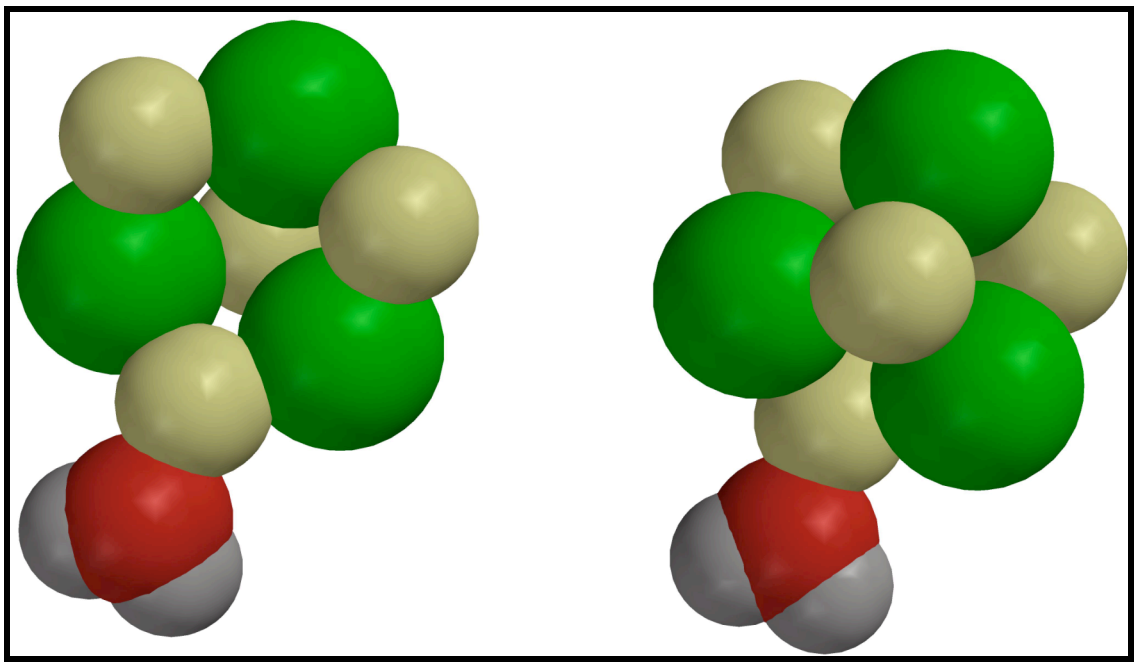

Figure 3.12. Hydrated Na_4Cl_3 Cation Structure – Corner Adsorption.

Clearly shown in Figure 3.12 is the sole coordination of the oxygen from water with a sodium ion. The water molecule shown is able to retain most of its' rotational and vibrational degrees of freedom with minimal coupling to the salt cluster. This type of aggregation is of considerable importance in later discussion where the entropic contribution is considerable.

Adsorption on the back side sodium ion, being coordinated to three chlorine ions as opposed to the aforementioned sodium ion's two, is also found to be thermodynamically favorable, though to a slightly lesser extent. It was found that the water molecule partially tilts. This relatively small interaction with a water hydrogen and cluster chlorine is sufficient to reduce the overall reaction favorability by ~1kcal:

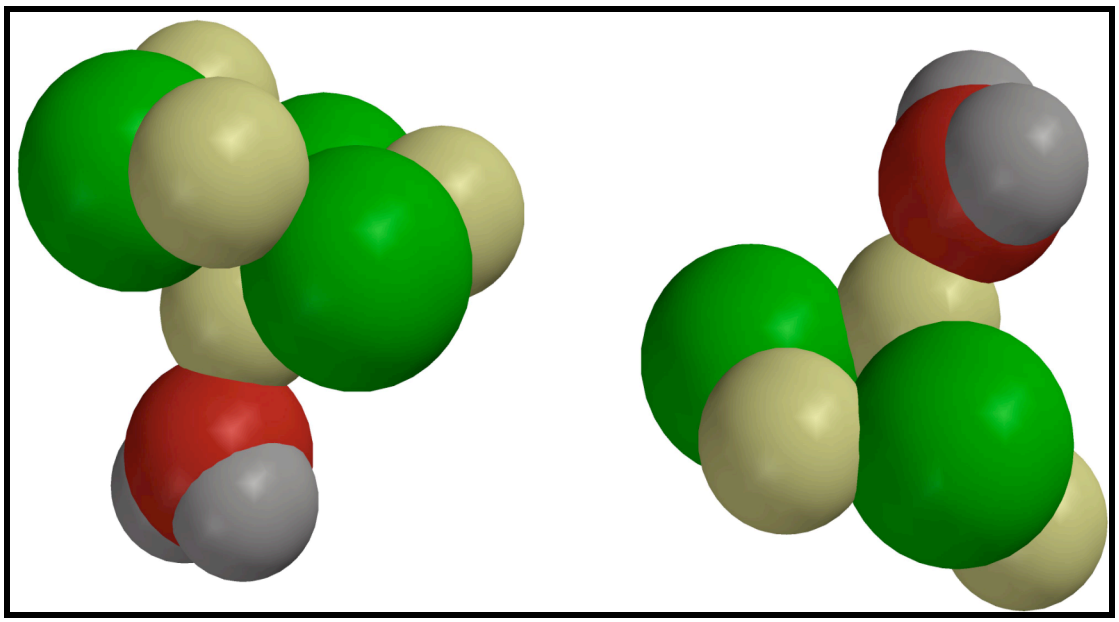

Figure 3.13. Hydrated Na_4Cl_3 Cation Structure – Face Adsorption.

Another significant variation from the corner adsorption is the less favorable dipole-dipole interaction on approach. The side with three equivalent sodium ions is presumed to be the positive side of the cluster dipole, making it the favorable side for interaction with the negative dipole side of the water molecule.

3.6.2 $Na_5Cl_4^{(+1)}$ Cluster

The Na_5Cl_4 cluster is the first in the series to adopt the bulk structure without any ionic defects. Any odd sided cluster, such as 3X1, 3X3, 3X5, and so on, demands the single excess (or deficiency) of either a chlorine or sodium atom. The Na_5Cl_4 cluster is predicted and has been confirmed to be planar in structure with no dipole moment:

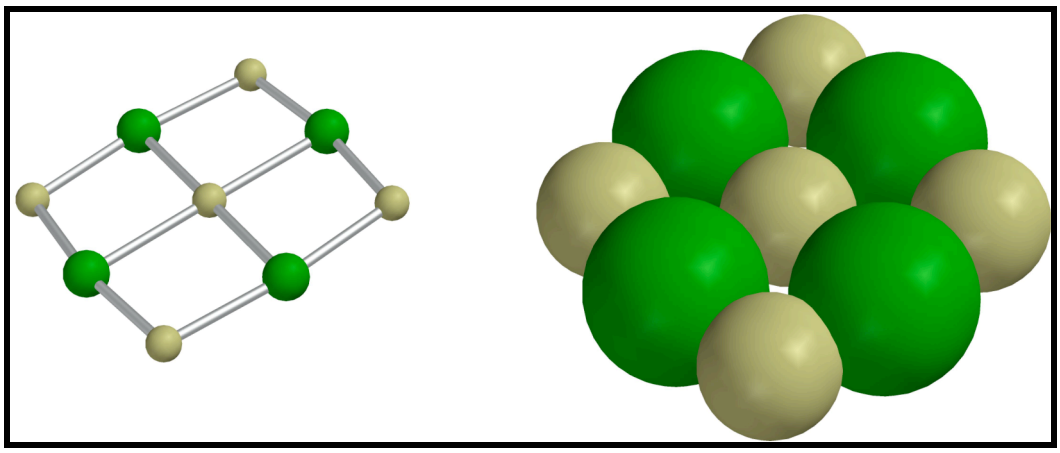

Figure 3.14. Dry Na_5Cl_4 Cation Structure.

Having no dipole, this structure is truly planar, without any warping, and is considered a highly stable species.

Four equivalent outward sodium ions present highly favorable adsorption sites for water. As is the case with the Na_4Cl_3, water adsorbs with a high exothermicity without losing any substantial degree of rotational or vibrational freedom:

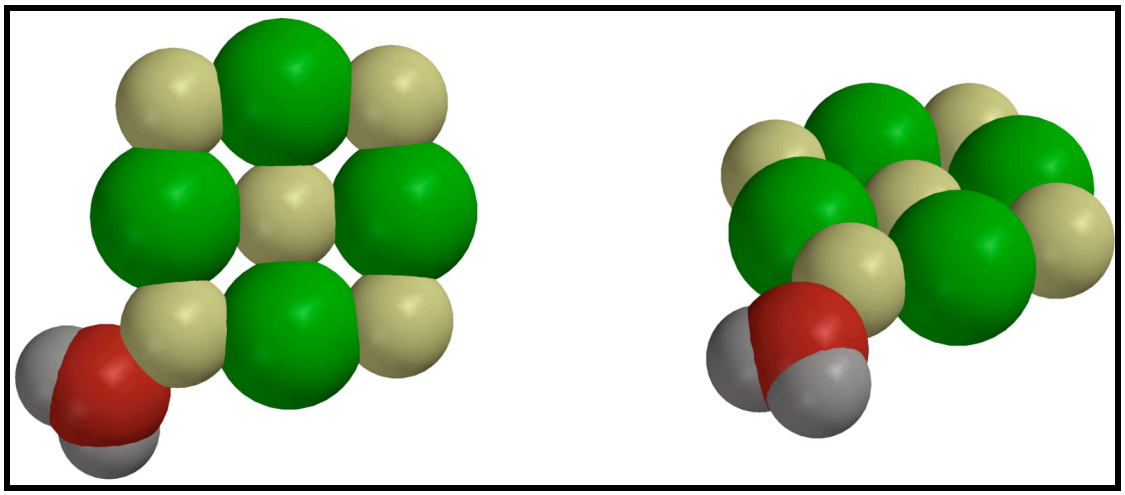

Figure 3.15. Hydrated Na_5Cl_4 Cation Structure – Corner Adsorption.

Additionally, adsorption of water to the Na_5Cl_4 cluster induces no discernable augmentation in structure.

Adsorption to the central face-sodium of the Na_5Cl_4 produces a very different result. As clearly seen in Figure 3.16, water adsorption induces a clear distortion in the previously highly symmetric structure:

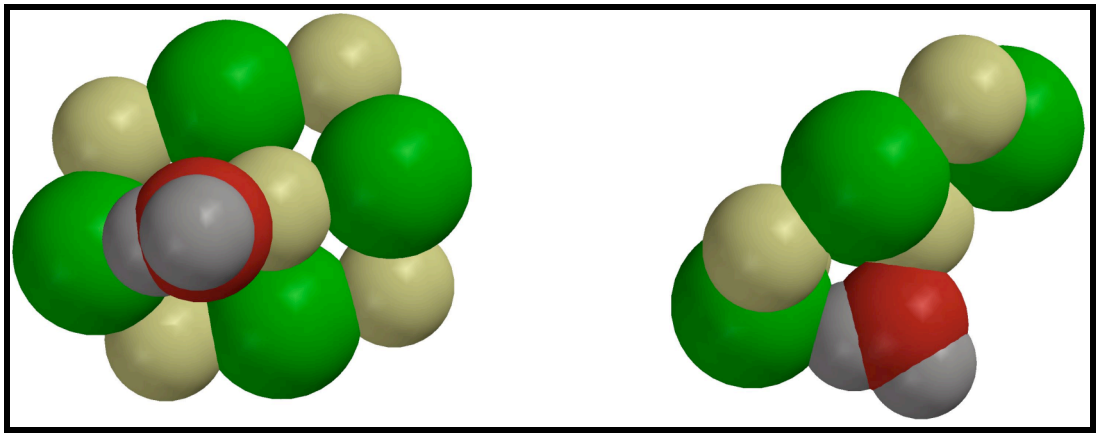

Figure 3.16. Hydrated Na_5Cl_4 Cation Structure – Face Adsorption.

In addition to the structural augmentation, water aggregation here shows a clear coupling of one of the hydrogen atoms from the water molecule to a chlorine ion. This interaction, effectively stripping the water of any rotational freedom as well as partially coupling its' vibrational modes, is a major contributing factor to the much lower predicted adsorption preference predicted and shown in Table 3.1.

3.6.3 $Na_7Cl_6^{(+1)}$ Cluster

The Na_7Cl_6 cluster has innumerous structures in the literature varying by only a few kcal/mol in stability. The most stable of these structures displays an extraordinary atomic arrangement forming an ionic bridge:

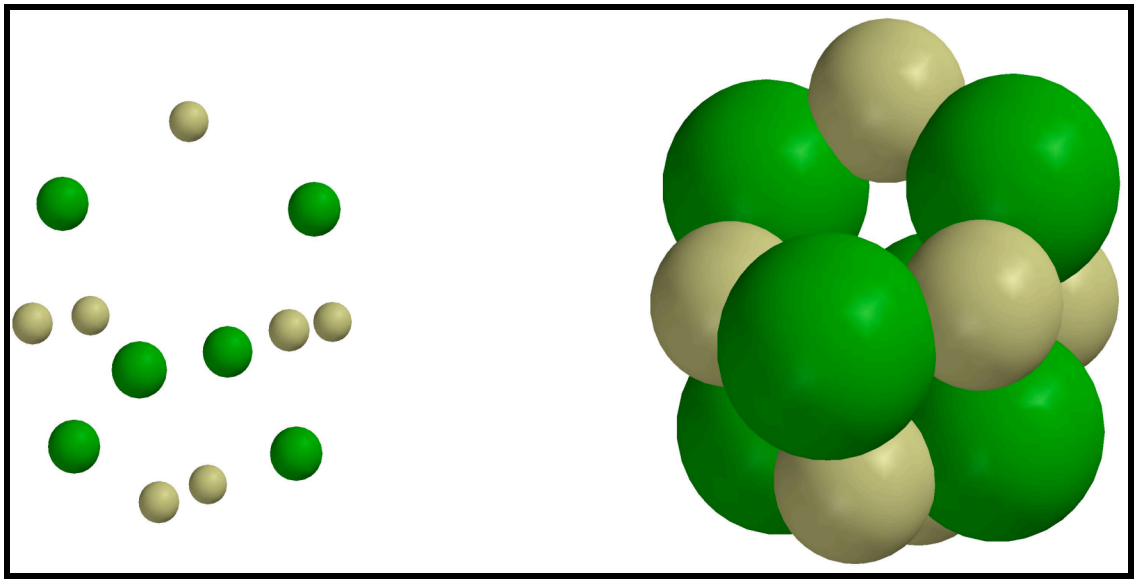

Figure 3.17. Dry Na_7Cl_6 Cation Structure.

Effectively none of the atoms in the Na_7Cl_6 cluster share the simple cubic arrangement found in the bulk. Of equal significance is the fact that every sodium ion is accessible from the surface with significantly less steric hindrance than those found in other species with planar surfaces.

Adsorption to the most accessible sodium ion, on the top of the cluster, is a highly favorable adsorption with, as seen in the Na_4Cl_3 and corner sodiums of the Na_5Cl_4 species, no interaction of the hydrogen atoms from the water:

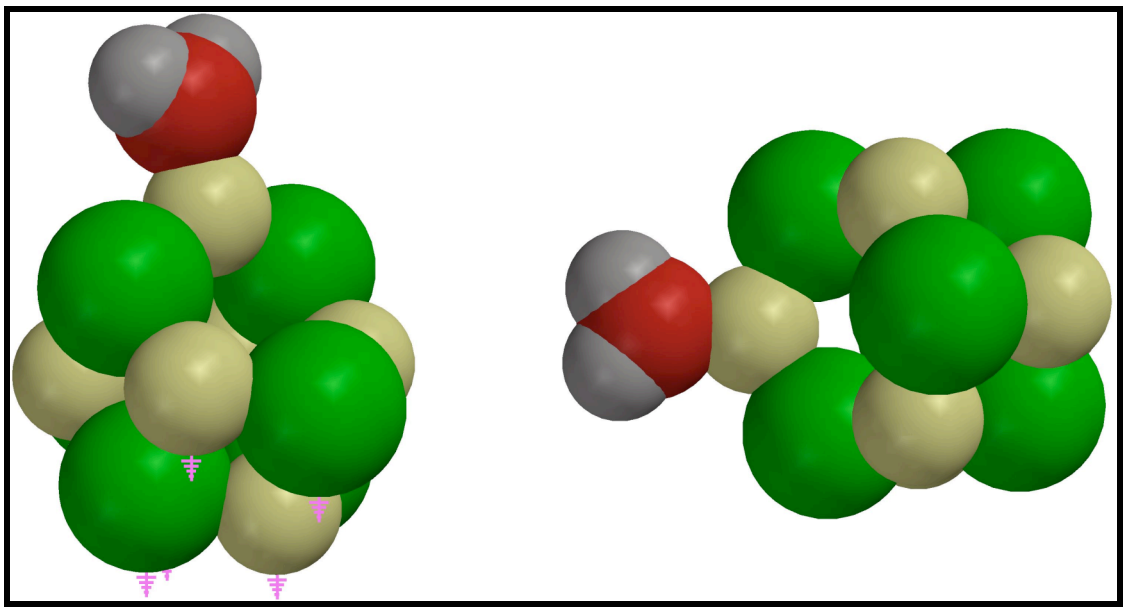

Figure 3.18. Hydrated Na_7Cl_6 Cation Structure – Top Adsorption.

Mass spectral data (Section 3.5.2) confirms this has aggregation ability but also displays multiple adsorptions clearly necessitating other active sites.

The next available site is to one of the four equivalent middle sodium ions. Computational analysis shows this adsorption is more favorable than that of the top sodium ion by ~1kcal/mol:

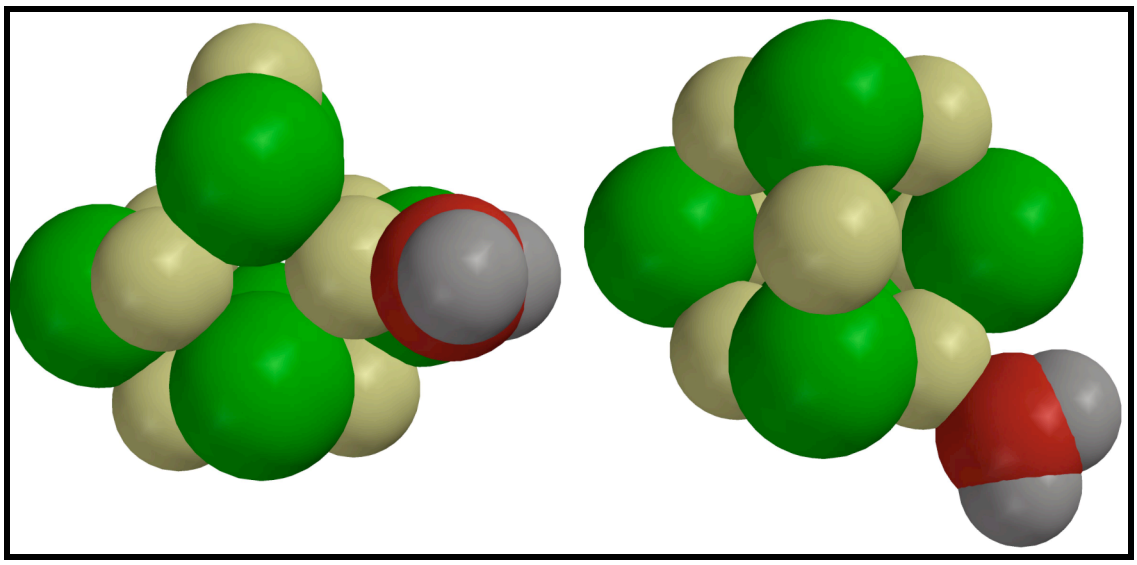

Figure 3.19. Hydrated Na_7Cl_6 Cation Structure – Middle Adsorption.

Because this adsorption site is less favored by the dipole-dipole during approach, an explanation is still needed. Most likely is an electrostatic stabilization from the nearby neighboring chlorine ions.

The last and least energetically favorable adsorption site for the Na_7Cl_6 cluster is to either of the two equivalent bottom sodium ions. Being almost sterically identical to the sodiums in the middle section of the cluster, the ~0.5kcal less favorability is attributed to this part of the cluster being the negative end of its' dipole:

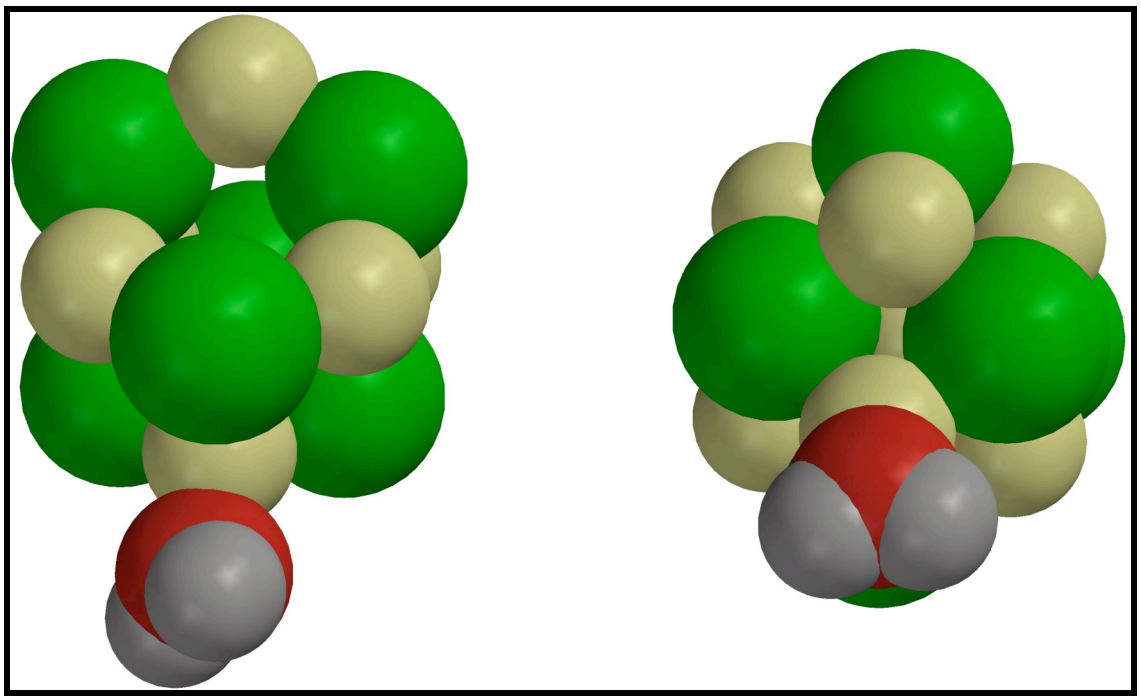

Figure 3.20. Hydrated Na_7Cl_6 Cation Structure – Bottom Adsorption.

Not having the benefit of stabilization from neighboring chlorine ions nor the stronger dipole-dipole interaction found with the sole top sodium ion, this adsorption site is the least favorable, though only by ~1.5kcal/mol.

3.6.4 $Na_{14}Cl_{13}^{(+1)}$ Cluster

The $Na_{14}Cl_{13}$ is the first species visually resembling the bulk structure in all aspects. Like the Na_5Cl_4 cluster, it maintains a charge while having no ionic defects. It has six equivalent cubic faces, zero dipole moment, and is the first in the species studied here to exhibit a relatively low overall charge density. Experimentally the $Na_{14}Cl_{13}$ is observed to be the most stable cluster amongst all of the cationic species studied. Having a net positive charge, the $Na_{14}Cl_{13}$ varies from the bulk only in that the chlorine ions, being much larger that sodium, do not segregate outwards at the surface:[36]

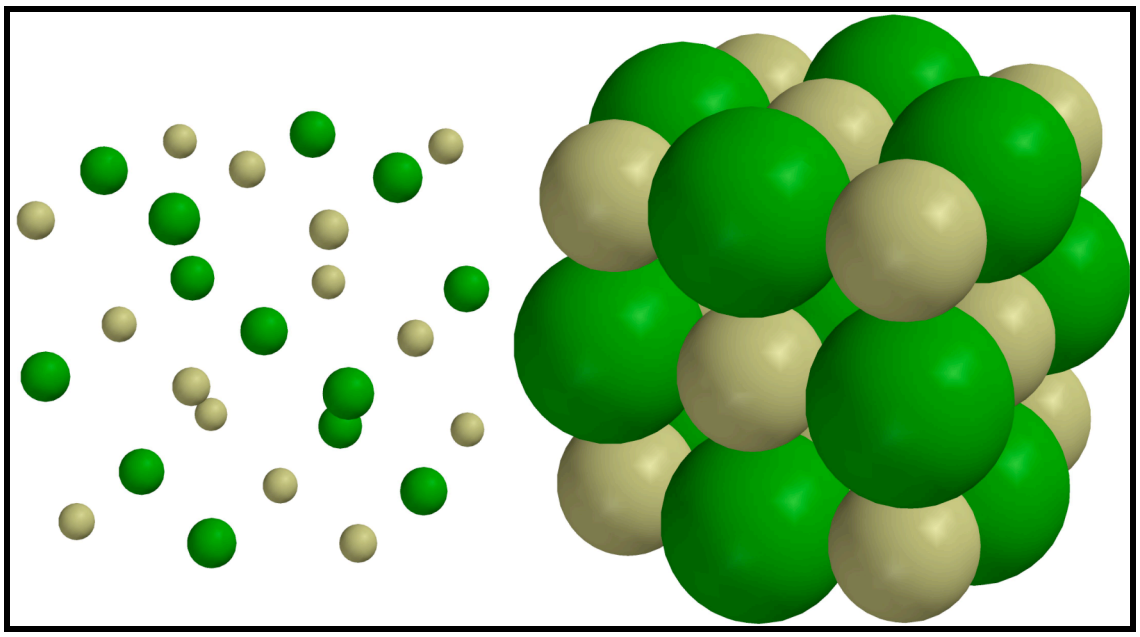

Figure 3.21. Dry $Na_{14}Cl_{13}$ Cation Structure.

Upon reaction with water, the $Na_{14}Cl_{13}$ presumed to adsorb on any one of the eight equivalent outer corner sodium sites:

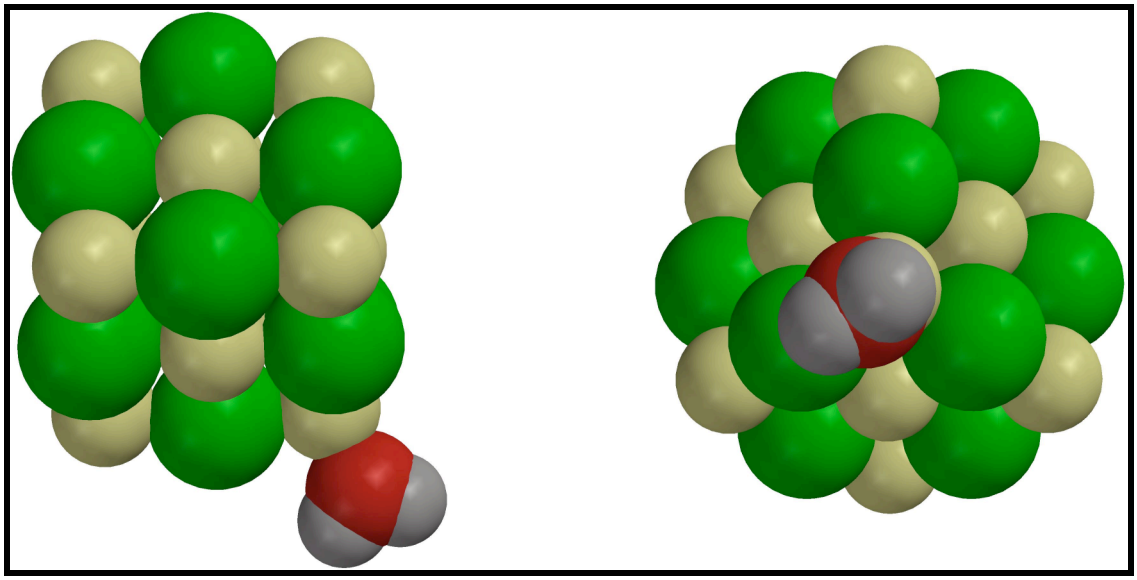

Figure 3.22. Hydrated $Na_{14}Cl_{13}$ Cation Structure – Corner Adsorption.

Results from the Na_4Cl_3 and Na_5Cl_4 clusters imply here that the likelihood for adsorption to any of the 6 equivalent surface sodium atoms would be much less favorable.

3.7 Anion Computational Results

Parallel with the cationic species, computational analysis was undertaken for select anionic species structurally having a marked variation from the bulk structure. All results again represent converged real-solution structures. Agreement is again found with previous studies[34] using lower level calculations. In the case of the anions, bond lengths are found to be overall slightly larger, on the order of 2.3-2.37Å. Although this is a considerable amount when discussing atomic and molecular species, they are still considered realistic and within the expected range. At first glance, the anionic clusters show an overall strong reaction exothermicity with water. Calculated ΔE values are within 1-5kcal/mol of the cation's values and experimentally would be considered quite favorable. Of substantial note and key to this study is the marked difference in ΔS and the dependent ΔG that follows:

Table 3.2. Anion Computational Reaction Values.

Anions					
$Na_nCl_m^{(-1)}$ (n,m)	ΔE (kcal/mol)	ΔH (kcal/mol)	ΔS cal/mol.K	ΔG kcal/mol	BL (angstroms)
(3,4) edge	-19.5	-17.7	-30.2	-8.7	2.35
(4,5) edge	-17.2	-15.4	-29.7	-6.5	2.33
(6,7) High-Energy top	-18.7	-16.8	-30.7	-7.7	2.37
(6,7) High-Energy bottom	-23.2	-21.4	-30.1	-12.4	2.23
(6,7) High-Energy middle	-20.2	-18.3	-32.2	-8.7	2.36
(6,7) Preferred "bottom middle"	-20	-18.4	-26	-10.6	2.32
(6,7) Preferred "bottom out"	-19.8	-18	-29.1	-9.3	2.33
(6,7) Preferred "top ring"	-17.2	-15.6	-28.4	-7.1	2.35
(6,7) Preferred "tope cube"	-18.2	-16.4	-30.2	-7.4	2.28
(13,14) face	N/A	N/A	N/A	N/A	N/A

For anions, the predicted entropic values are as much as 60% greater than found with the cations. In the atmospherically analogues environment, where the environmental temperature is very real and relatively large, the overall entropic contribution to the reaction heavily restricts overall aggregation probability. The anion mass spectrum is consistent with this finding, showing aggregation occurring at a much lesser extent. The cause of this larger entropy value is clearly seen in the predicted adsorption structures that follow.

3.7.1 $Na_3Cl_4^{(-1)}$ Cluster

Nearly indistinguishable from the Na_4Cl_3 cation, the Na_3Cl_4 anion is also the first anion to adopt the approximate simple cubic structure of the bulk:

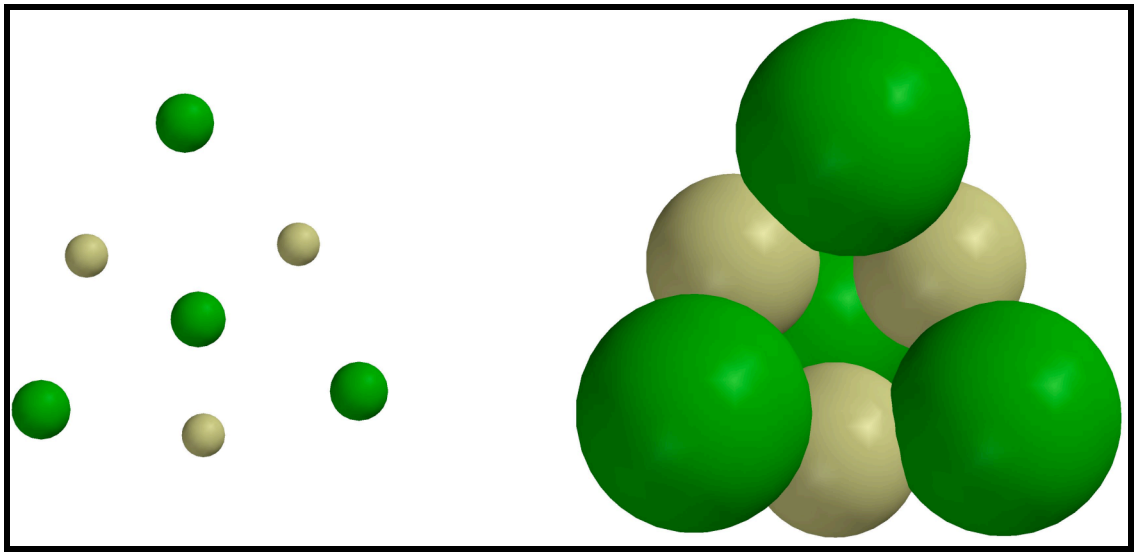

Figure 3.23. Dry Na_3Cl_4 Anion Structure**.**

Similar to its' cationic cousin, the Na_3Cl_4 cluster has three equivalent corner chlorine ions, each coordinated to two sodium ions, and a single face chlorine ions coordinated to all three of the sodium ions present. Also similar is the "blooming" of the defect side due to the electrostatic repulsion of the three equivalent chlorine ions.

As is the case with cation aggregation, the oxygen atom from the water molecule coordinates with a sodium ion in the salt cluster. Close inspection indicates adsorption to the anion is immediately seen as being less likely. In addition to the calculated entropic contribution, the available sodium ions are less abundant and are sterically hindered by the chlorine ions, which have a tendency to segregate outwards[36] due to their size and

electrostatic repulsion from one another in neutral and anionic clusters. Adsorption on the side of the three equivalent chlorines shows clear interaction with both hydrogen atoms, significantly reducing any rotational or vibrational freedom available to the water molecule:

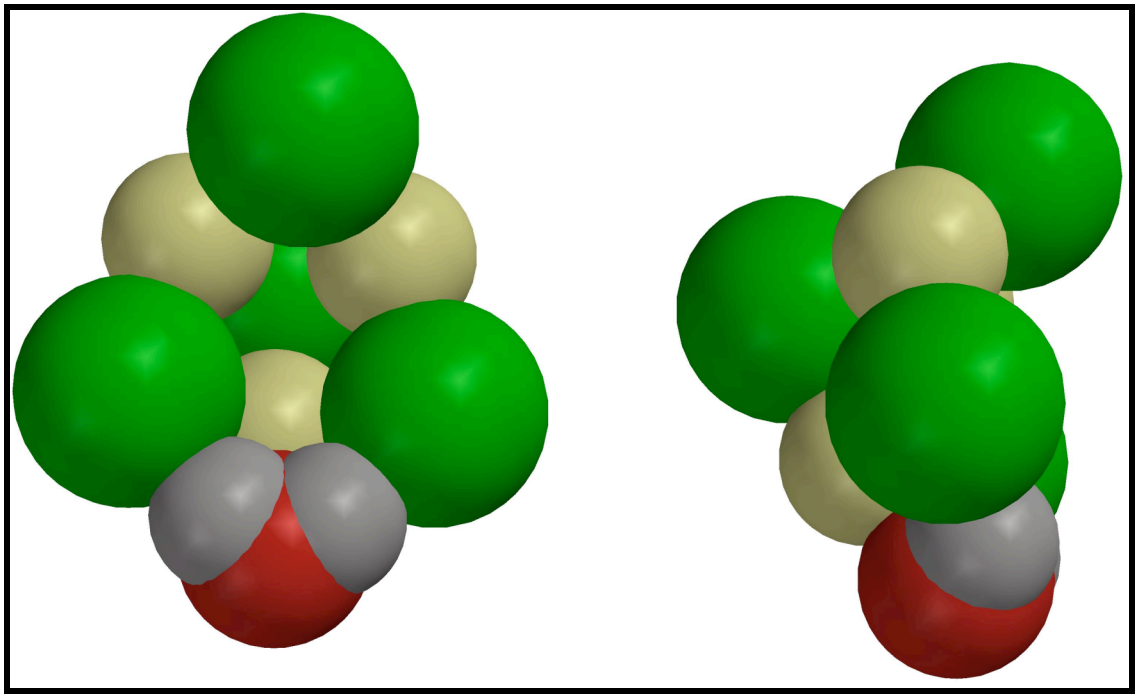

Figure 3.24. Hydrated Na_3Cl_4 Anion Structure – Corner Adsorption.

Though no appreciable distortion in structure is induced, this adsorption is further hindered by the lack of a favorable dipole-dipole interaction between the water molecule and cluster during approach. Not until contact occurs can the oxygen from the water rotate around to properly coordinate with an available sodium ion. Adsorption to the opposite side, with the non-equivalent chlorine ion, is presumed to have the same coordination and unfavorable entropic restriction.

3.7.2 $Na_4Cl_5^{(-1)}$ Cluster

Because of the larger size of the chlorine ion relative to sodium, the Na_4Cl_5 clusters does not adopt the same planar structure as its' cation equivalent**.** The Na_4Cl_5 configuration presents a clear central deformation, taking on a more cup-like or watch-glass arrangement:

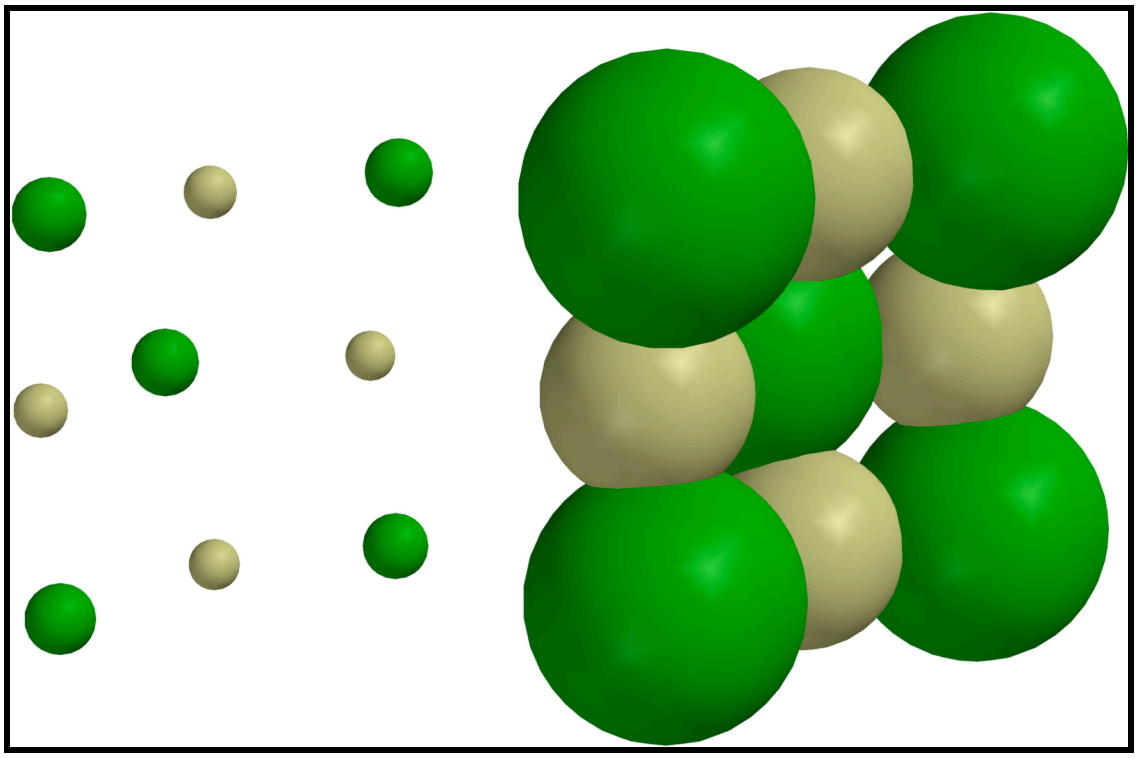

Figure 3.25. Dry Na_4Cl_5 Anion Structure.

As with the Na_4Cl_5, the four equivalent sodium ions here are surrounded by the larger chlorine ions. In the anionic case they, however, are not readily available for coordination with the water molecule's oxygen atom.

Upon adsorption of a water molecule, the interaction of both hydrogen atoms is again seen as the adsorbent is forced to effectively lay-down on the salt surface:

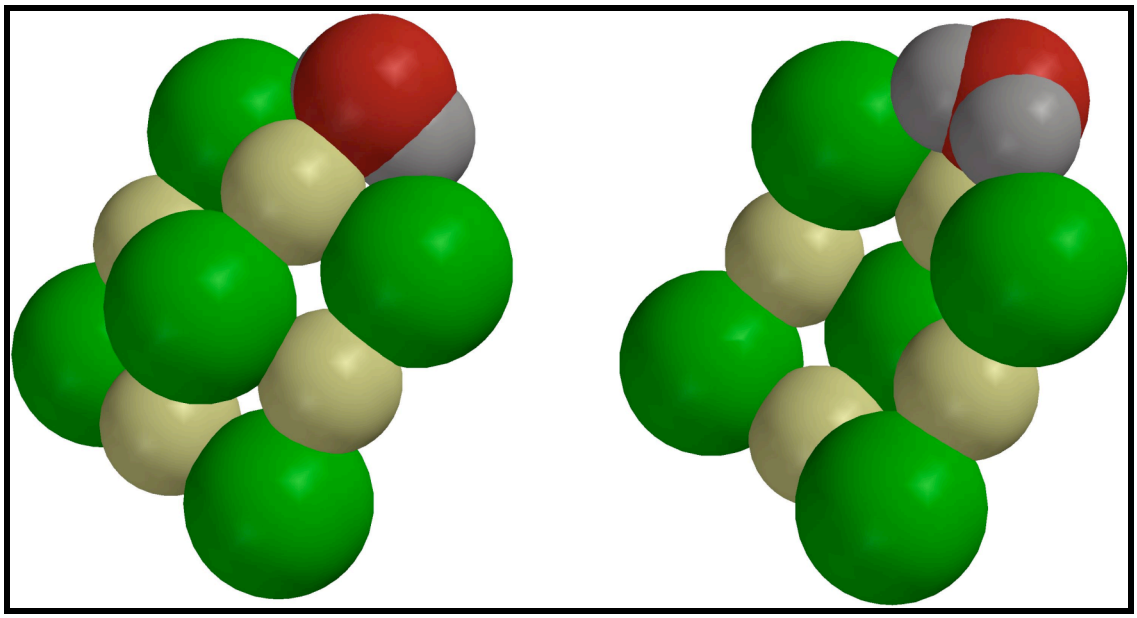

Figure 3.26. Hydrated Na_4Cl_5 Anion Structure – Edge Adsorption.

No further distortion in structure is seen but based on the computational analysis undertaken, this presents a much less favorable adsorption than the cation equivalent.

3.7.3 $Na_6Cl_7^{(-1)}$ Clusters

The Na_6Cl_7 cluster presents a number of spectacular exceptions to the rule for the anionic species. Two separate Na_6Cl_7 structures were investigated. The first, here labeled "preferred", is confirmed[34] as the most stable dry species structure. The oddly shaped species appears, qualitatively, as a pseudo-hybrid of the Na_3Cl_4 and Na_4Cl_5 clusters having a nine atom deformed plane with a four atom deformed plane added to a corner:

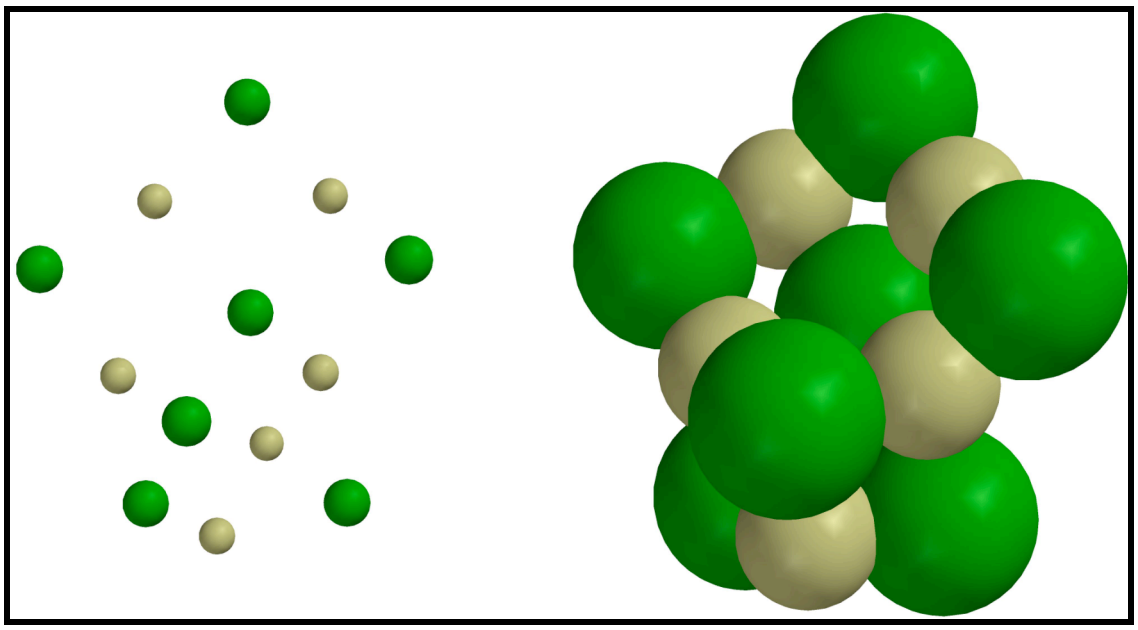

Figure 3.27. Dry Na_6Cl_7 Anion Preferred Structure.

Whereas the Na_4Cl_5 is similar to its' cation counterpart, albeit with a deformation, the preferred Na_6Cl_7 species is the only cluster studied here that has nothing, structurally or qualitatively, in common with its' analogous cation. There are four non-equivalent adsorption sites for the preferred Na_6Cl_7. The first, referred to as the "top cube" site occurs having the water molecule effectively connecting a chlorine ion from the 3X3 plane to a chlorine ion from the 2X2 plane. Oxygen from the water molecule coordinates to one of the sodium ions in the upper 3X3 plane thereby having, as seen with many of the other anions, all three constituent atoms from the water ionically coupled to the cluster:

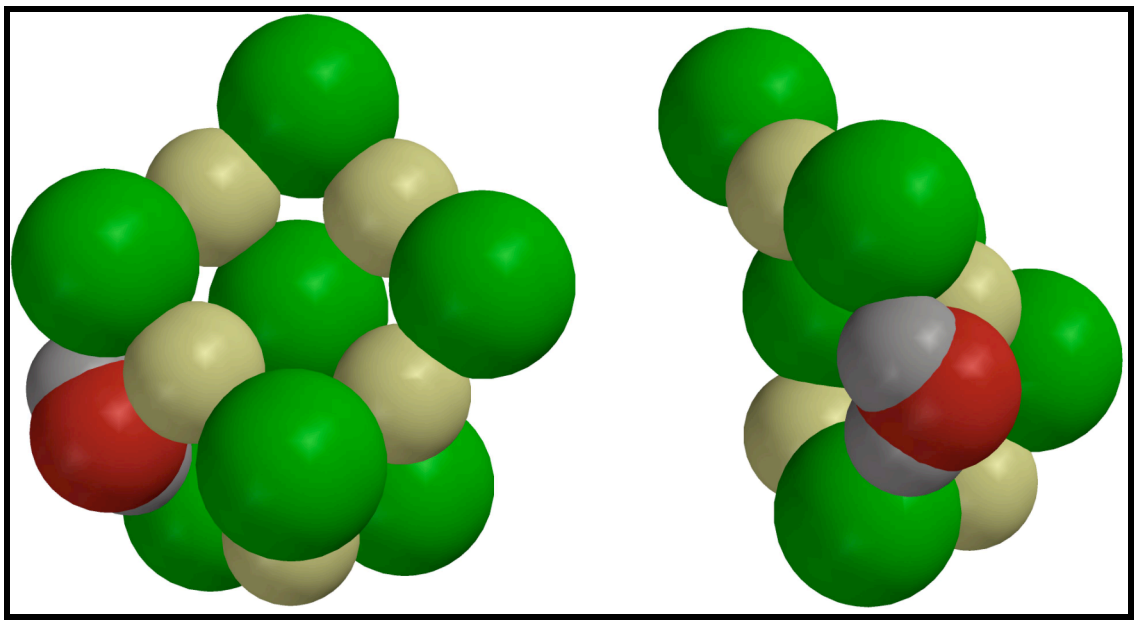

Figure 3.28. Hydrated Na_6Cl_7 Anion Preferred Structure – Top Cube Adsorption.

The entropic contribution, as shown in Table 3.2, is considerable, having the highest entropy term and second least favorable free-energy of reaction of the four adsorption sites available to the preferred Na_6Cl_7 species.

The second adsorption site available for the preferred Na_6Cl_7 is here called the "top ring" site. Though not having the largest entropy term, the top ring site is the least energetically favorable site in the series. Here the water oxygen coordinates to a sodium ion in the upper 3X3 plane. Only one of the hydrogen atoms couples, also in the upper 3X3 plane to the neighboring chlorine:

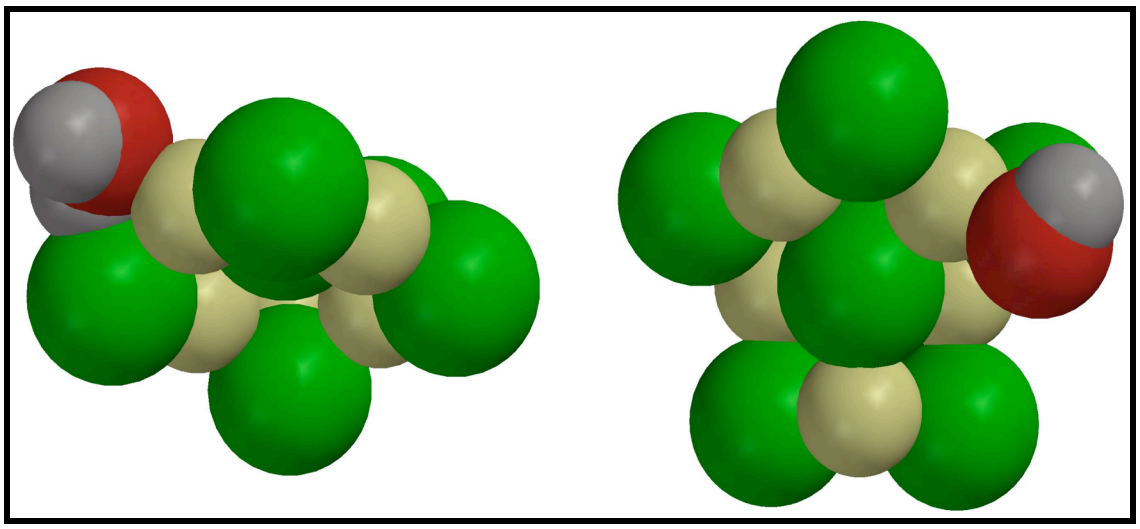

Figure 3.29. Hydrated Na_6Cl_7 Anion Preferred Structure – Top Ring Adsorption.

As with the other anions studied thus far, no discernable distortion in structure is observed from aggregation. Because of the low reaction energy however, this adsorbent arrangement is not likely to have any significant population.

The most favorable adsorption site for the preferred Na_6Cl_7 cluster is the "bottom middle" site. Having the smallest entropic hindrance and largest reaction free-energy, the bottom middle configuration, like the top ring, coordinates only one of the water hydrogen atoms. Here the oxygen coordinates to the inside sodium from the lower 2X2 plane, arguably the least sterically guarded by the surrounding chlorine ions, and coordinates the single hydrogen to a chlorine in the same plane:

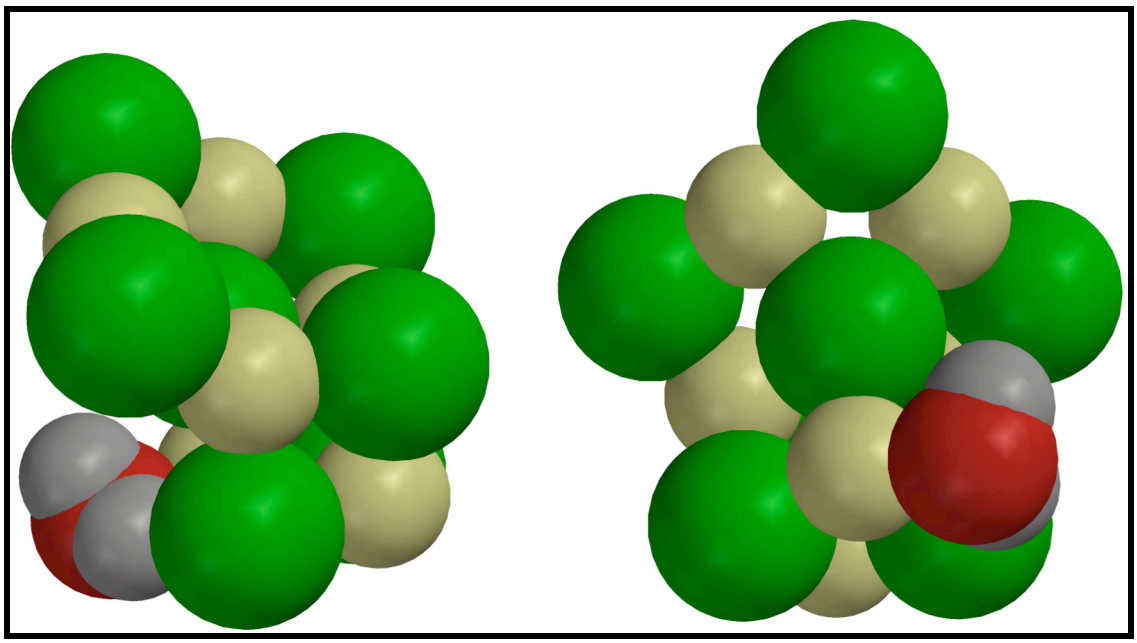

Figure 3.30. Hydrated Na_6Cl_7 Anion Preferred Structure – Bottom Middle Adsorption.

Having a reaction exothermicity nearing that of the cations, this adsorption site is helped, in part, by the fact that the lower 2X2 plane of the preferred Na_6Cl_7 is the presumed positive side of the dipole. Whether this dipole-dipole interaction can locally overcome the dipole-ion interaction arising from the clusters overall negative charge is not clear, though it certainly can't retard the process during approach.

The last of the four available adsorption sites for the preferred Na_6Cl_7 cluster is here labeled the "bottom out". As in the case of the "top cube" aggregation site, the "bottom out" configuration coordinates the oxygen and both hydrogen atoms from the water molecule. The arrangement is analogous to that of the "top cube" assignment as the water molecule effectively bridges the upper 3X3 and lower 2X2 planes. Following a 90^0 rotation, this arrangement allows the oxygen atom to coordinate with the outer sodium from the lower 2X2 instead of the upper 3X3 plane:

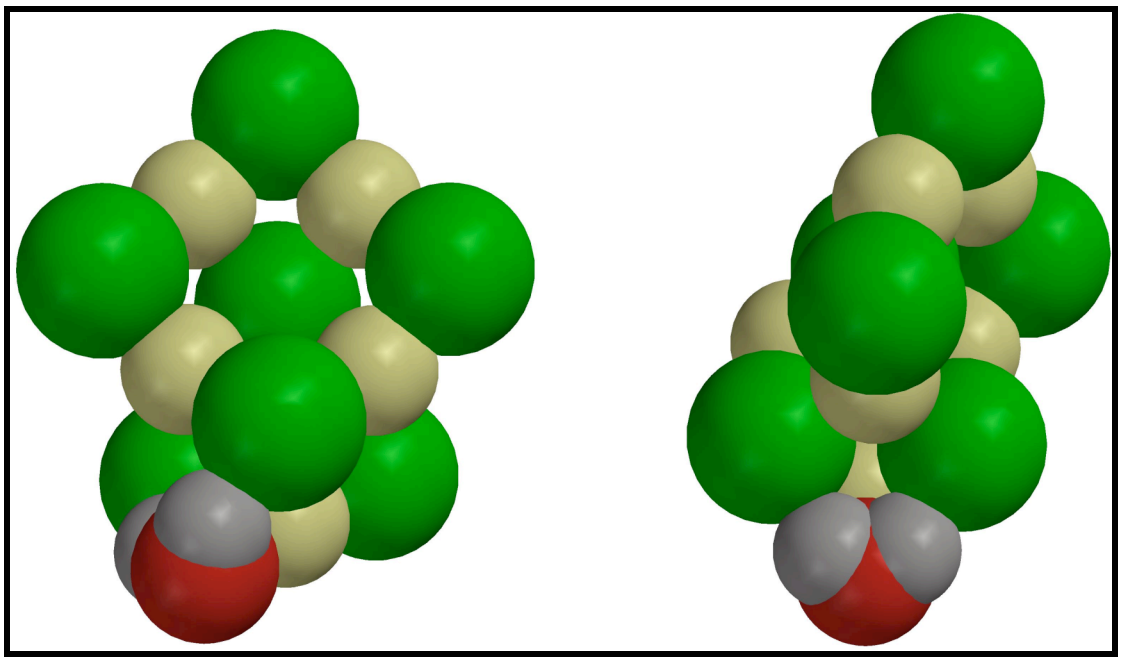

Figure 3.31. Hydrated Na_6Cl_7 Anion Preferred Structure – Bottom Out.

While still having a considerable entropic hindrance to adsorption, the overall free-energy of reaction is second only to the "bottom middle" with the energetic difference being only slightly larger than 1kcal/mol.

The second structure investigated, being only ~1kcal/mol higher in energy than the preferred structure, is analogous to the cationic Na_7Cl_6. With the sodium and chlorine ions interchanged, the overall structure is still exceptionally stable. Sharing the bridged ion of the Na_6Cl_7, a chlorine ion, coordinated to only two sodium ions, protrudes from the top of the cluster. The other chlorines in the Na_6Cl_7 heavily guard the inclusive sodium ions:

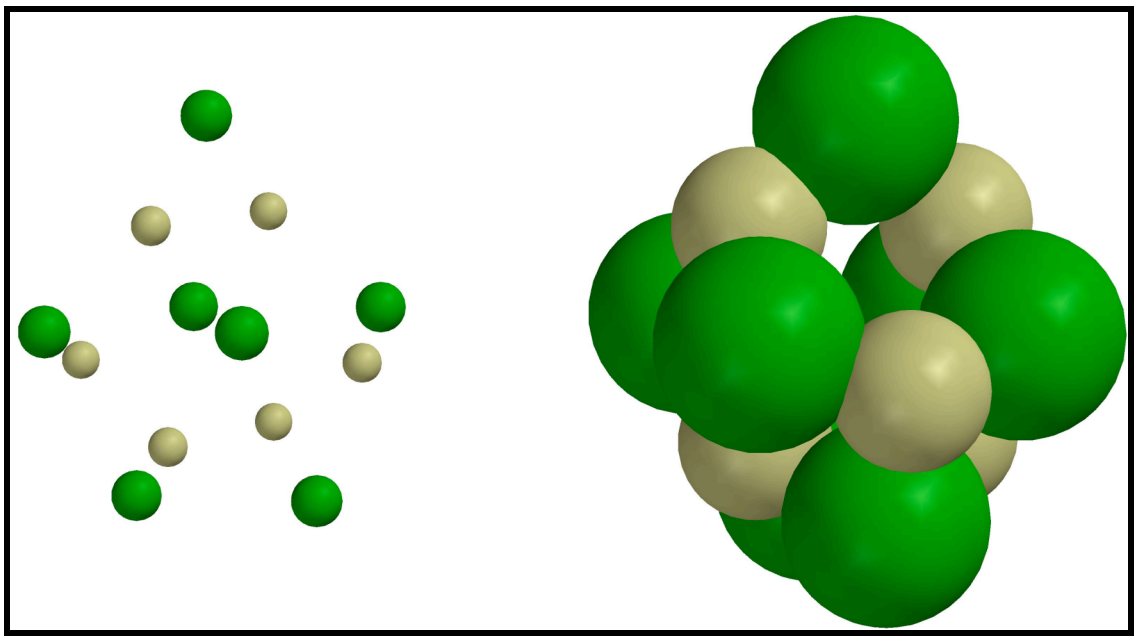

Figure 3.32. Dry Na_6Cl_7 Anion High-Energy Structure.

Approaching from above, the first available adsorption sites does not allow for coordination to the bridged chlorine ion. Instead, the water molecule couples with two of the chlorine ions in the middle chlorine plane and the sodium ion in between them:

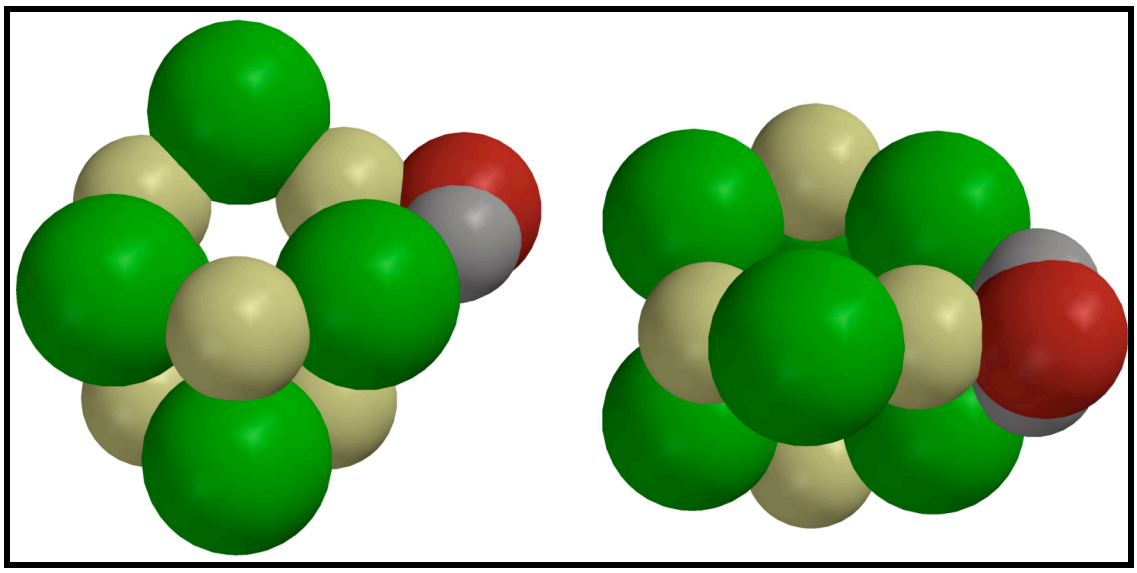

Figure 3.33. Hydrated Na_6Cl_7 Anion High-Energy Structure – Top Adsorption.

No discernable distortion occurs in the cluster from aggregation but, as shown in Table 3.2, this particular configuration is highly unfavorable. For the higher energy Na_6Cl_7, it has the second largest entropic contribution, the lowest free-energy of reaction, and one of the lowest free energies of reaction of all of the anion species studied here.

The middle adsorption site for the high-energy Na_6Cl_7 configuration approaches from the middle of the cluster. The oxygen coordinates to the same sodium ion as in the previous case but one of the two hydrogens coordinates to a chlorine ion in the lower chlorine plane:

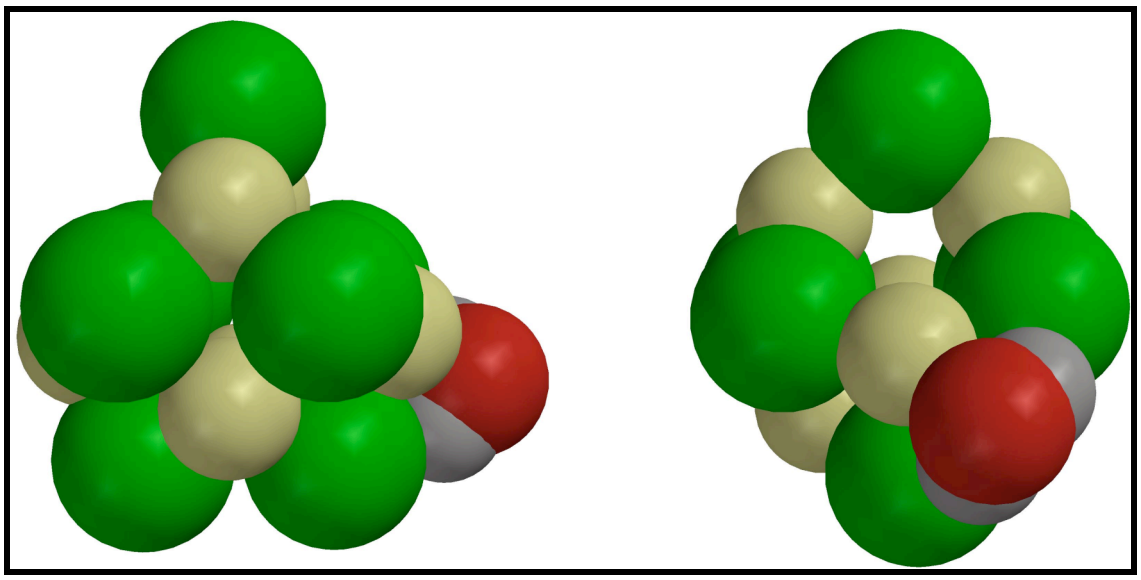

Figure 3.34. Hydrated Na_6Cl_7 Anion High-Energy Structure – Middle Adsorption.

This arrangement has the highest entropic contribution of the high-energy Na_6Cl_7 adsorption sites but still manages an overall reaction free-energy near that of the "bottom-out" adsorption site seen for the preferred Na_6Cl_7 structure.

The final available adsorption site for the high-energy Na_6Cl_7 demands a detailed discussion. With the exception of the adsorption of water to the face of the Na_5Cl_4 cation, no other adsorption presented thus far has induced any considerable distortion in structure. Approaching from the bottom of the cluster, when water adsorbs to the high-energy Na_6Cl_7 cluster, a rearrangement of the entire cluster structure occurs:

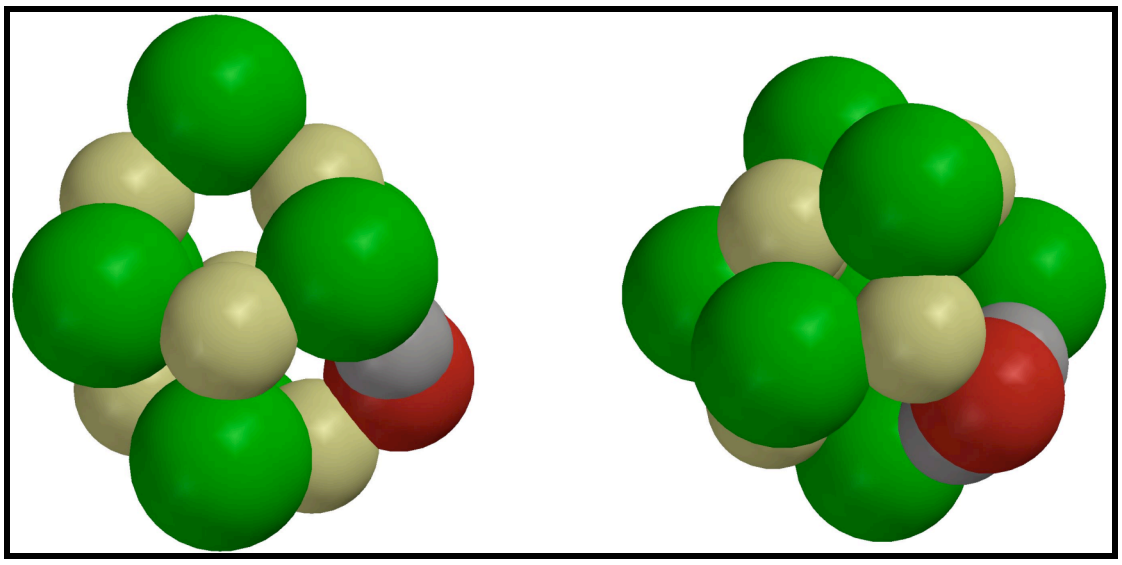

Figure 3.35. Hydrated Na_6Cl_7 Anion High-Energy Structure – Bottom Adsorption.

The entire lower plane of the high-energy Na_6Cl_7 is shifted, integrating the water molecular in place of two previously present ionic bonds. The water molecule, acting as an intermediate bridge, displaces one of the lower plane surface sodium ions and, through strong hydrogen bonds, connects to two of the middle plane chlorine ions. The shift of the four lower atoms effectively induces the clusters to adopt a local CsI, of BCC, structure. In addition to inducing an enormous distortion and rearrangement in the initial Na_6Cl_7 structure, computational analysis shows this adsorption provides a record high anionic reaction free-energy; comparable in strength to that found in cation aggregation.

3.7.4 $Na_{13}Cl_{14}^{(-1)}$ Cluster

The $Na_{14}Cl_{13}$, like its' cationic equivalent, is the first anionic species visually resembling the bulk structure in all aspects. Like the Na_4Cl_5 cluster, it maintains a charge while having no ionic defects. It also has six equivalent cubic faces, zero dipole moment,

and is the first in the species studied here to tend to a relatively low overall charge density:

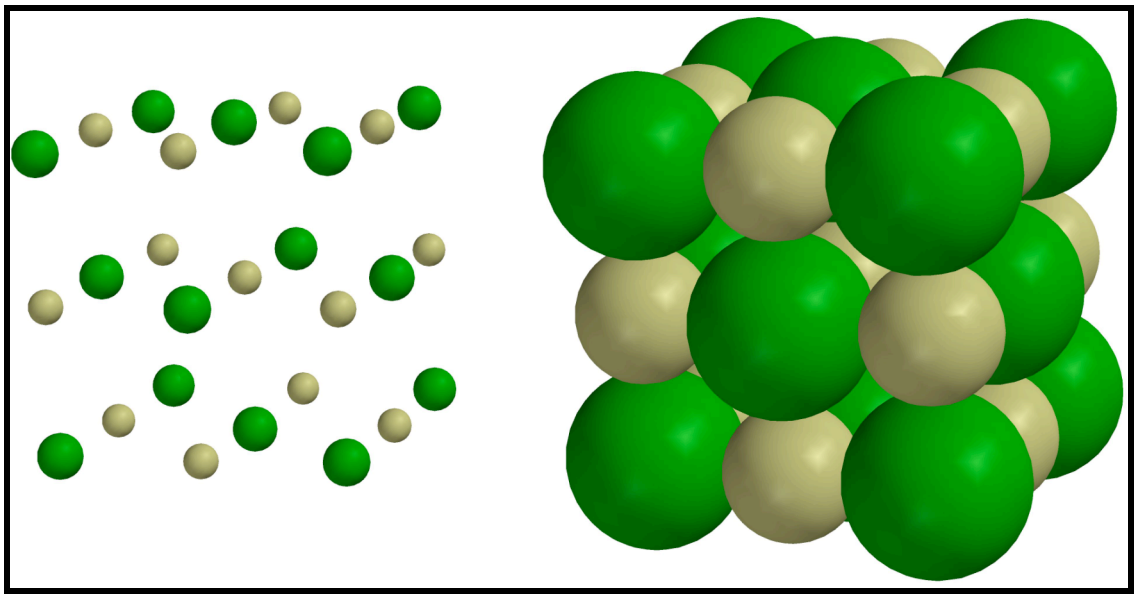

Figure 3.36. Dry $Na_{13}Cl_{14}$ Anion Structure.

Adsorption was not observed in experiments but adsorption to this species is most likely analogous to adsorption on a bulk 001 face,[28,29] where, as has been seen with a number of other anions, the water molecule coordinates its oxygen as well as both of its' hydrogens.

3.8 Discussion

Of all of the significant observations presented, the predicted effect of water adsorption on the high-energy Na_6Cl_7 anion is certainly the most profound. Although, as mentioned previously, this pre-aggregate structure is not the most stable structure available, it is likely produced by the LDI reactor source. Being highly favorable and stable as an aggregate, the presence of water during cluster formation in the reactor likely

induces a viable number of this type of coordination cluster to form. This adsorption favorability is comparable to that of the cations and, by inducing a considerable augmentation of its' structure, is seen in the experimental adsorption mass spectrum as the first relatively abundant adsorption yield species. This adsorption is only seen for water approaching from the bottom of the cluster and, inducing a BCC-like coordination of the sodium and chlorine ions, is markedly different than any other anionic $NaCl:H_2O$ aggregate structures known. Computational modeling also indicates that the most stable pre-aggregate (preferred) Na_6Cl_7 structure adsorbs water with a Gibbs free-energy far exceeding the other anionic clusters pursued here, though not quite to the same extent as observed for the cations.

Similar to adsorption on a 001 neutral bulk surface,[28,29] other anionic aggregates require the water molecule to lay effectively flat on the surface. Coordination of the oxygen to sodium as well as one or both of the hydrogen's to chlorine is predicted and experimentally confirmed to be entropically unfavorable. Once adsorbed, the water molecule effectively loses all rotational degrees of freedom as well as coupling multiple vibrational modes by way of the hydrogen-chlorine interaction. Further hindering this aggregation is the lack of an appreciable long-range interaction to initiate approach with an appropriate orientation. The dipole-dipole/dipole-ion forces for the anionic species require that the water approach hydrogen-side first, impeding the necessary and dominant oxygen-sodium interaction.

Adsorption to cation cluster surfaces falls in suit with the anionic system as they are also predicted and observed here to be much less favorable. As seen in the adsorption of water to the center sodium ion in Na_5Cl_4, computational analysis shows promotion of a

considerable augmentation in the planar cluster structure. This augmentation, unlike the spectacular high-energy Na_6Cl_7, proves to be both energetically and entropically unfavorable and highly unlikely relative to other adsorption configurations.

Since calculations indicate that most cationic species have similar reaction exothermicity or ΔE, steric hindrance and relative charge density also play a key role in promoting adsorption. High defect density species such as Na_4Cl_3, Na_6Cl_5, Na_7Cl_6, and $Na_{13}Cl_{12}$ are capable of adsorbing multiple waters molecules with little or no effect to their structure or stability. Species with highly exposed sodium ions, such as the planar Na_5Cl_4 and oddly shaped Na_7Cl_6, are also capable of readily interacting with the oxygen side of water, presenting a preferential adsorption site. As one tends to the bulk, reducing both charge and defect density, a rapid drop-off in adsorption probability is observed.

The $Na_{14}Cl_{13}$ cluster exhibits a much lower experimentally observed adsorption yield then its' brethren Na_5Cl_4. Although both species have no dipole moment, the Na_5Cl_4 presents a higher relative charge density and has considerably less chlorine crowding around the available corner sodium ions.

Clearly seen are a number of marked differences in the kinetics and coordinations involved in the adsorption of water to anion and cation clusters. For both, but much more so for the cations, the structural variations available give rise to differing charge densities and inherent dipoles, both of which are of significant during pre-aggregation approach. Unfavorable dipole-dipole and dipole-ion interactions have been shown to cause some adsorption sites to aggregate poorly. More significant to the anions, with the exception of adsorption to the facial sodium in Na_5Cl_4, is the significant entropic contribution arising from the coordination of one or both hydrogens from the water molecule. This

conformation, necessary to all anion aggregates, stifles the rotational and vibrational degrees-of-freedom of the water to such an extent that adsorption at any atmospherically accessible temperature will compete poorly relative to cationic species.

CHAPTER 4

WATER SOLUBLE AUROUS BENZENE-THIOLATE OLIGOMERS

4.1 Introduction and Background

Aurous-thiolate [Au(I)(SR)] compounds are crucial agents in a number of areas of chemistry and materials science. They are the established precursor[37] for adherent gold-film formation commonly found in use as heat reflectors in jet engines, engine compartment heat reflectors for various competitive performance motorsports, microelectronics, and various decorative uses. Aurous-thiolates have also long been used as chrysotherapy[37] agents for treatment of rheumatoid arthritis. The more recent use as a direct precursor in most gold cluster/nanoparticle/colloid preparations used nowadays has become preferential, also being products of the etching-decomposition products of the same and of gold-thiolate self-assembled monolayers (SAMs).

This long-established reputation for practical importance is matched, unfortunately, by a reputation for fundamental intractability. They exist mainly as highly stable polymeric substances, with the chain structure $(—Au—SR—)_x$, involving linear coordination about the Au(I) center to the two proton-free S-atoms. The free AuSR molecules are essentially unknown, and the solubility is very low (~1 mM) except under conditions of excess thiolate and high pH. A classic example is the Au(I)CyS compound of the amino-acid thiol cysteine (CySH), with a solubility of ~1mM at pH = 7.4, requiring a 25-fold excess of CySH to achieve a solubility of 100 mM, in the form of $Au(CyS)_2^{(-1)}$ complexes.[38]

In practice, this has implied the substantial disadvantages of having to work with insoluble phases present, or at very low concentrations, or using strong complexing agents (Lewis Bases such as Ph_3P:), or employing sterically demanding (tertiary) thiolates that preclude the formation of long-chain polymers.

The para-mercaptobenzoic acids (pMBA = HOOC-C_6H_4-SH) appear to constitute a striking exception. Despite this group's experiences with the various gold-benzenethiolates, we were not aware of this aspect until the recent reports of Ackerson, Jadzinsky, Azubel et al., who have used Au-pMBAs to obtain high quality Au-rich clusters from reactions in a single (aqueous) phase.[39] The total-structure-determination of a $(Au)_{102}(pMBA)_{44}$ compound suggests that short oligomeric units, such as the $Au(pMBA)_2^{-1}$ species, are key structural units stabilizing this giant cluster.

Lacking in the recent literature however is a thorough investigation of the Au(pMBA) oligomer prior to reduction for cluster formation. This water soluble precursor is thought to have a wide variety of other chemical applications, beyond that previously presented, and would likely be more efficiently and calculably applied with a better understanding of its' fundamental physical properties. It follows that a basic analytical study be undertaken.

4.2 Synthesis

4.2.1 Standard Synthesis

Initially, the synthesis technique described in the existing literature[40] was replicated. 10 mM oligomer solutions were prepared in 50:50 methanol-water. A solution

containing 4 molar equivalents of pMBA was added to a solution of dissolved $HAuCl_4$, inducing the formation of the Au(I)pMBA oligomer:

$$Au(III)Cl_{4\,(aq)}^{-1} + 4HSC_6H_4COOH_{(aq)} \rightarrow$$
$$Au(I)_n(SC_6H_4COOH)_{m(s)}^{-1} + HOOC - H_4C_6S - SC_6H_4COOH_{(aq)} \quad \textbf{(4.1)}$$

Due to the low pH of the reactant solution (pH ~2) from the high acidity of the tetrachloroaurate ($AuCl_4^{-1}$), the aurous-thiolate oligomer immediately precipitated as a white polymeric substance. The solid oligomer was centrifuged in solution, rinsed multiple times with water to remove any excess disulfide, presumed to be soluble, and then introduced into pure de-ionized water. 1M NaOH was added to a pH > 9 to expedite solubilization, then back titrated with 1M HCl to neutral pH (7). Further addition of HCl to 10mM oligomer solution would induce precipitation of the oligomer below ~pH 6.5.

4.2.2 Soluble Synthesis

It was proposed and confirmed that an alternative synthesis pathway was also available which did not induce any precipitation upon oligomer formation. Prior to mixing, the separate pMBA and tetrachloroaurate solutions were each pH adjusted using 1M NaOH. The pMBA solution had ~2 molar equivalents added to a pH of ~7 to fully deprotonate the carboxylic protons:

$$HSC_6H_4COOH + NaOH \rightarrow HSC_6H_4COO^{(-1)} \quad \textbf{(4.2)}$$

The tetrachloroaurate solution was adjusted to ~pH 4. Any additional NaOH would induce the tetrachloroaurate to decompose to colloidal gold. The pH-adjusted solutions were then mixed, adding the tetrachloroaurate solution drop-wise to the pMBA solution:

$$Au(III)Cl_{4\,(aq)}^{-1} + HSC_7O_2H_{(aq)} \rightarrow$$
$$Au(I)(SC_7H_4O_2H)_{2\,(aq)}^{-1} + HO_2H_4C_7S - SC_7H_4O_2H_{(aq)} \qquad \textbf{(4.3)}$$

Having been pH-adjusted this time prior to reaction, no oligomer precipitate formed. This synthesis seemed advantageous, though whether or not the product was as predicted, the same as the standard synthesis, necessitated further investigation.

4.3 ESI-MS Analysis

10 mM oligomer solutions from both synthesis techniques were prepared for electrospray ionization (ESI)-MS analysis. The standard synthesis solution, not being rinsed so as to fully characterize all solvated species, was solubilized in 50:50 solution at a pH >9 and then diluted (with 50:50 solution) to a concentration of 10 μM. The soluble synthesis solution was also diluted to 10 μM with 50:50 solution. Compositional analysis of the solution was performed using a Thermo Finnigan LCQ DecaXP+ ion-trap mass-spectrometer (Thermo Fisher Scientific, Inc. Waltham, MA) fitted with an ESI ion source and configured to detect negatively charged ions (no discernable signal was found for positive ions nor was any expected). Optimized single parameters utilized an ion-transfer capillary temperature of 300^0C. It is significant to note that at lower capillary

temperatures, as low as 200^0C, compositional distribution of molecular species remained identical while suffering only in signal strength; one of the many indications of the exceptional stability of the $Au(pMBA)_2^{(-1)}$ oligomer and higher homologs.

4.3.1 Linear Oligomers

The acquired mass spectrum shows a majority content of the $Au(pMBA)_2^{(-1)}$ followed by lesser quantities of the larger oligomers $Au_2(pMBA)_3^{(-1)}$ and $Au_3(pMBA)_4^{(-1)}$:

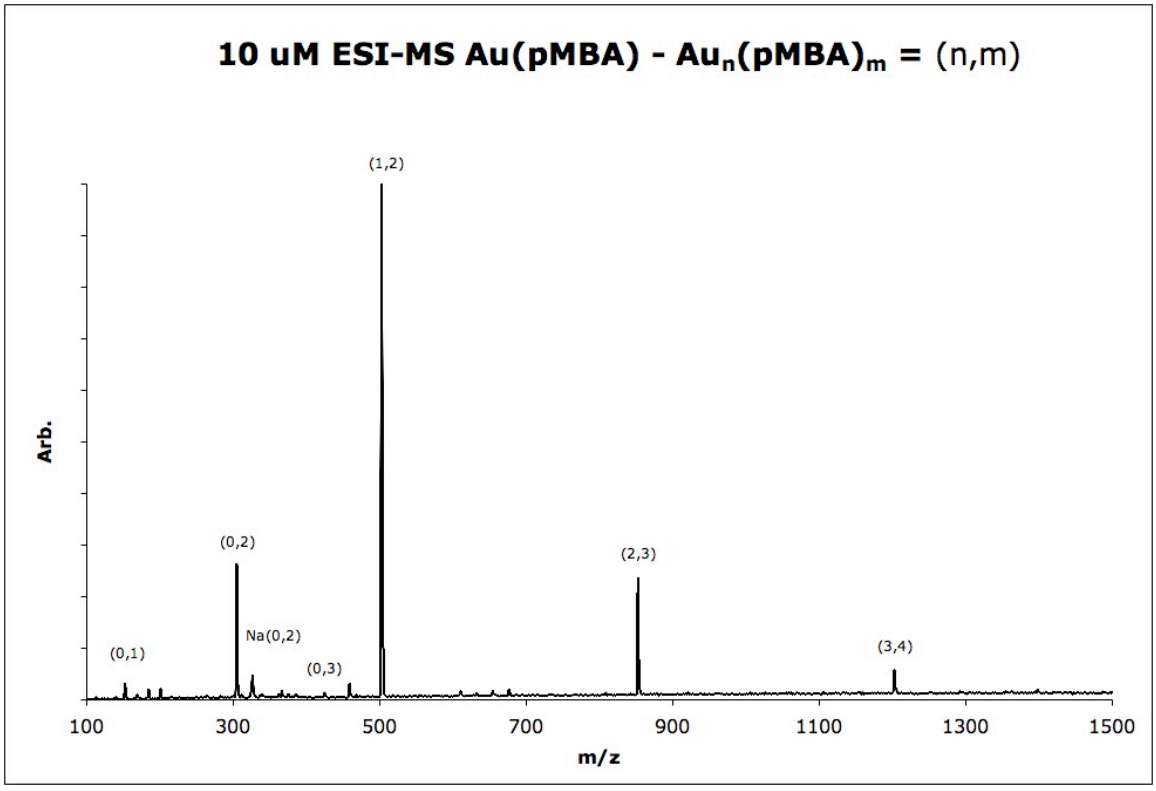

Figure 4.1. ESI-MS of Aurous-thiolate Oligomer.

In addition to the gold thiolate oligomers, a sizable quantity of the disulfide, with and without Na substitution are seen. Smaller amounts of the less stable tri-sulfide are also

present in addition to a very small, effectively negligible, amount of the free thiolate. These species, having no inclusive gold, form during reaction of the $Au(III)Cl_4^{-1}$ producing the Au(I)-thiolate found in the oligomer. It was confirmed later through ESI-MS that the majority of this is removed when the oligomer is rinsed prior to solubilization.

Amazingly, the ESI-MS spectra are identical for the standard synthesis as well as the soluble synthesis, indicating the thermodynamically preferential formation of the shorter linear oligomeric units.

4.3.2 Doubly Charged and Ring Oligomers

In the current literature, predictions exist for similar cyclic species, having one less thiolate available to their formula. Closer inspection of the ESI-MS spectra shows an exceedingly small, but real, amount of the predicted[41] $Au_4(pMBA)_4$ ring. This is the first structure, according to theory, that has no ring-induced strain. Other cyclic units were not observed. Also present in trace amounts was the doubly charged $Au_2(pMBA)_3$. It is not clear why none of the other linear oligomeric species were observed in the doubly charged, deprotonated state. This marks an interesting result as the $Au(pMBA)_2$ species, being the most abundant single-charged species, would be expected to provide the most candidates for the deprotonation:

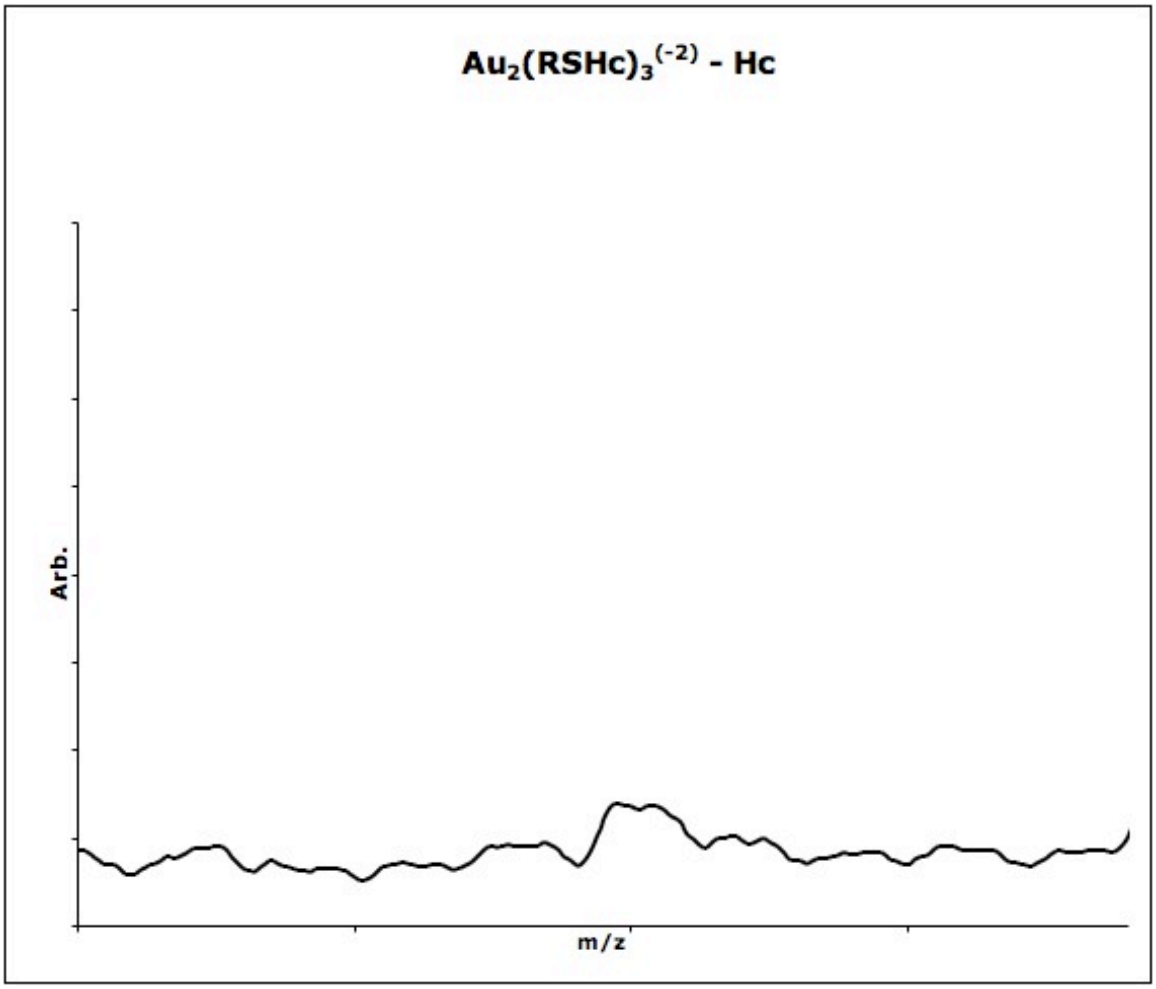

Figure 4.2. ESI-MS $Au_2(pMBA)_3^{-2}$

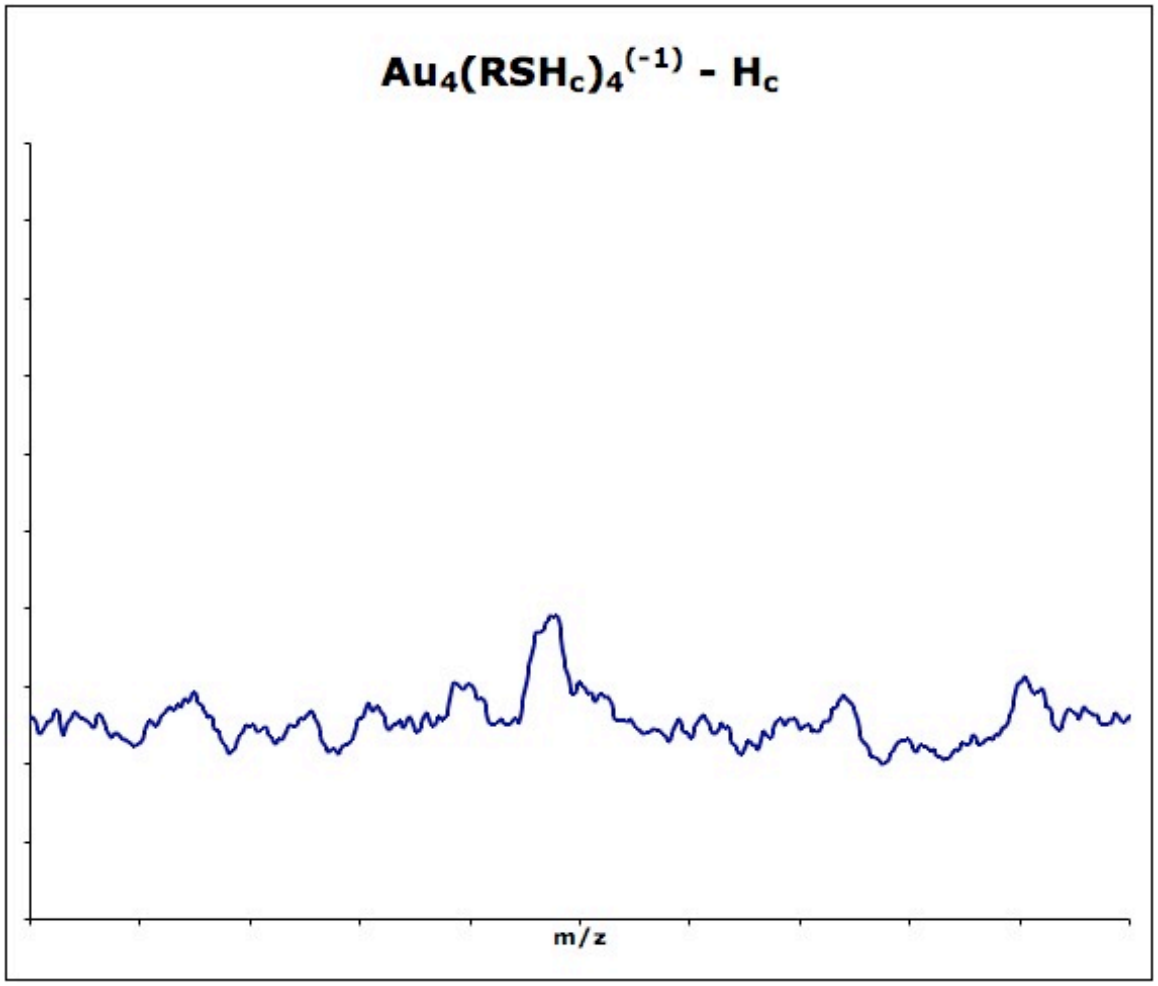

Figure 4.3. $Au_4(pMBA)_4^{-1}$.

Whereas the dominant $Au(pMBA)_2$ peak was previously normalized to a signal strength of 100, these trace signals both constitute a relative signal strength of < 2. Doubly charged species such as the oligomeric $Au_2(pMBA)_3^{-2}$ as well as the singly charged cyclic $Au_4(pMBA)_3^{-1}$ rely on the deprotonation of one of the available carboxylic groups. Despite the exceptionally efficient deprotonation capabilities of ESI, the inherent signal strength is unlikely to compete with the singly charged linear oligomers. These more abundantly seen species carry an inherent -1 charge by virtue of their stoichiometry. Known as naturally charged species, the singly charged linear oligomers would likely

overwhelm any species requiring an externally induced charging pathway. Analysis by matrix-assisted laser-desorption ionization, not available at the time, would provide a useful comparison in determining the true structural-dispersity of the synthesis product.

4.4 UV-VIS Analysis

Comparative UV-VIS spectra of the standard and soluble synthesis products were recorded using a Shimadzu UV-1601 spectrophotometer set to run in split-beam reference mode. 2.5 mM oligomer solutions, one by the standard technique and one by the soluble synthesis technique, were diluted with 50:50 solution to concentrations of 25μM and 10μM respectfully. The standard synthesis oligomer solution was rinsed prior to solubilization in 50:50 solution. Measurements were made in UV-transparent quartz cells, the reference cell being filled with 50:50 solution:

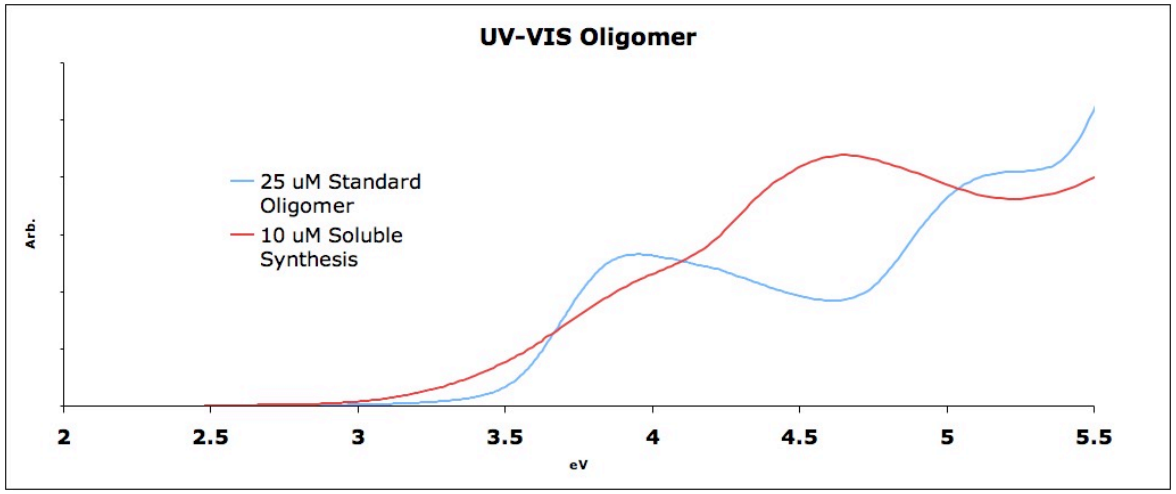

Figure 4.4. UV-VIS Comparison of Standard and Soluble Synthesis Products.

Seen only in the soluble synthesis spectrum is a peak centered at ~4.5eV. This feature is indicative of the disulfide[42] produced during formation of the oligomer. The lack of a 4.5eV peak in the standard soluble synthesis spectrum confirms its' effective removal during the rinsing stage prior to solubilization.

Contrasting UV-VIS measurements were also carried out on the pMBA solution and decanted rinse solution from the standard synthesis for further confirmation of peak assignments. 50μM pMBA solutions were prepared with pH values of 4.07 and pH 12.6. Because during the standard synthesis not all of the pMBA generally dissolves, it became apparent that a comparison was needed. A sample of the decanted rinse from the standard synthesis was also analyzed at an estimated concentration of 50μM. Because of the poly-dispersity of the reaction products, an exact concentration could not be designated. All solutions were diluted with 50:50 solution with identical experimental parameters found in the oligomer UV-VIS analysis:

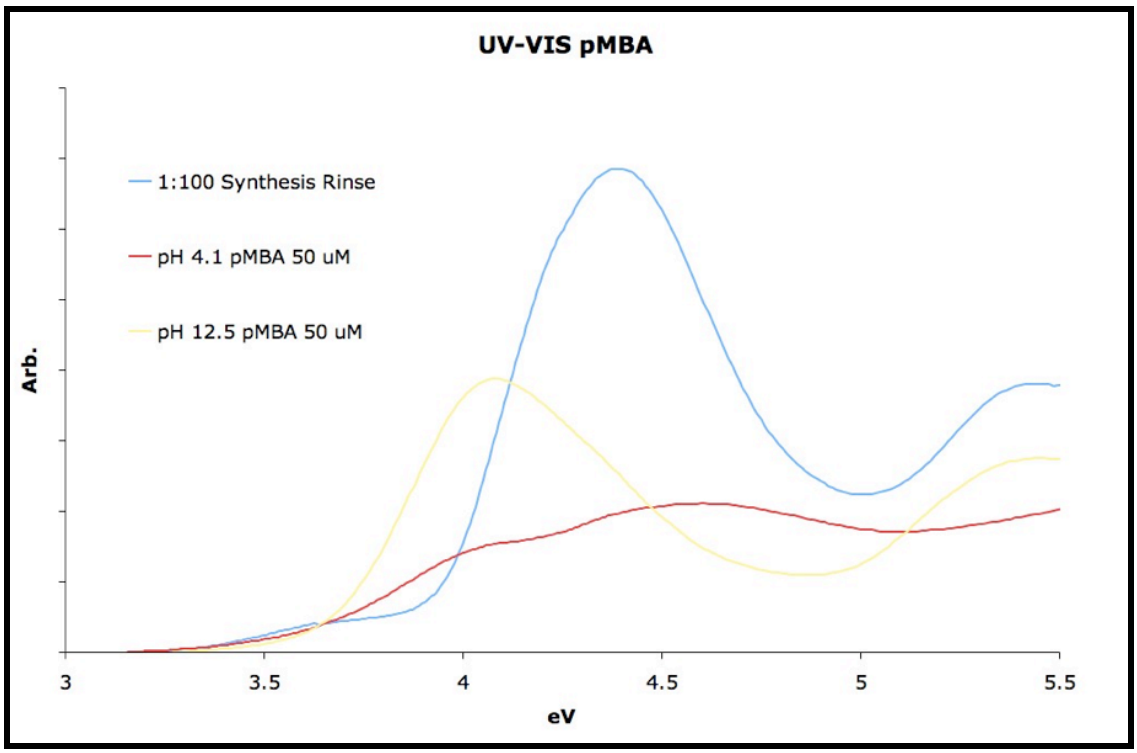

Figure 4.5. UV-VIS Comparison of pMBA and Standard Synthesis Byproducts.

Immediately apparent in the standard synthesis byproduct is the 4.5eV peak associated with the disulfide.[42] The two pMBA solutions, clearly not sharing this feature, are thereby assumed to be of relatively high purity and stable in solution. The high pH pMBA solution shows a primary peak, centered at ~4eV, identical to that seen in the oligomer UV-VIS albeit slightly shifted and associated with the phenyl group. The slight shift is a good indication of a small variation in chemical environment, here suggestive of coordination to gold. The lower pH pMBA solution, having not completely solubilized, shows a considerable weaker signal overall and lacks much of the spectral features seen in the oligomer or solubilized thiolate.

4.5 ATR-IR Analysis

Further spectroscopic analysis was pursued for a more complete characterization. Determination of available vibrational modes and relative shifts upon oligomer formation was carried out by way of attenuated total internal reflection infrared spectroscopy (ATR-IR).

ATR-IR spectra were recorded from 7500 - 600 cm^{-1} using a Bruker Equinox 55 FT-IR spectrometer (Bruker Optics Inc., Billerica, MA) equipped with a liquid nitrogen (LN_2) cooled MCT detector (Infrared Associates, Stuart, FL) and a Specac Gateway in-compartment horizontal ATR unit (Specac Inc., Cranston, RI). Each sample was deposited onto a trapezoidal ZnSe (n_D = 2.43 at λ = 5 μm) ATR crystal (MacroOptica, Moscow, Russia) with 6 effective reflection regions[43] (72 × 10 × 6 mm; 45 °). The spectrometer sample chamber was purged with dry air to stabilize atmospheric humidity and CO_2. The purge also served to assist in the rapid drying of the oligomeric solution, thus removing solvent related signal. Approximately 500 μL of 10 mM standard synthesis oligomer solution, having been thoroughly rinsed prior to solubilization, was pipetted onto the waveguide to maximize interaction with discrete evanescent field sensing regions. Spectra were then recorded at 120 s intervals throughout the drying process until a stable spectral signature was acquired. ATR-IR reference and sample spectra were generated by averaging 100 scans at a spectral resolution of 1 cm^{-1}. This process was repeated with a pH adjusted 10mM solution of pure pMBA. Also inset on the graph are computational predictions[44] for the $Au(pMBA)_2$ and $Au_2(pMBA)_3$:

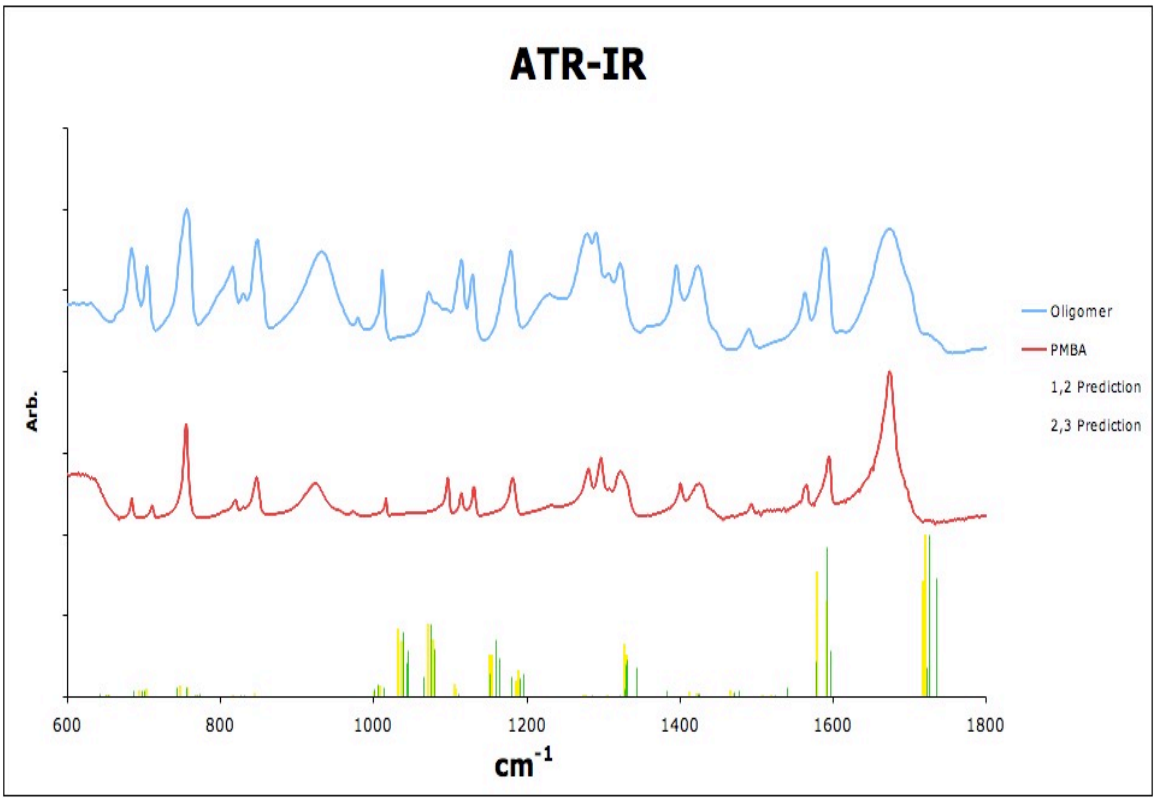

Figure 4.6. ATR-IR Spectroscopy of Oligomer, pMBA, and Computational Predictions.

At first glance there is an immediately apparent broadening of peaks in the oligomer spectrum. Since the thiolate vibrational modes become coupled across the oligomeric chain, this is an appropriate and expected result. A small number of features, such as those seen in the pMBA spectrum at ~700cm^{-1}, 800cm^{-1}, 1080cm^{-1}, 1400cm^{-1}, and 1600cm^{-1} are heavily suppressed. These modes also indicate, being present with a reduced amplitude, that the molecular coordination is to that of a larger, more impeding system.

In the displayed range of 600cm^{-1} to 1800cm^{-1}, only C-C, C-S, and other larger atom vibrational modes (i.e. no hydrogen related features.) are expected. The ATR-IR spectrum is consistent with the structure of the oligomer, where no non-hydrogen bonds

are broken. Any modes being unaccounted here would otherwise imply degradation or change in the pMBA structure inconsistent with the reaction and product model provided.

4.6 Exceptional Solubility

Once both synthesis techniques had been consistently carried out multiple times, a higher concentration solution was deemed necessary to approximate the oligomer solubility. An oligomer solution, produced at an initial concentration of 50 mM (50 mM $HAuCl_4$, 200 mM pMBA), also having been rinsed, re-solubilized in water, and adjusted to neutral pH, was lightly heated in a water bath to 60^0C, inducing slow evaporation of the water, thereby controllably increasing the concentration of oligomer. At a concentration of ~100 mM, the oligomer was observed to remain stably solubilized above pH ~6.8. At a concentration of ~450 mM, the solution was found to be stable at room temperature, as well as at pH levels as low as 7. Any further HCl addition immediately induced some level of precipitation. It is significant to note that at a concentration of 450 mM, assuming the dominant form of $Au(SRH_c)_2^{(-1)}$ as confirmed in ESI-MS, the solution is nearly 23% aurous-thiolate by mass, not including the presence of solubilized NaCl from the use of NaOH and HCl for pH adjustment:

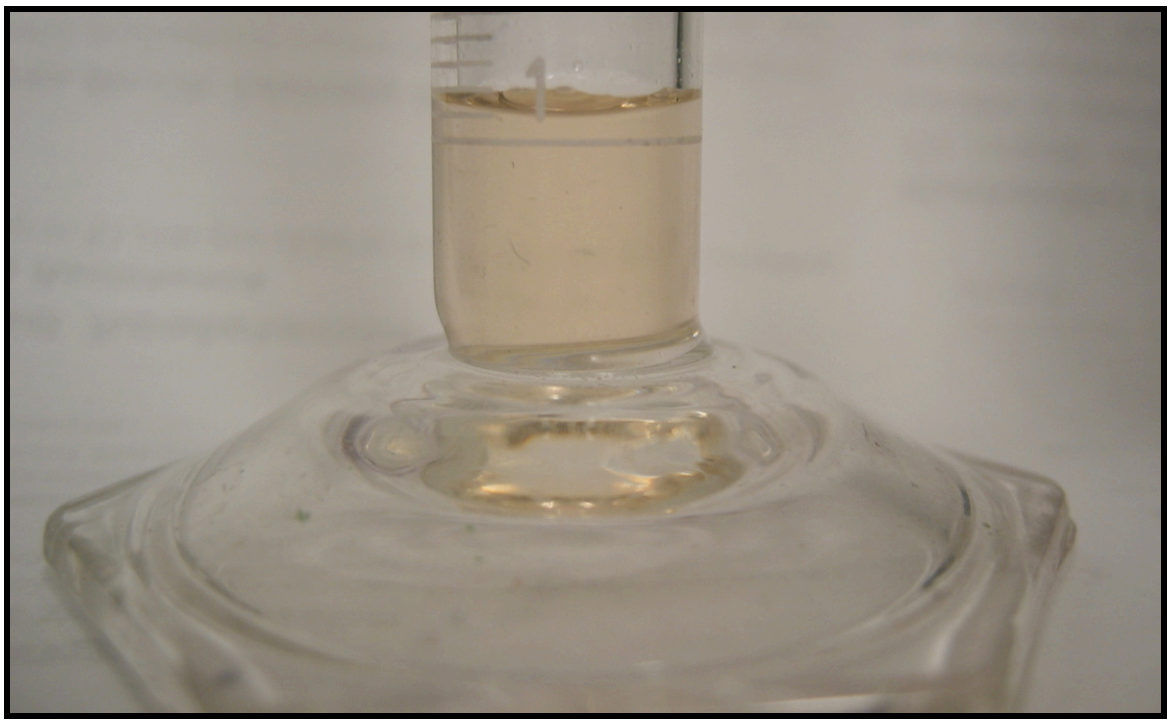

Figure 4.7. 450mM Oligomer Solution.

Contrast this to another highly soluble compound such as NaCl, which, at the same 450 mM concentration, would account for less than 2.7% total solution mass. Limited by the cost associated with the amount of gold required to accurately measure solubility at levels this high, it was determined much less quantitatively that the oligomer is likely soluble at levels well exceeding 1M. The solution shown in figure 4.7 was placed in a watch glass and allowed to dry overnight:

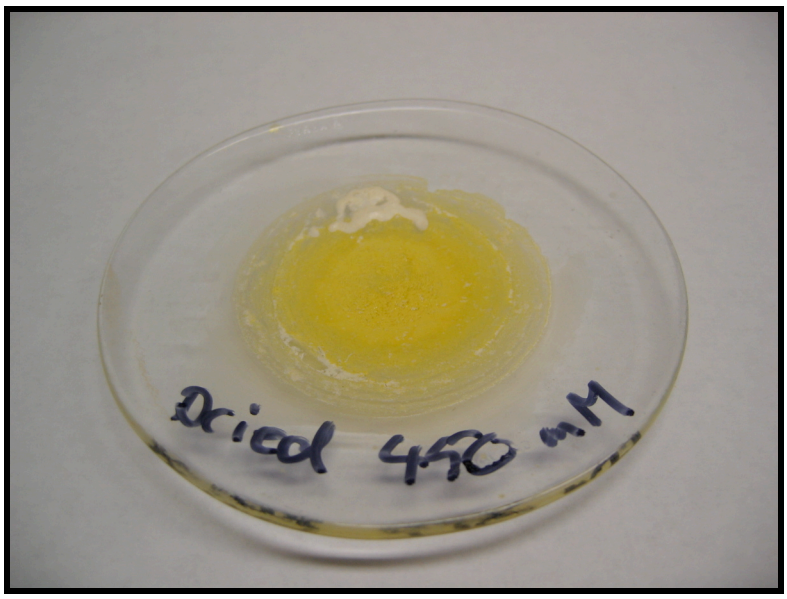

Figure 4.8. Dried Oligomer**.**

Once fully dried, approximately 500µL of neutral water was added and gently agitated across the surface. In less than one minute, the dried solid had completely re-entered solution without any further chemical treatment:

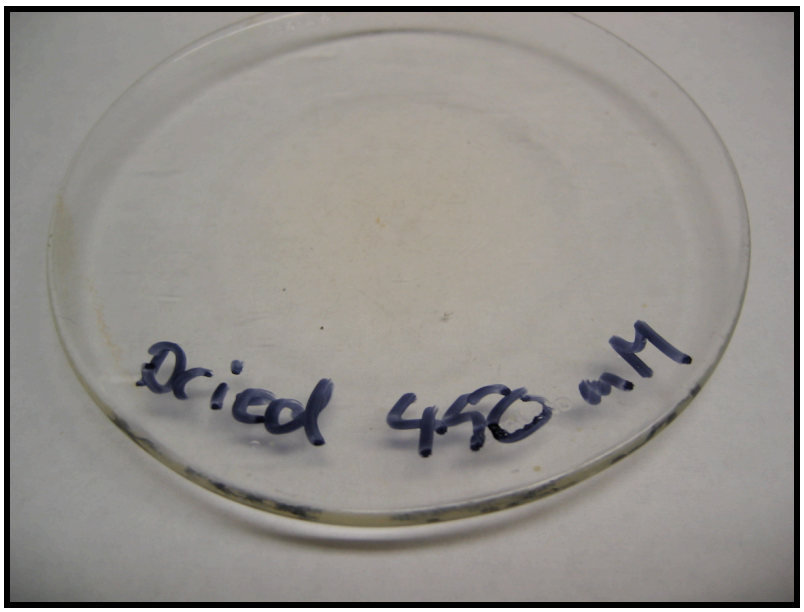

Figure 4.9. Re-Solubilized Oligomer (~1M).

Because of the exceptional solubility and stability of the pMBA-based aurous-thiolate oligomer, it is likely much research will continue utilizing this precursor. Both academic and industrial applications stand to gain immensely from its' extraordinary properties.

APPENDIX A

GOLD THIOLATE CLUSTER SYNTHESIS AND CHARACTERIZATION

As part on an ongoing joint project, spectroscopic analysis was carried out on samples provided by Dr. Pablo Jadzinsky,[39] et al. from Stanford University as well products synthesized in-house. These results constitute significant discovery, in good agreement with the current literature,[45,46] but are still pending[44] a number of additional experimental and theoretical collaborations.

Continuing the ongoing characterization of the structurally determined[39] $Au_{102}(pMBA)_{44}$ species, spectroscopic analysis was performed on samples provided by Dr. Pablo Jadzinsky. The sample provided, having been partially purified and expected to be a mixture of the $Au_{102}(pMBA)_{44}$ and a still to be characterized $Au_{150}(pMBA)_x$, had an approximate concentration of 25μM with a total volume of ~1ml. Near infrared spectroscopy, along with UV-VIS, was carried out on a Carey SE UV-VIS-NIR. Samples were provided in deuterated water and analyzed from 1000nm to 1800nm (5500cm^{-1} to 10,000cm^{-1}):

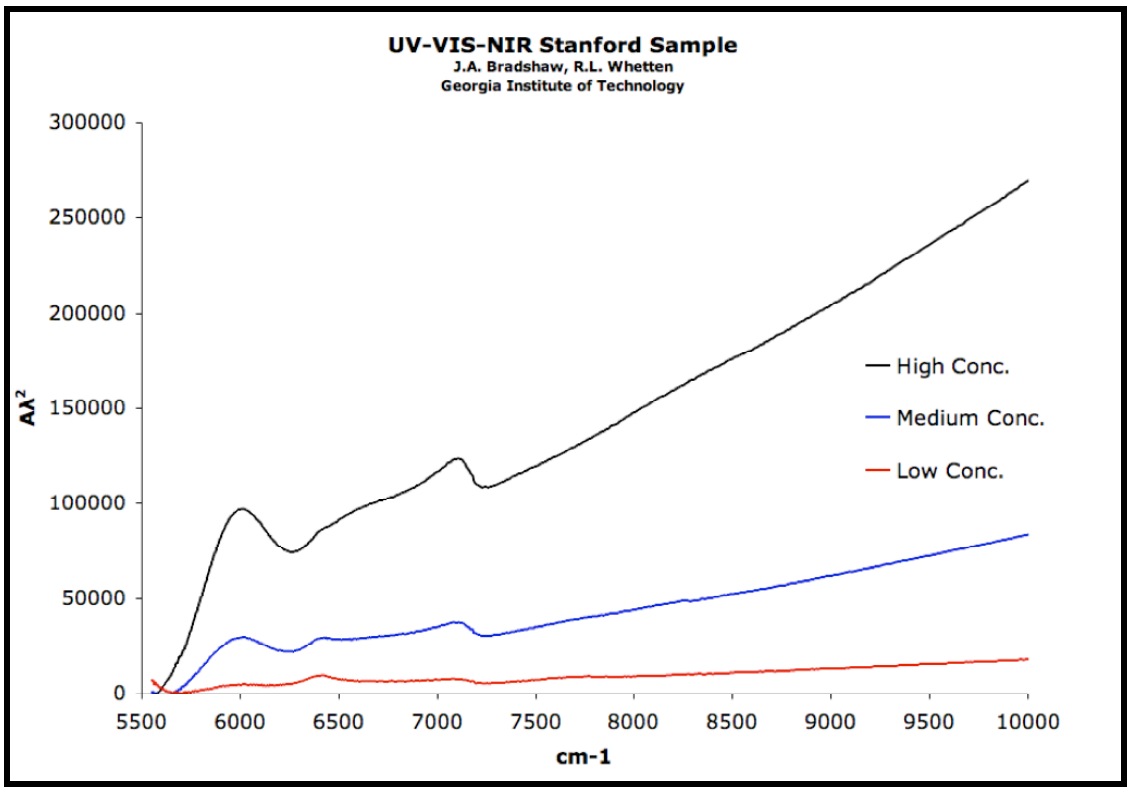

Figure A.1. UV-VIS-NIR Spectrum of $Au_{102}(pMBA)_{44}$.

Though exact concentrations were only approximated, the clusters have a clear and acceptable change in absorbance as a function of concentration. A clear onset in absorbance is visible at ~6000cm-1, in strong agreement with the most recent theory in the literature[45].

A reduction of the pMBA-based aurous-thiolate oligomer was also performed at Georgia Tech. Solutions of the standard synthesis and soluble synthesis oligomer were prepared as discussed in Section 4.2. Both solutions were diluted, from 10mM, to a final concentration of 10µM with 50:50 methanol-water. A 100µM solution of NaBH4 in 50:50 methanol-water was added, to an excess of 3.4 molar relative to the oligomer, and allowed to react overnight with constant stirring:

$$Au(pMBA)_2 + 3.4NaBH_4 \rightarrow Au_x(pMBA)_y \qquad \textbf{(A.1)}$$

The resulting solution remained colourless due to the exceptionally low concentration of clusters. A 500mL solution of reduced oligomer was heated to 60^{O}C and concentrated, using a RotoVap, to a final volume of 2ml. No further processing or purification was undertaken. The resulting solution was then analyzed using a Shimadzu UV-1601 UV-VIS spectrophotometer set to run in split-beam reference mode using 50:50 solution as a reference:

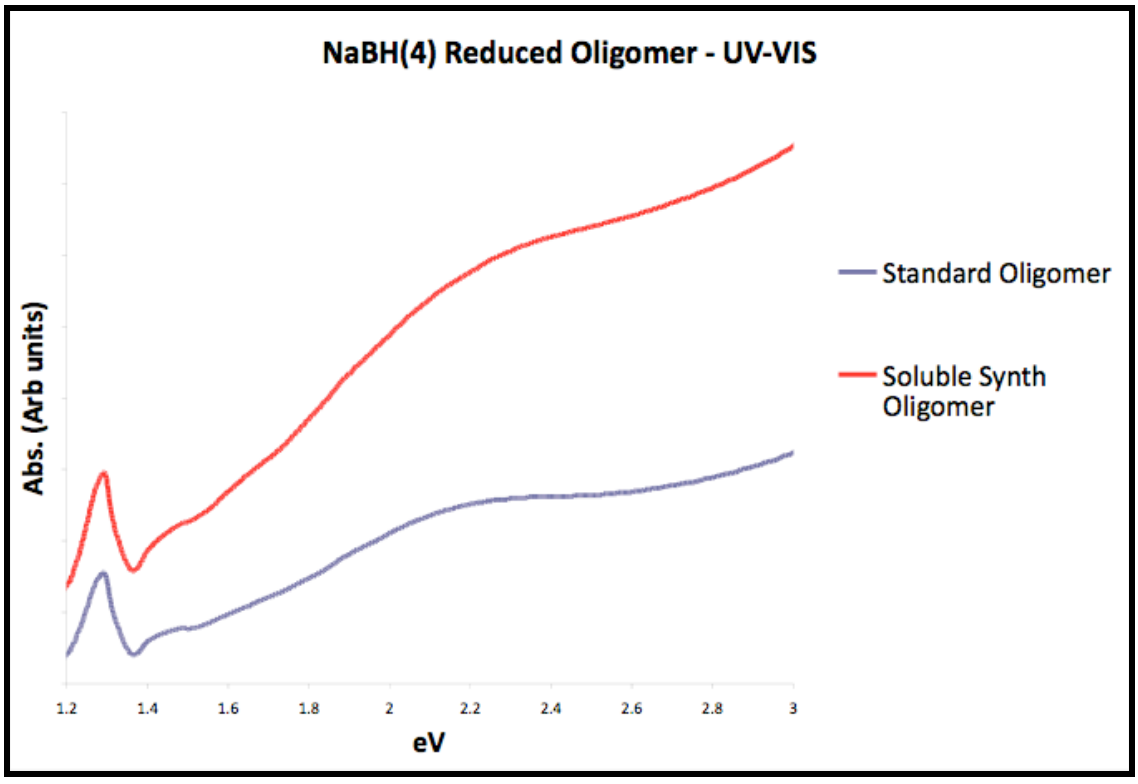

Figure A.2. UV-VIS Unpurified Oligomer Reduction Product.

Unlike the purified clusters provided by Jadzinksy et al, the clusters produced here are indicative of much smaller species.[47] The sharp peak at 1.3eV is consistent with predictions[46] for ~25-44 gold atoms. Further analysis is necessary to determine the relative dispersity of this and possible other clusters in solution.

APPENDIX B

GOLD IODIDE CLUSTERS

Thiolate species are often referred to as pseudo-halogens. As an ongoing parallel research study to the aurous-thiolate oligomers, the LDI clustering products of gold iodide were investigated. Due to the lack to literature on the subject, these are findings are considered of clear significance and justify further pursuit. Gold iodide was synthesized in a similar fashion to the aurous-thiolate oligomer, by reaction of tetrachloroaurate and potassium iodide. Au(I)I was filtered after each half-molar equivalent aliquot of potassium iodide was added to tetrachloroaurate solution due to Au(I)I ability to solubilize in the presence of excess iodide:[48]

$$Au(III)Cl_4^{-1}{}_{(aq)} + KI_{(aq)} \rightarrow Au(I)I_{(s)} \qquad \textbf{(B.1)}$$

The resulting product demonstrates a number of marked differences from bulk gold or the tetrachloroaurate initially used. The resulting dried powder has a faint yellowish-green tint:

Figure B.1. Gold Iodide Powder.

By comparison, tetrachloroaurate is a much darker orange colour and significantly more hydrophilic:

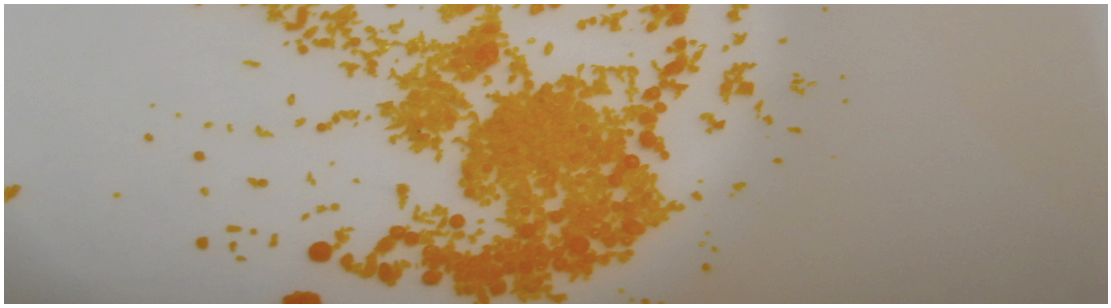

Figure B.2. Tetrachloroaurate Powder.

The tetrachloroaurate is in fact so hydrophilic that it readily absorbs water out of the atmosphere at a rate visible to the naked eye.

Another significant property of the Au(I)I is its' low thermal and radiative stability. Au(I)I powder will readily decompose to solid gold and iodine vapor if subjected to intense light, low pressure, and/or temperatures above 100^{O}C. While preparing a target rod for LDI analysis, it was found necessary to cool the starting powder as well as the hydraulic die to 0^{O}C prior to pressing. Upon introduction to vacuum inside the LDI reactor, a given target rod had a useful lifetime of only a few hours.

Initial characterization was performed using ESI-MS. Au(I)I powder was dissolved in de-ionized water using a slight excess of KI to induce formation of the soluble $Au(I)I_2^{-1}$. Positive and negative ion-mode analysis was performed though no discernable cation ion signal was collected. Negative mode analysis gave an exceptionally strong signal. Optimized single parameters utilized an ion-transfer capillary temperature of 300^{0}C. At a concentration of 10μM, the gold iodide solution presented an

exceptionally strong and highly aurous-thiolate analogous signal:

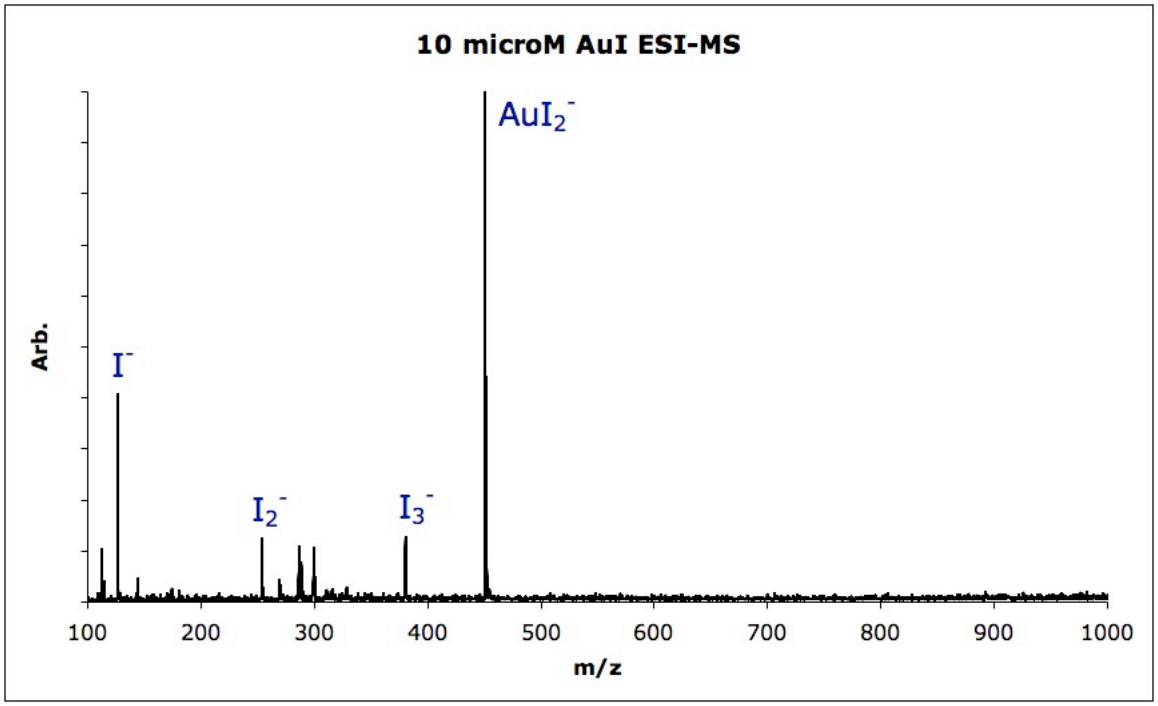

Figure B.3. ESI-MS Analysis of Au(I)I.

Nearly identical to the ESI-MS of the aurous-thiolate oligomer, the gold-iodide spectrum includes multiply coordinated iodide species similar to the single, di and tri-sulfides. Unlike the aurous-thiolate, however, is the lack or larger homologs such as Au_2I_3.

Alternative analysis of gold iodide clusters was performed using LDI. Identical settings as those found in Section 3.3. Both positive and negative mode ion collection was performed and the results were rather astonishing:

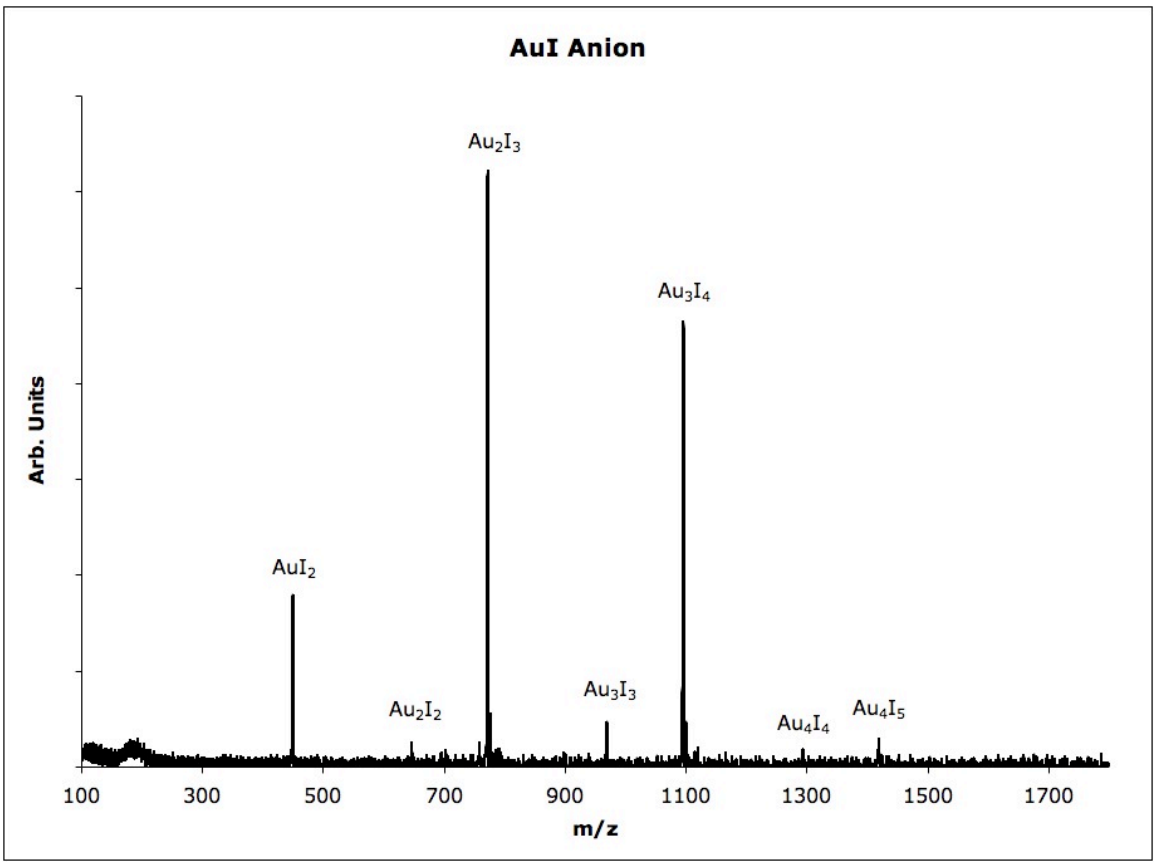

Figure B.4. LDI-MS Analysis of Anion Au(I)I.

In anion mode, the clustering appears to produce Au(I)I species kindred with the oligomer but without an apparent upper limit on size. For cation analysis a drastically different trend was seen:

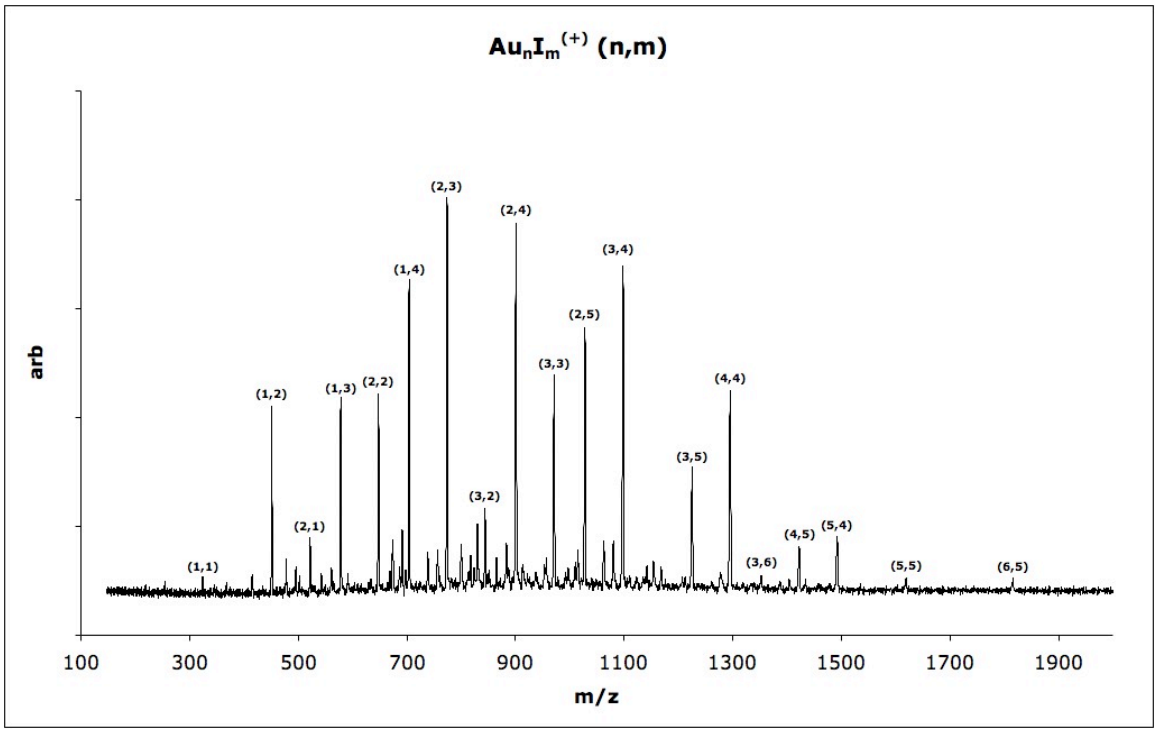

Figure B.5. LDI-MS Analysis of Cation Au(I)I.

Nearly every possible configuration of Au and iodide exists. Mostly likely iodine molecules, known to coordinate into long chains such as I_3^{-1}, I_5^{-1}, and I_7^{-1} are the most likely explanation for this phenomenon but further investigation is necessary.

APPENDIX C

NACl:H_2O THERMODYNAMIC PLOTS

Following are a collection of graphical plots representing the data from Table 3.1 and Table 3.2.

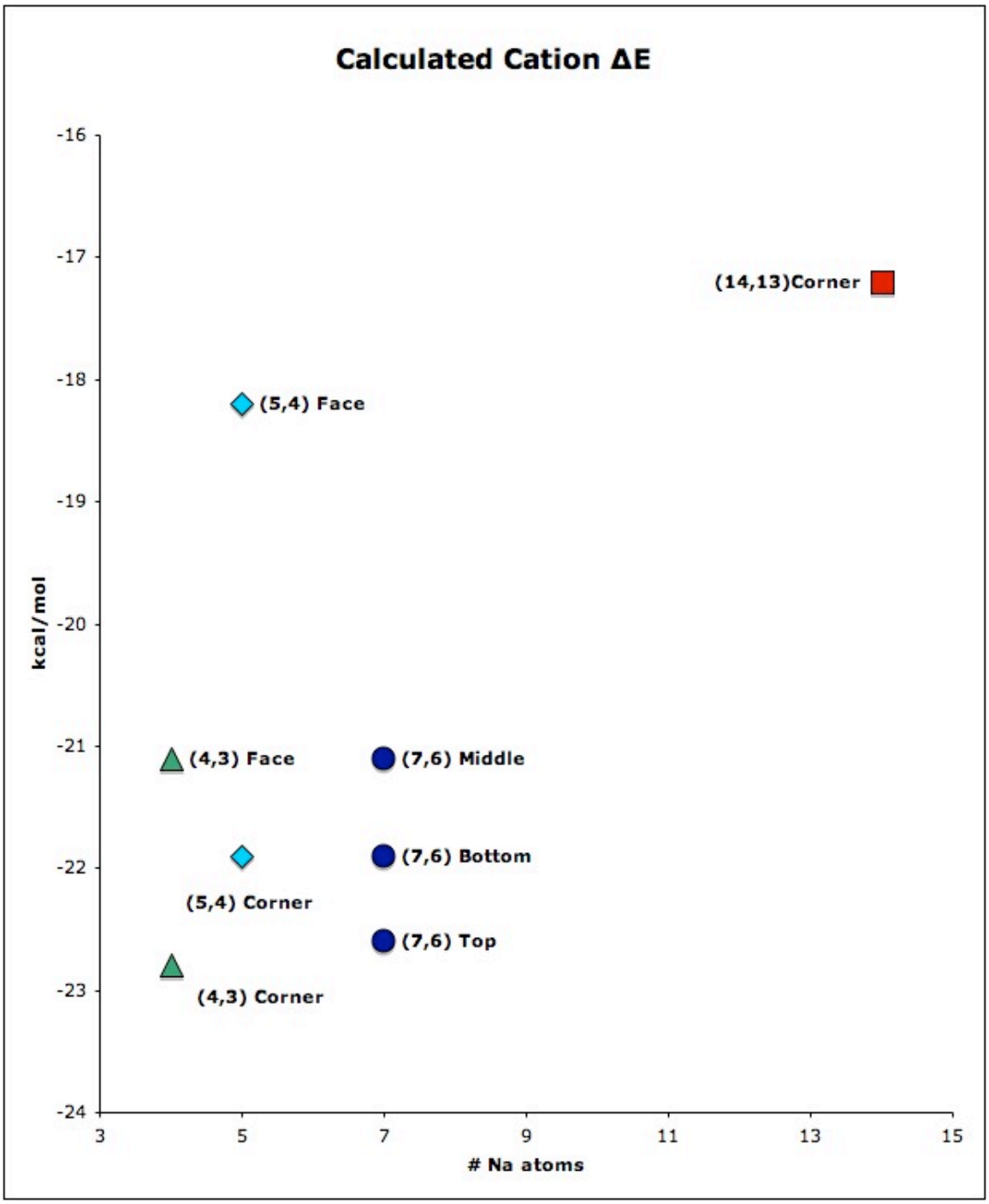

Figure C.1. Plotted Computational Cation ΔE Values.

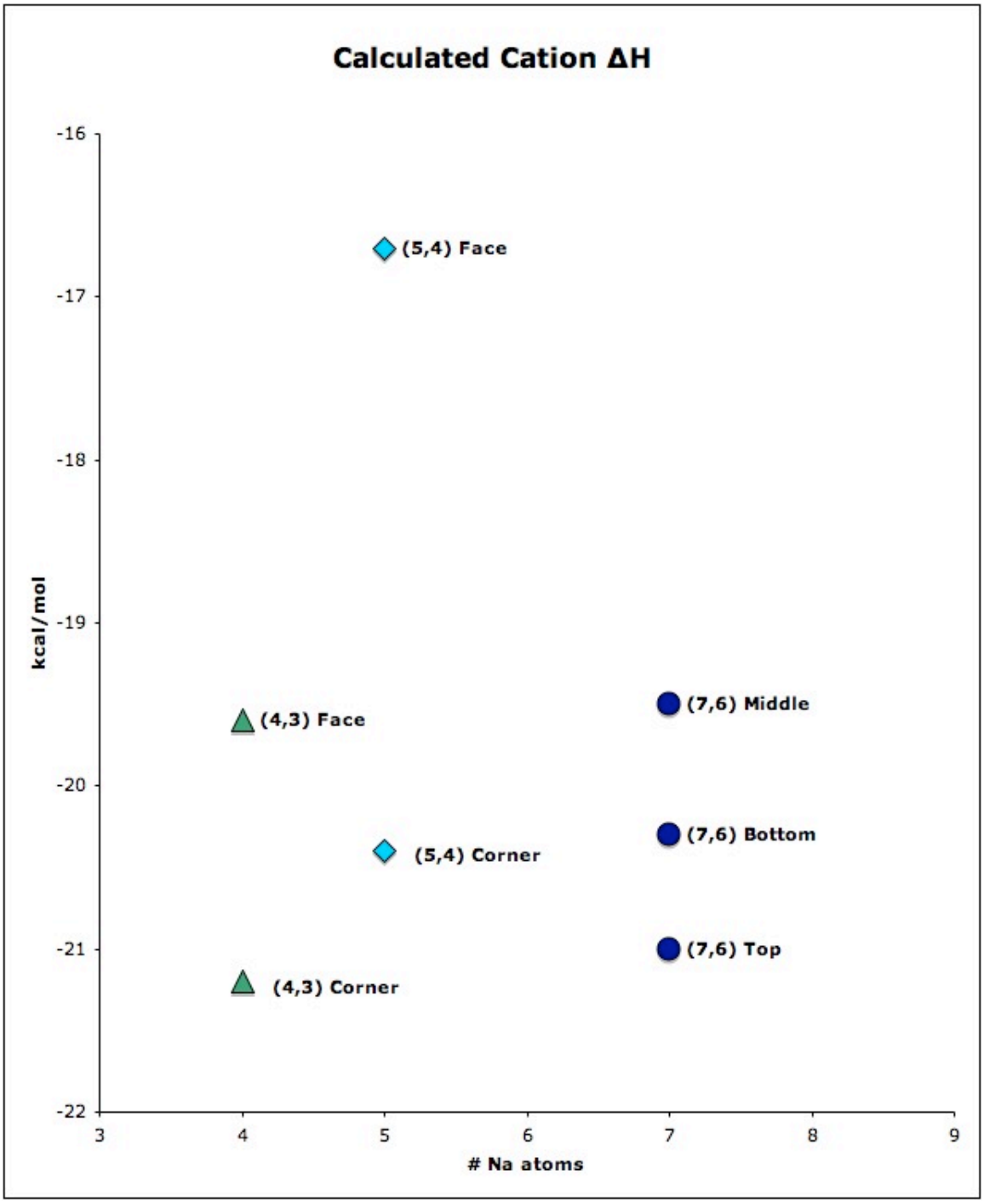

Figure C.2. Plotted Computational Cation ΔH Values.

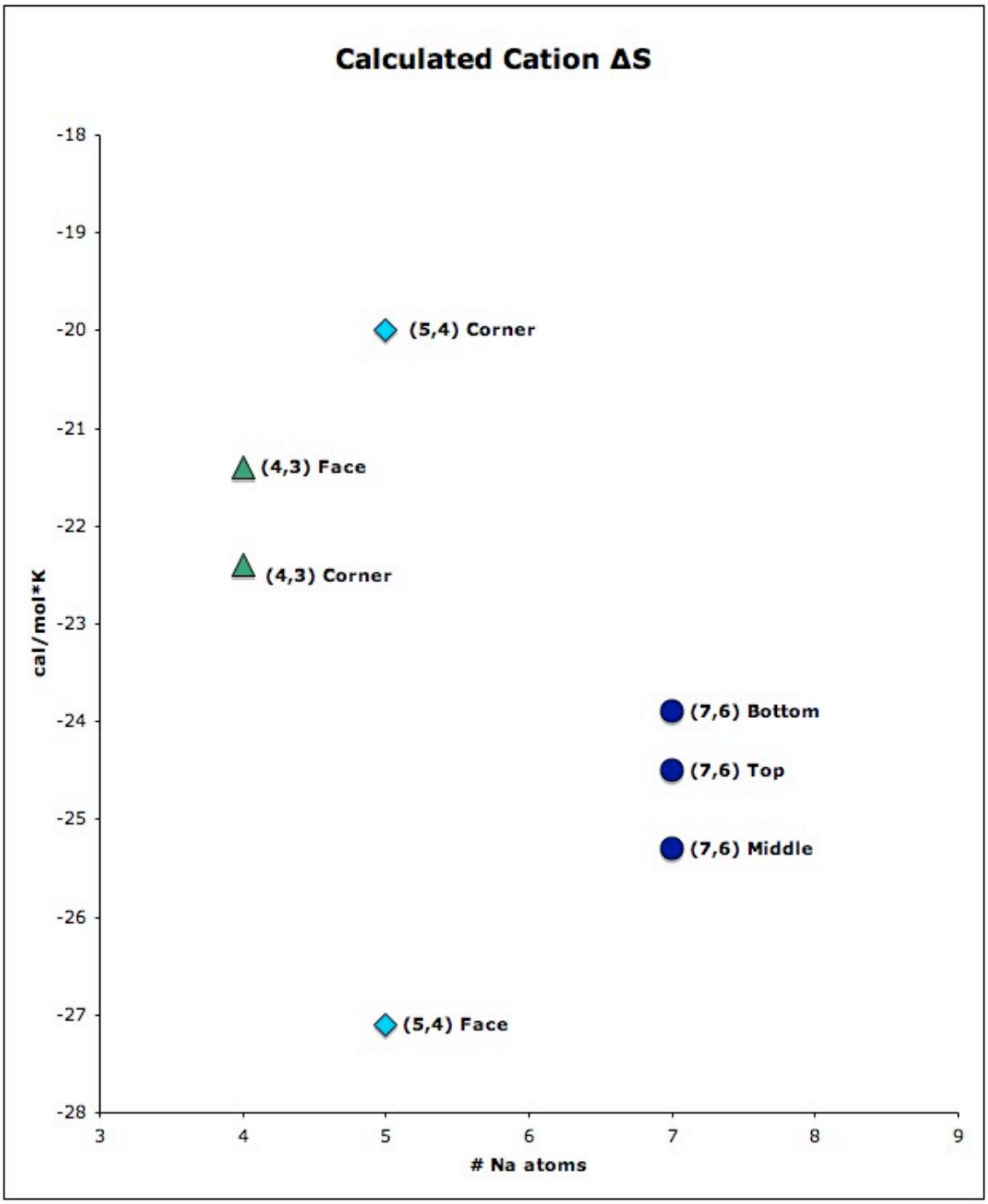

Figure C.3. Plotted Computational Cation ΔS Values.

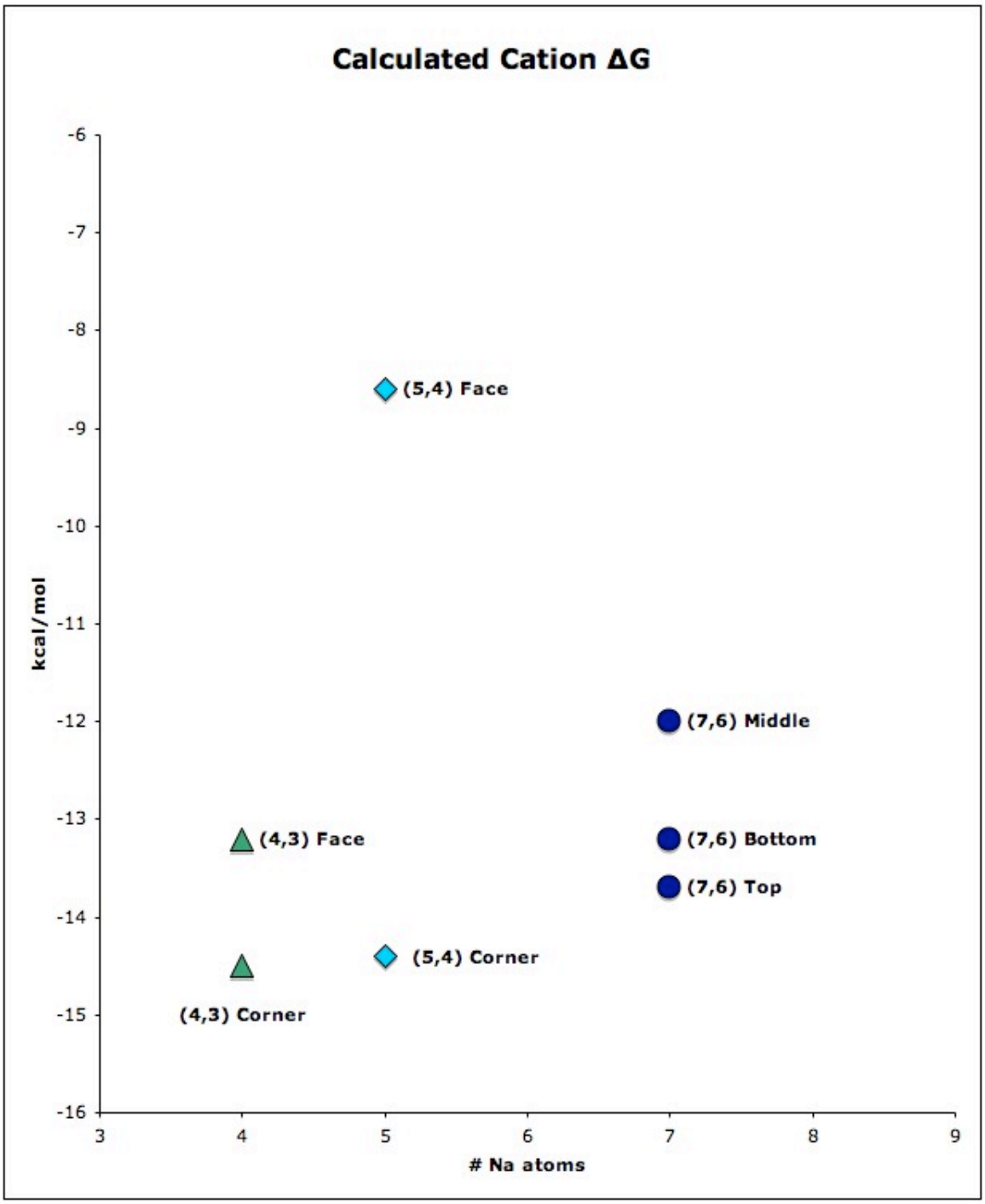

Figure C.4. Plotted Computational Cation ΔG Values.

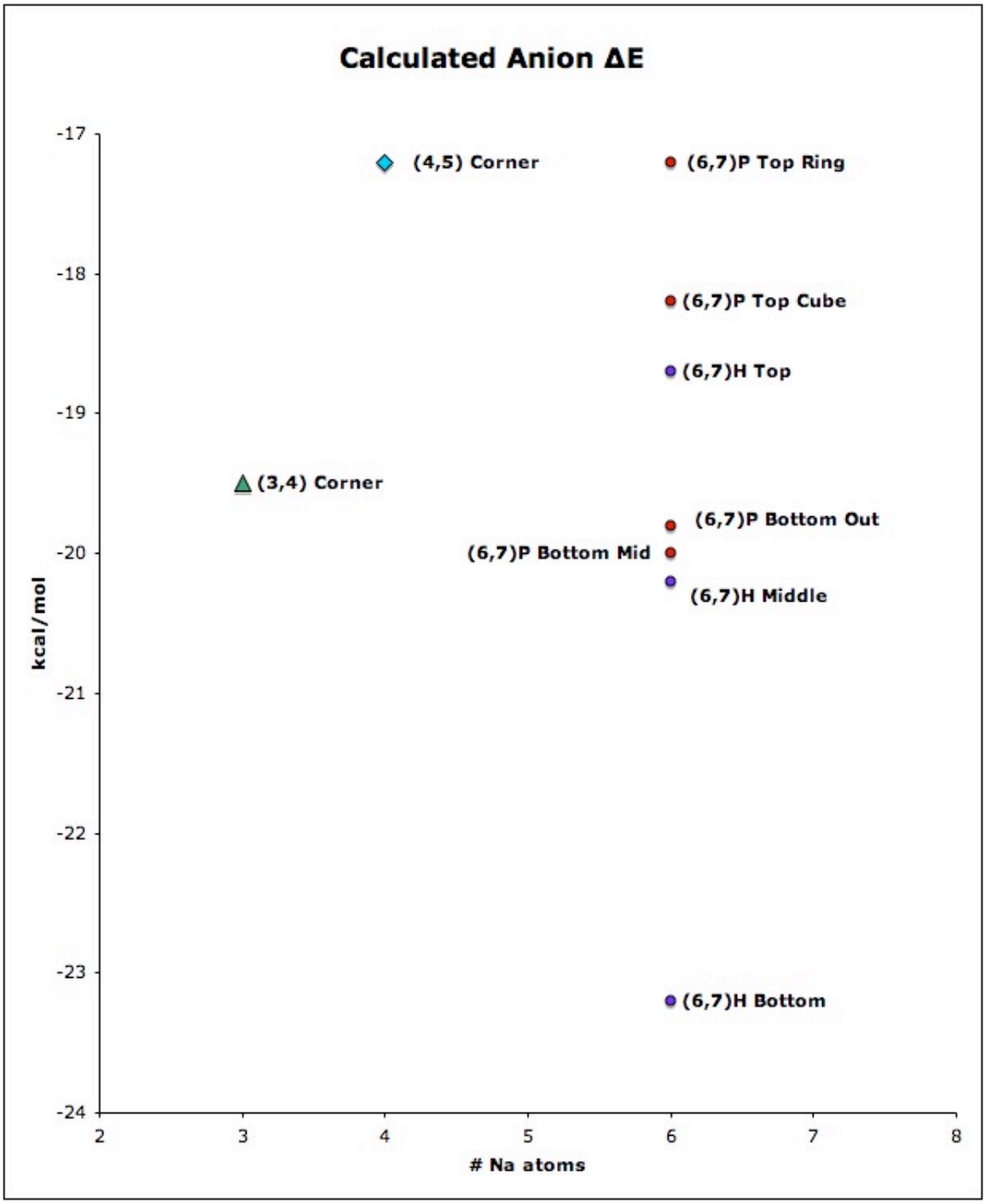

Figure C.5. Plotted Computational Anion ΔE Values.

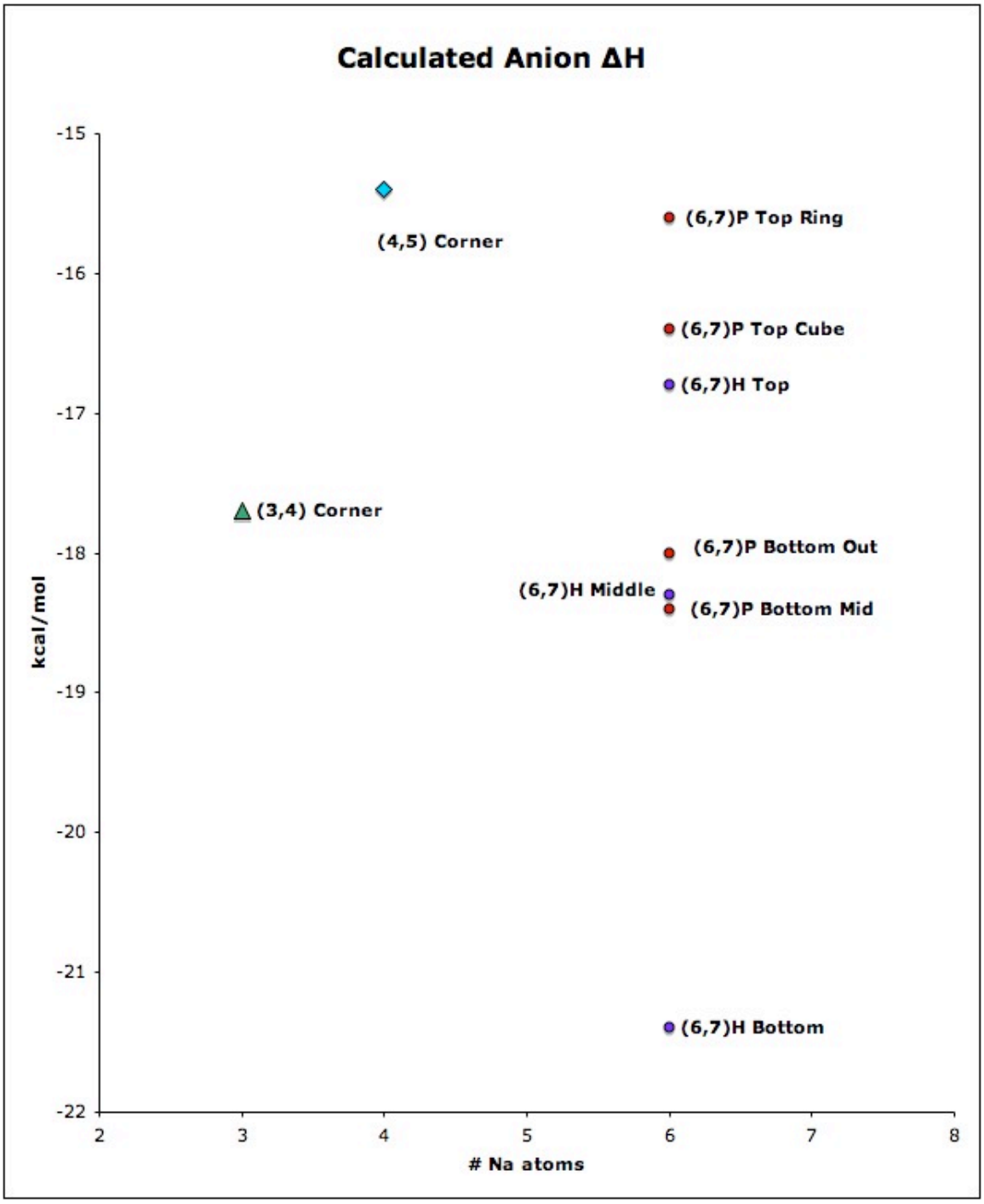

Figure C.6. Plotted Computational Anion ΔH Values.

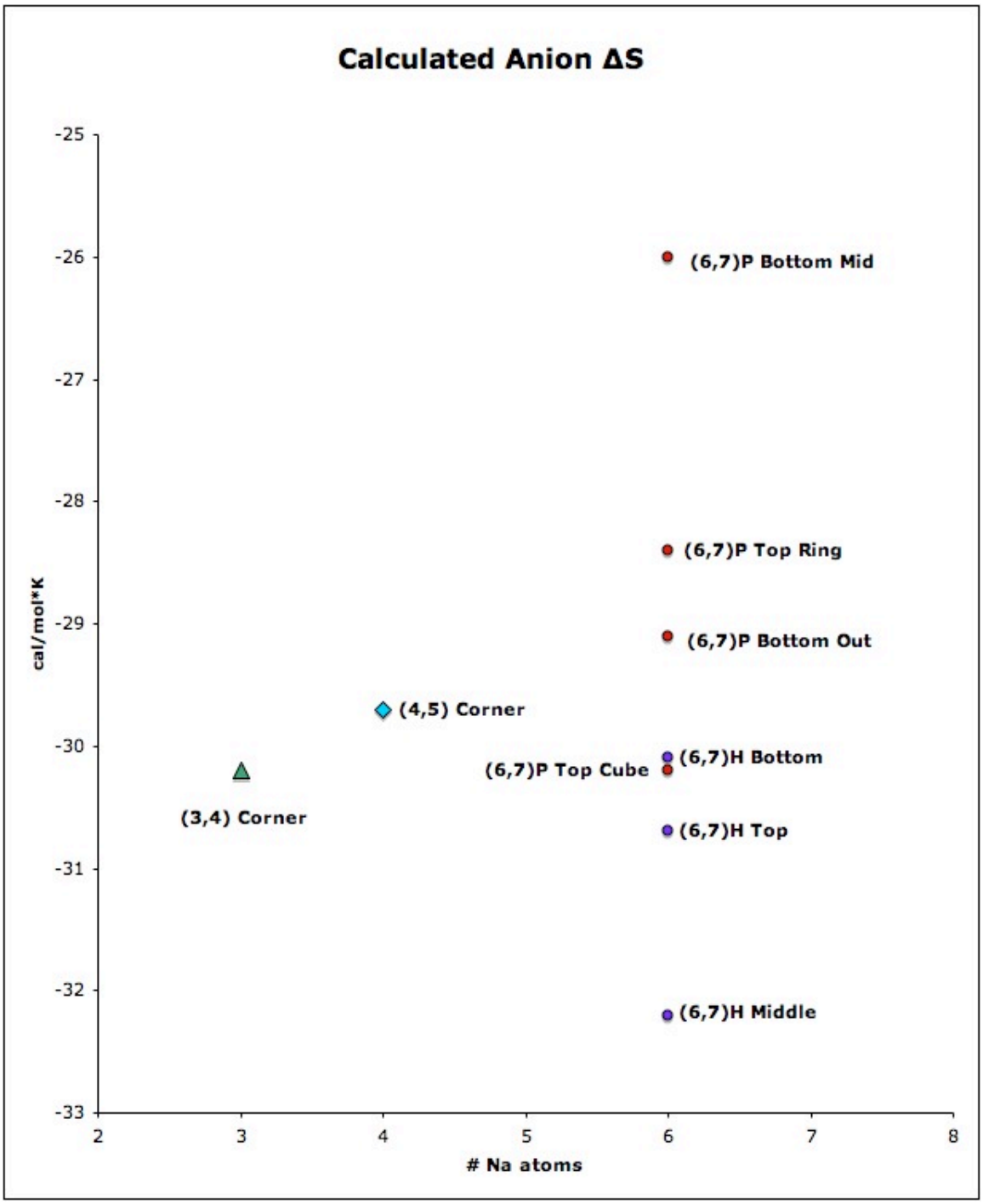

Figure C.7. Plotted Computational Anion ΔS Values.

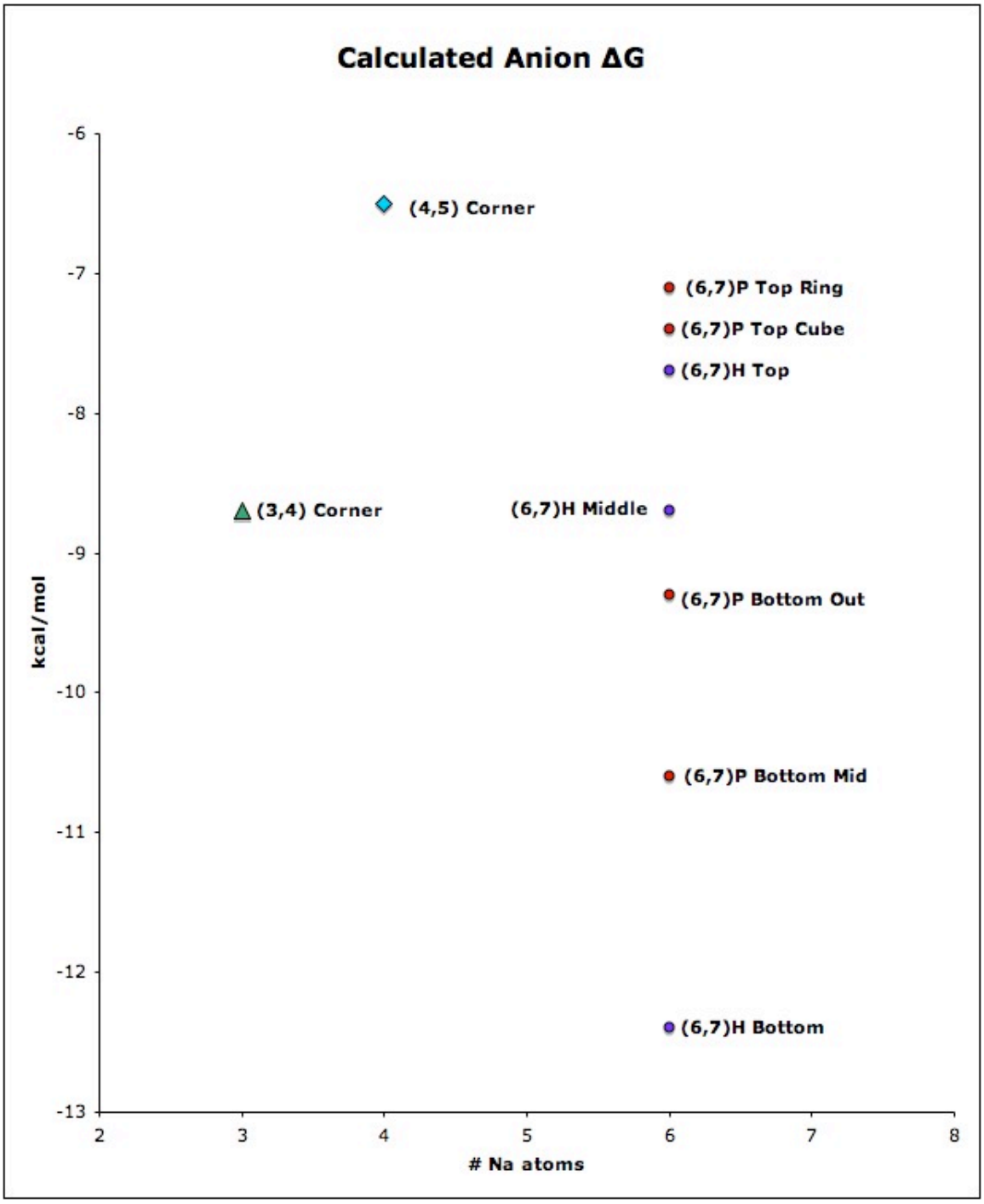

Figure C.8. Plotted Computational Anion ΔG Values.

REFERENCES

[1] Faraday, Philos., Trans. R. Soc. Lond. B. Biol. Sci., 147: 145 (1857)

[2] Schmidbaur, Hubert. *Gold: Progress in Chemistry, Biochemistry and Technology*. New York: Wiley & Sons Press, 1999.

[3] Dormann., Rev. Physique Appliquee., 16: 6 (1981)

[4] Faist J, Capossa F, Sivco D, et al., Science, 264: 5158 (1994)

[5] Schuurmans M., Thooft G., Phys. Rev. B., 31: 12 (1985)

[6] Novoselov KS, Geim AK, Morozov SV, et al., Nature, 438: 7065 (2005)

[7] Berger C, Song ZM, Li XB, et al., Science, 312: 5777 (2006)

[8] "Copper NanoParticles" http://www.sciencedaily.com/articles/n/nanoparticle.html, May 12th, 2008.

[9] Dalfovo F, Giorgini S, Pitaevskii LP, et al., Revs. Mod. Phys., 71: 3 (1999)

[10] Bergeron DE, Castleman AW, Morisato T, et al., Science, 304: 5667 (2004)

[11] Gerion D, Hirt A, Billas IML, et al., Phys. Rev. B., 62: 11 Pages: 7491-7501 (2000)

[12] Cotter, Robert J. *Time-of-Flight Mass Spectrometry*. Washington D.C.: ACS Press, 1997.

[13] Horowitz P, Hayes T.. *The Art of Electronics*. Cambridge University Press, 1989.

[14] Continuum Surelite OPO Operation Manual. 2001

[15] Behlke Power Electronics Handbook. 2005

[16] Prospero, J., Mohnen, V., Jaenicke, R., Charlson, R., Delany, C., Moyer, J., Zoller, W., Rahn, K., Rev. Geophys. Sae Phys., 21: 1607 (1983)

[17] "2007 Salt Statistics", http://minerals.usgs.gov/minerals/pubs/commodity/salt/, December 11th, 2007.

[18] Kurlansky, Mark (2002), *Salt: A World History*, New York: Walker & Co.

[19] Laszlo, Pierre. *Salt: Grain of Life*. Arts and traditions of the table. New York: Columbia University Press, 2001.

[20] Hollenbach, D., Salpeter, E. E., Appl. J., 163: 155 (1971)

[21] Martin T., Phys Rep-Rev. Sec. Phys. Lett. 95: 3 (1983)

[22] Beck R., StJohn P., Homer M., et al., Science, 253: 5022 (1991)

[23] Welch D., Lazareth O., Dienes G., et al., J. Chem. Phys., 68: 5 (1978)

[24] Landman U., Scharf D., Jortner J., Phys. Rev. Lett., 54: 16 (1985)

[25] Martin T., Phys Rep-Rev. Sec. Phys. Lett., 273: 4 (1996)

[26] Rajagapol G., Barnett R., Landman U., Phys. Rev. Lett., 67: 6 (1991)

[27] Diefenbach J., Martin T., J. Chem Phys., 83: 5 Pages: 2238-2241 (1985)

[28] Engkvist O., Stone A., J. Chem. Phys., 110: 24 Pages: 12089-12096 (1999)

[29] Yang Y., Meng S., Wang E., Phys. Rev. B., 74: 24 (2006)

[30] Zhang Q., Carpenter C., Kemper P., Bowers M., J. Am. Chem. Soc.,125 (2003)

[31] Blades AT, Peschke M, Verkerk UH, et al., J. Am. Chem. Soc., 126: 38 (2004)

[32] Margie L. Homer, Doctoral Thesis, University of California at Los Angeles, (1993)

[33] Frank E. Livingston, Doctoral Thesis, University of California at Los Angeles, (1995)

[34] N. G. Phillips, C. W. S. Conover, and L. A. Bloomfield, J., Chem. Phys. 94: 4980 (1991)

[35] Barnett R., Landman U., J. Phys. Chem., 100: 33 (1996)

[36] Ewing G., Intermolecular Forces and Clusters II, 116 (2005)

[37]] Schmidbaur, Hubert. *Gold: Progress in Chemistry, Biochemistry and Technology*. New York: Wiley & Sons Press, 1999.

[38] Zhang J., Chi Q., Nielsen J., et al., Langmuir, 16: 18 (2000)

[39] Jadzinsky P., Calero G., Ackerson C., et al., Science, 318: 5849 (2007)

[40] Supplementary Information: Jadzinsky P., Calero G., Ackerson C., et al., Science, 318: 5849 (2007)

[41] Gronbeck H., Walter M., Hakkinen H., J. Am. Chem. Soc., 128: 31 (2006)

[42] "UV-VIS Database" http://webbook.nist.gov/chemistry, December 3rd, 2007

[43] G. T. Dobbs and B. Mizaikoff, App. Spec., 60: 573 (2006).

[44] Bradshaw, et al., In Draft. 2008

[45] M. Walter, J. Akola, O. Lopez-Acevedo, P. D. Jadzinsky, G. Calero, C. J. Ackerson, H. Gronbeck, H. Hakkinen, PNAS online (2008) 0801001105

[46] Nirmalya K.C.,Yuichi N., Hironori T., Yukatsu S., Tatsuya T., PNAS online (2008) JA8005379

[47] Price R., Whetten R., J. Phys. Chem. B., 110: 44 (2006)

[48] Teicher M., Weil R., Phys. Rev. B. 18: 12 (1978)

VITA

JAMES A. F. BRADSHAW

James Adam Ferguson Bradshaw was born in Calgary, Alberta Canada. He attended public schools in Calgary as well as 10^{th} through 12^{th} grade at The John Cooper School in The Woodlands, Texas. He received a B.S. in Physics from The Georgia Institute of Technology, Atlanta, Georgia, in 2002 and returned to pursue a doctorate in Physical Chemistry. James has also spent time pursuing research and/or coursework under various titles and positions at Columbia University in New York City, The Landau Institute for Theoretical Physics outside of Moscow in Russia, and Oxford University in Oxford, England. When he is not working on his research, James enjoys any and all things involving fabrication and/or high speed.